POLITECNICO DI TORINO

Master's Degree in Electronic Engineering

Politecnico
di Torino

Master's Degree Thesis

Overcoming eddy current solvers: on the full-wave modelling of quasi-static scenarios

Supervisors

Prof. Francesco P. ANDRIULLI

Prof. Adrien MERLINI

Candidate

Viviana GIUNZIONI

ACADEMIC YEAR 2020-2021

Summary

Low-frequency electromagnetic compatibility and interference (EMC/EMI) circuit simulations are often based on quasi-static, eddy-current approximations of Maxwell's system [1] and require ad-hoc solvers to be employed. The need for relying on approximate physics stems from the instability of standard full-wave Maxwell solvers when the frequency decreases. The focus of this thesis has been to work on and extend a formulation capable of overcoming this limitation and performing exact modelling of circuits with a full-wave Maxwell solver [2]. Based on the Poggio-Miller-Chang-Harrington-Wu-Tsai (PMCHWT) equation, this full-wave formulation is well-conditioned, stable and accurate over a broad frequency range. This result is obtained by exploiting primal and dual quasi-Helmholtz projectors that allow for an adequate frequency rescaling of the solenoidal and quasi-irrotational components of the system. The eddy current regime is included in the range of applicability of this solver which answers to the strong industrial need for efficient modelling of eddy currents with the significant advantage that, unlike standard eddy current solvers, the stabilized formulation is capable of handling multi-scale scenarios in which incompatible approximations of the physics would need to co-exist. The resulting scheme is also compatible with multiply connected geometries, allowing modelling of complex and realistic circuits. One of the most promising applications of this technology is the study of the behaviour of an electronic equipment in terms of emission, immunity to radiation, and coupling. These electromagnetic compatibility properties are known to be of crucial importance in the design phase of electronic systems.

In this work, the formulation has been validated against analytic scattering models, both in near and in far field, for exciting plane waves oscillating in a wide range of frequencies to ensure that it remains accurate and stable under the most extreme modelling conditions. After this preliminary check, we tackled the problem of modelling of the electromagnetic fields on some canonical circuital structures for which analytical solutions are known, in order to further verify the performances of the solver. To this end, a different kind of excitation has been implemented, capable of modelling the enforcement of a potential difference. We successfully managed to extract system-based parameters, such as voltages and currents, that

made it possible to estimate the impedance of the structures under test, both inductive and capacitive. The results obtained are in excellent agreement with what expected from circuit theory. Finally, a new line of investigation into strategies for the numerical integration of the Green's function dampened behaviour in highly lossy media has been opened. The promising results achieved from this analysis will allow to further broaden the range of frequencies and conductivities over which the model can be efficiently exploited and ensure that the solver can perform even on the most challenging-to-model media that can be encountered.

Acknowledgements

First and foremost, I want to express my gratitude to Prof. Francesco Andriulli, for the enthusiasm and the dedication in approaching his job. I thank him in particular for the time spent for guiding me through this fascinating discipline and for the great opportunity received to conduct my thesis work in this group and to continue my scientific growth in this framework in the next future.

Then, I am grateful to every person met at CERL: any of them gave precious advice and support during the last months. In particular, thanks to my co-supervisor, Prof. Adrien Merlini, for his continuous and patient helping me in keeping the right direction, to my careful reviewers, Dr. Clément Henry and Engr. Davide Consoli, and to Dr. Tiffany Chhim, who deeply studied the topics treated in this thesis before me during her recently concluded doctoral studies and left her knowledge on them and her code to me as inheritance.

Final thanks are directed to my friends and my family, for the support and the encouragement offered during all these years.

Table of Contents

List of Figures

Acronyms

ACA
Adaptive Cross Approximation

BC
Buffa-Christiansen

BEM
Boundary Element Method

EFIE/O
Electric Field Integral Equation/Operator

EMC
electromagnetic compatibility

EMI
electromagnetic interference

EQS
Electro-quasistatic

FMM
Fast Multiple Method

KCL
Kirchhoff Current Law

KVL
Kirchhoff Voltage Law

MFIE/O

Magnetic Field Integral Equation/Operator

MLACA

Multi Layer Adaptive Cross Approximation

MLFMM

Multi Layer Fast Multiple Method

MoM

Method of Moments

MQS

Magneto-quasistatic

PCB

Printed Circuit Board

PEC

Perfect Electric Conductor

PMC

Perfect Magnetic Conductor

PMCHWT

Poggio-Miller-Chang-Harrington-Wu-Tsai

RHS

right hand side

RWG

Rao-Wilton-Glisson

Chapter 1

Introduction to Electromagnetism

1.1 The Maxwell's system

The whole electromagnetic theory rely on a set of two equations, called the Maxwell's system. Given an open surface S bounded by a closed contour C, these equations read

$$\oint_C \boldsymbol{\mathcal{E}}(\boldsymbol{r},t)\cdot d\boldsymbol{l} = -\frac{d}{dt}\iint_S \boldsymbol{\mathcal{B}}(\boldsymbol{r},t)\cdot d\boldsymbol{S} - \iint_S \boldsymbol{\mathcal{M}}(\boldsymbol{r},t)\cdot d\boldsymbol{S} \tag{1.1}$$

$$\oint_C \boldsymbol{\mathcal{H}}(\boldsymbol{r},t)\cdot d\boldsymbol{l} = \frac{d}{dt}\iint_S \boldsymbol{\mathcal{D}}(\boldsymbol{r},t)\cdot d\boldsymbol{S} + \iint_S \boldsymbol{\mathcal{J}}(\boldsymbol{r},t)\cdot d\boldsymbol{S}. \tag{1.2}$$

Definitions and units of the quantities involved are the following:

$\boldsymbol{\mathcal{E}}$ is the electric field, V/m;

$\boldsymbol{\mathcal{H}}$ is the magnetic field, A/m;

$\boldsymbol{\mathcal{D}}$ is the electric flux density, A·s/m^2;

$\boldsymbol{\mathcal{B}}$ is the magnetic flux density, V·s/m^2;

$\boldsymbol{\mathcal{J}}$ is the electric current density, A/m^2;

$\boldsymbol{\mathcal{M}}$ is the magnetic current density, V/m^2.

These equations are valid in any extended region of space (no continuity conditions are required). They are known as the Maxwell's equations in integral form.

Stokes' theorem, which reads $\oint_C \boldsymbol{A} \cdot d\boldsymbol{l} = \iint_S (\nabla \times \boldsymbol{A}) \cdot d\boldsymbol{S}$ with $\boldsymbol{A}$ being a generic vector field, is exploited to move to the differential form:

$$\nabla \times \boldsymbol{\mathcal{E}}(\boldsymbol{r}, t) = -\frac{d}{dt}\boldsymbol{\mathcal{B}}(\boldsymbol{r}, t) - \boldsymbol{\mathcal{M}}(\boldsymbol{r}, t) \tag{1.3}$$

$$\nabla \times \boldsymbol{\mathcal{H}}(\boldsymbol{r}, t) = \frac{d}{dt}\boldsymbol{\mathcal{D}}(\boldsymbol{r}, t) + \boldsymbol{\mathcal{J}}(\boldsymbol{r}, t). \tag{1.4}$$

Since flux integrals of these quantities are involved (and then simplified), some conditions need to be verified for these expressions to be valid: the vector fields should be «single-valued, bounded, continuous functions of position and time and exhibit continuous derivatives» [3]. Such conditions hold true if the surface S and its contour C lie in a homogeneous medium.

In these equations, the electric current density $\boldsymbol{\mathcal{J}}$ accounts for both conduction current, which obeys Ohm's law ($\boldsymbol{\mathcal{J}_c} = \sigma\boldsymbol{\mathcal{E}}$), and impressed current, source of the system. The term $\frac{d}{dt}\boldsymbol{\mathcal{D}}$ represents instead the electric displacement current. By symmetry, contribution $\frac{d}{dt}\boldsymbol{\mathcal{B}}$ can be denoted as magnetic displacement current. Magnetic current density $\boldsymbol{\mathcal{M}}$ is usually introduced in the Maxwell's system in order to preserve symmetry and duality properties, even if magnetic currents and charges have not been observed in nature.

Finally, it is necessary to mention the equations relating fields and flux densities, called constitutive equations,

$$\boldsymbol{\mathcal{B}}(\boldsymbol{r}, t) = \boldsymbol{\mu}\,\boldsymbol{\mathcal{H}}(\boldsymbol{r}, t) \tag{1.5}$$

$$\boldsymbol{\mathcal{D}}(\boldsymbol{r}, t) = \boldsymbol{\epsilon}\,\boldsymbol{\mathcal{E}}(\boldsymbol{r}, t), \tag{1.6}$$

where the quantities denoted as $\boldsymbol{\mu}$ and $\boldsymbol{\epsilon}$ are respectively the permeability and the permittivity of the medium in which field propagation occurs. These are in general tensor quantities and show complicated dependence on position, on time, on frequency, and on the field itself. A commonly used simplification is to consider μ and ϵ as constant scalars. Moreover, $\mu = \mu_0\,\mu_r$, $\epsilon = \epsilon_0\,\epsilon_r$, where μ_0 and ϵ_0 are permeability and permittivity of vacuum, whose values are

$$\mu_0 = 4\pi \times 10^{-7}\,\mathrm{H/m}$$

$$\epsilon_0 = \frac{1}{\mu_0\,c_0^2} \simeq 8.85 \times 10^{-12}\,\mathrm{F/m}.$$

Speed of light in vacuum, denoted as c_0, is one of the seven fundamental constants established in the International System of Units, of value 299,792,458 m/s.

1.2 Continuity and divergence equations

Assumption of conservation of the electric charge is based on experimental evidences. It is translated in the continuity equation

$$\oiint_S \boldsymbol{\mathcal{J}}(\boldsymbol{r},t)\cdot d\boldsymbol{S} = -\frac{d}{dt}\iiint_V \rho_e(\boldsymbol{r},t)\,dV, \tag{1.7}$$

where S is a closed surface enclosing the volume V, ρ_e is electric charge density, in $\mathrm{A{\cdot}s/m^3}$. Equivalently, the differential form, obtained from divergence theorem ($\oiint_S \boldsymbol{A}\cdot d\boldsymbol{S} = \iiint_V \nabla\cdot\boldsymbol{A}\,dV$), reads

$$\nabla\cdot\boldsymbol{\mathcal{J}}(\boldsymbol{r},t) = -\frac{d}{dt}\rho_e(\boldsymbol{r},t). \tag{1.8}$$

By duality, also conservation of magnetic charge follows, leading to the magnetic charge continuity equation in integral and differential forms

$$\oiint_S \boldsymbol{\mathcal{M}}(\boldsymbol{r},t)\cdot d\boldsymbol{S} = -\frac{d}{dt}\iiint_V \rho_m(\boldsymbol{r},t)\,dV \tag{1.9}$$

$$\nabla\cdot\boldsymbol{\mathcal{M}}(\boldsymbol{r},t) = -\frac{d}{dt}\rho_m(\boldsymbol{r},t), \tag{1.10}$$

where the quantity ρ_m denotes the magnetic charge density, in $\mathrm{V{\cdot}s/m^3}$. From the Maxwell's system and the continuity equations, two more equations can be derived. They can be written in integral form,

$$\oiint_S \boldsymbol{\mathcal{B}}(\boldsymbol{r},t)\cdot d\boldsymbol{S} = \iiint_V \rho_m(\boldsymbol{r},t)\,dV \tag{1.11}$$

$$\oiint_S \boldsymbol{\mathcal{D}}(\boldsymbol{r},t)\cdot d\boldsymbol{S} = \iiint_V \rho_e(\boldsymbol{r},t)\,dV, \tag{1.12}$$

or, equivalently, in differential form,

$$\nabla\cdot\mathcal{B}(\boldsymbol{r},t) = \rho_m(\boldsymbol{r},t) \tag{1.13}$$

$$\nabla\cdot\mathcal{D}(\boldsymbol{r},t) = \rho_e(\boldsymbol{r},t). \tag{1.14}$$

These equations relating flux densities and charges are sometimes called divergence equations, with reference to the operator involved in their differential form.

1.3 Maxwell's equations in frequency domain

Any time-harmonic vector, i.e. with time-dependence of cosinusoidal form, can be written as the sum of its in-phase and in-quadrature components:

$$\boldsymbol{\mathcal{V}}(\boldsymbol{r},t) = \boldsymbol{V'}(\boldsymbol{r})\cos(\omega t) - \boldsymbol{V''}(\boldsymbol{r})\sin(\omega t) = \Re\{(\boldsymbol{V'}(\boldsymbol{r}) + j\boldsymbol{V''}(\boldsymbol{r}))\,e^{j\omega t}\}.$$

In the previous notation, the complex vector $(\boldsymbol{V'} + j\boldsymbol{V''}) = \boldsymbol{V}$ is called phasor and, given the angular frequency ω, contains the same amount of information of the original vector $\boldsymbol{\mathcal{V}}$. Assuming time-harmonic dependence of all the quantities involved in the Maxwell's system, it is possible to rewrite them in terms of their phasors. Once noticed the property

$$\frac{d}{dt}\boldsymbol{\mathcal{V}}(\boldsymbol{r},t) = \Re(j\omega\boldsymbol{V}(\boldsymbol{r})\, e^{j\omega t}),$$

real part operators and complex exponentials can be simplified to obtain finally

$$\nabla \times \boldsymbol{E}(\boldsymbol{r},\omega) = -j\omega\boldsymbol{B}(\boldsymbol{r},\omega) - \boldsymbol{M}(\boldsymbol{r},\omega) \tag{1.15}$$

$$\nabla \times \boldsymbol{H}(\boldsymbol{r},\omega) = j\omega\boldsymbol{D}(\boldsymbol{r},\omega) + \boldsymbol{J}(\boldsymbol{r},\omega). \tag{1.16}$$

In the previous expressions, quantities in roman letters represent the complex phasors of the respective real-valued vector fields in time domain.

It is interesting to notice that the same frequency-domain representation of the Maxwell's system can be obtained through the Fourier transform of time-domain quantities involved. It suggests the fact that equations 1.15 and 1.16 are not valid for time-harmonic fields only, but for any $\mathbb{R}$ integrable field with a generic spectrum.

1.4 Electric and Magnetic fields in free space

Solution of the Maxwell's system coupled with properly boundary conditions can be very complicated. An analytic solution can be found only in few special cases. The most important between them is the so called radiation in free space, i.e. an homogeneous and infinitely extended region of space, as it will be clear in the following chapter.

1.4.1 Potentials for electric sources

Consider the Maxwell's equations in free space in frequency domain form, equations 1.15 and 1.16. Assume that the source of the system is of electric type only, magnetic current $\boldsymbol{M}$ and magnetic charge ρ_m do not come into play. Equation 1.13 states that the magnetic flux density is solenoidal. By consequence, it can be expressed as the curl of another vector field, by virtue of the vector calculus identity $\nabla \cdot (\nabla \times \boldsymbol{A}) = 0$,

$$\boldsymbol{B}(\boldsymbol{r}) = \nabla \times \boldsymbol{A}(\boldsymbol{r}). \tag{1.17}$$

Equation 1.17 sets the curl of the vector field $\boldsymbol{A}$, while its divergence is still to be defined. Inserting eq. (1.17) into eq. (1.15), one obtains

$$\nabla \times (\boldsymbol{E}(\boldsymbol{r}) + j\omega\boldsymbol{A}(\boldsymbol{r})) = 0.$$

By recalling that $\nabla \times \nabla\phi_e = 0$, an irrotational field can be written as the gradient of a scalar field. So it is possible to write

$$\boldsymbol{E}(\boldsymbol{r}) + j\omega\boldsymbol{A}(\boldsymbol{r}) = -\nabla\phi_e(\boldsymbol{r}). \tag{1.18}$$

Just the gradient of ϕ_e is known, so, as $\boldsymbol{A}$, it is not determined uniquely, but possible choices differ from a constant field.

From equation 1.18, it is clear that the electric field scattered by the electric current and charges, sources of the system, can be expressed in terms of the vector field $\boldsymbol{A}(\boldsymbol{r})$ and the scalar field $\phi_e(\boldsymbol{r})$, called respectively electric vector potential and electric scalar potential, with units V·s/m and V.

A closed form relation between potentials and sources can be found easily from manipulation of the equations seen so far. By using the definitions of the potentials, second Maxwell's equation (1.16) reads

$$\nabla \times \left(\frac{1}{\mu}\nabla \times \boldsymbol{A}(\boldsymbol{r})\right) = j\omega\epsilon\left[-j\omega\boldsymbol{A}(\boldsymbol{r}) - \nabla\phi_e\right] + \boldsymbol{J}(\boldsymbol{r}),$$

which, by using some vector identities, can be rewritten as

$$\nabla^2\boldsymbol{A}(\boldsymbol{r}) + k^2\boldsymbol{A}(\boldsymbol{r}) = \nabla(j\omega\mu\epsilon\phi_e(\boldsymbol{r}) + \nabla\cdot\boldsymbol{A}(\boldsymbol{r})) - \mu\boldsymbol{J}(\boldsymbol{r}), \tag{1.19}$$

where the wave number amplitude $k = \omega\sqrt{\mu\epsilon}$ is introduced. In second place, divergence equation 1.14 can be expressed as

$$\nabla\cdot(-j\omega\boldsymbol{A}(\boldsymbol{r}) - \nabla\phi_e(\boldsymbol{r})) = -\frac{\rho_e(\boldsymbol{r})}{\epsilon},$$

which, adding the quantity $k^2\phi_e = -j\omega(j\omega\epsilon\mu\phi_e)$ at both sides, becomes

$$\nabla^2\phi_e(\boldsymbol{r}) + k^2\phi_e(\boldsymbol{r}) = -\frac{\rho_e(\boldsymbol{r})}{\epsilon} - j\omega(j\omega\mu\epsilon\phi_e(\boldsymbol{r}) + \nabla\cdot\boldsymbol{A}(\boldsymbol{r})). \tag{1.20}$$

Since only $\nabla\times\boldsymbol{A}$ is imposed from eq. (1.17), divergence of the vector potential can be set freely. A common choice is the one that allows to simplify the right hand sides (RHSs) in equations 1.19 and 1.20, called the Lorenz gauge:

$$\nabla\cdot\boldsymbol{A}(\boldsymbol{r}) = -j\omega\mu\epsilon\phi_e(\boldsymbol{r}). \tag{1.21}$$

Under this condition, vector and scalar electric potentials are such to satisfy the inhomogeneous Helmholtz equation in vector and scalar form respectively:

$$\nabla^2\boldsymbol{A}(\boldsymbol{r}) + k^2\boldsymbol{A}(\boldsymbol{r}) = -\mu\boldsymbol{J}(\boldsymbol{r}) \tag{1.22}$$

$$\nabla^2\phi_e(\boldsymbol{r}) + k^2\phi_e(\boldsymbol{r}) = -\frac{\rho_e(\boldsymbol{r})}{\epsilon}. \tag{1.23}$$

1.4.2 Potentials for magnetic sources

Consider now sources of magnetic type only. The potentials for magnetic sources, $\boldsymbol{F}$ and ϕ_m, can be found by following similar steps as in the electric sources case. In this respect, the electric flux density is solenoidal, so it can be written as

$$\boldsymbol{D}(\boldsymbol{r}) = -\nabla \times \boldsymbol{F}(\boldsymbol{r}). \tag{1.24}$$

By replacing eq. (1.24) into eq. (1.16), the relation between magnetic field and magnetic potentials is clarified as

$$\boldsymbol{H}(\boldsymbol{r}) + j\omega \boldsymbol{F}(\boldsymbol{r}) = -\nabla \phi_m(\boldsymbol{r}), \tag{1.25}$$

where $\boldsymbol{F}$ is the vector magnetic potential, in A·s/m, ϕ_m is the scalar magnetic potential, in A. By imposing the Lorenz gauge,

$$\nabla \cdot \boldsymbol{F}(\boldsymbol{r}) = -j\omega\mu\epsilon\phi_m(\boldsymbol{r}), \tag{1.26}$$

the relations between potentials and sources are expressed as Helmholtz equations in vector and scalar form:

$$\nabla^2 \boldsymbol{F}(\boldsymbol{r}) + k^2 \boldsymbol{F}(\boldsymbol{r}) = -\epsilon \boldsymbol{M}(\boldsymbol{r}) \tag{1.27}$$

$$\nabla^2 \phi_m(\boldsymbol{r}) + k^2 \phi_m(\boldsymbol{r}) = -\frac{\rho_m(\boldsymbol{r})}{\mu}. \tag{1.28}$$

1.4.3 Green's function and scattered field

In order to find an analytic solution for the potentials described so far, it is necessary to solve the inhomogeneous Helmholtz equation. Green's function approach will be exploited to this purpose [4]: it consists of looking for the solution of the problem under study in case of point source excitation, represented by a Dirac delta function. This solution is called Green's function or fundamental solution, denoted with the letter G. Then, the solution of the original Helmholtz equation will be obtained by convoluting G with the actual source, by virtue of superposition principle. In formulae, the Green's function satisfies

$$\nabla^2 G(\boldsymbol{r}) + k^2 G(\boldsymbol{r}) = -\delta(\boldsymbol{r}). \tag{1.29}$$

This equation admits unique solution just if the boundary condition of outgoing waves only is imposed at infinity, called Sommerfeld's radiation condition. Expression of the three-dimensional free space Green's function is

$$G(\boldsymbol{r}) = \frac{e^{-jk|\boldsymbol{r}|}}{4\pi|\boldsymbol{r}|}. \tag{1.30}$$

By convoluting both sides of eq. (1.29) with the right hand sides of equations 1.22, 1.23, 1.27, 1.28 and comparing what obtained with the just mentioned equations, potentials $\boldsymbol{A}$, ϕ_e, $\boldsymbol{F}$, ϕ_m are respectively obtained as

$$\boldsymbol{A}(\boldsymbol{r}) = \mu \iiint_{r' \in \mathbb{R}^3} G(\boldsymbol{r} - \boldsymbol{r'}) \boldsymbol{J}(\boldsymbol{r'}) dV' \tag{1.31}$$

$$\phi_e(\boldsymbol{r}) = \frac{1}{\epsilon} \iiint_{r' \in \mathbb{R}^3} G(\boldsymbol{r} - \boldsymbol{r'}) \rho_e(\boldsymbol{r'}) dV' \tag{1.32}$$

$$\boldsymbol{F}(\boldsymbol{r}) = \epsilon \iiint_{r' \in \mathbb{R}^3} G(\boldsymbol{r} - \boldsymbol{r'}) \boldsymbol{M}(\boldsymbol{r'}) dV' \tag{1.33}$$

$$\phi_m(\boldsymbol{r}) = \frac{1}{\mu} \iiint_{r' \in \mathbb{R}^3} G(\boldsymbol{r} - \boldsymbol{r'}) \rho_m(\boldsymbol{r'}) dV'. \tag{1.34}$$

Summing up the contributions, electric and magnetic fields scattered from both electric and magnetic sources are written as

$$\boldsymbol{E}(\boldsymbol{r}) = -j\omega \boldsymbol{A}(\boldsymbol{r}) - \nabla \phi_e(\boldsymbol{r}) - \frac{1}{\epsilon} \nabla \times \boldsymbol{F}(\boldsymbol{r}) \tag{1.35}$$

$$\boldsymbol{H}(\boldsymbol{r}) = -j\omega \boldsymbol{F}(\boldsymbol{r}) - \nabla \phi_m(\boldsymbol{r}) + \frac{1}{\mu} \nabla \times \boldsymbol{A}(\boldsymbol{r}) \tag{1.36}$$

or equivalently, given the Lorenz gauge considered, as

$$\boldsymbol{E}(\boldsymbol{r}) = -j\omega \boldsymbol{A}(\boldsymbol{r}) + \frac{1}{j\omega\mu\epsilon} \nabla \nabla \cdot \boldsymbol{A}(\boldsymbol{r}) - \frac{1}{\epsilon} \nabla \times \boldsymbol{F}(\boldsymbol{r}) \tag{1.37}$$

$$\boldsymbol{H}(\boldsymbol{r}) = -j\omega \boldsymbol{F}(\boldsymbol{r}) + \frac{1}{j\omega\mu\epsilon} \nabla \nabla \cdot \boldsymbol{F}(\boldsymbol{r}) + \frac{1}{\mu} \nabla \times \boldsymbol{A}(\boldsymbol{r}). \tag{1.38}$$

1.5 Maxwell's equations in statics

The Maxwell's system and the scattering equations seen so far can be specialized for the static and quasi-static regimes. The first arises when the simulation frequency is exactly zero; we name quasi-static regime instead a frequency regime in which particular approximations can be taken, better specified in the following.

1.5.1 The static regime

In case the frequency is exactly zero, electric and magnetic fields are fully decoupled and the Maxwell's system reads

$$\nabla \times \boldsymbol{E}(\boldsymbol{r}, \omega) = -\boldsymbol{M}(\boldsymbol{r}, \omega) \tag{1.39}$$

$$\nabla \times \boldsymbol{H}(\boldsymbol{r}, \omega) = \boldsymbol{J}(\boldsymbol{r}, \omega). \tag{1.40}$$

Assuming to work with physical (electrical) sources only, eq. (1.39) states that the electric field is irrotational. It follows that the static electric field over simply connected domains is conservative:

$$\oint_C \boldsymbol{E} \cdot d\boldsymbol{l} = 0. \tag{1.41}$$

In this case, the notion of electric potential ϕ_e is introduced and widely exploited in circuit analysis. Indeed, in this context, independence of potential difference, or voltage, from the path along which is measured (eq. (1.41)) is better known as Kirchhoff Voltage Law (KVL) [5]. It is to be noticed that the relation $E = -\nabla\phi_e$ obtained is just a specialization of eq. (1.18) in the static case and with electric sources only.

Kirchhoff Current Law (KCL) [6, 7], the other pillar on which circuit analysis is based, is derived instead from eq. (1.40). Recalling the definition of current flowing through an open surface S_o enclosed by the contour C_o and applying the Stokes theorem, a relation with the circulation of the magnetic field is obtained:

$$I = \iint_{S_o} \boldsymbol{J}(\boldsymbol{r}) \cdot d\boldsymbol{S} = \iint_{S_o} (\nabla \times \boldsymbol{H}(\boldsymbol{r})) \cdot d\boldsymbol{S} = \oint_{C_o} \boldsymbol{H}(\boldsymbol{r}) \cdot d\boldsymbol{l}. \tag{1.42}$$

Relations in 1.42 are also valid for a close surface S_c, whose enclosing contour C_c vanishes. From this consideration, it is clear that the total current flowing through the close surface S_c, given by the difference between ingoing and outgoining currents, is null.

1.5.2 The quasi-static regime

For frequencies different from zero, Kirchhoff voltage and current laws are not valid anymore, but a coupling is observed between electric and magnetic fields:

$$\oint_C \boldsymbol{E}(\boldsymbol{r}) \cdot d\boldsymbol{l} = -j\omega \iint_S \boldsymbol{B}(\boldsymbol{r}) \cdot d\boldsymbol{S} \tag{1.43}$$

$$I = \iint_S \boldsymbol{J}(\boldsymbol{r}) \cdot d\boldsymbol{S} = \oint_C \boldsymbol{H}(\boldsymbol{r}) \cdot d\boldsymbol{l} - j\omega \iint_S \boldsymbol{D}(\boldsymbol{r}) \cdot d\boldsymbol{S}. \tag{1.44}$$

The coupling term $j\omega \iint_S \boldsymbol{B}(\boldsymbol{r}) \cdot d\boldsymbol{S}$ in eq. (1.43) can be safely neglected if its modulus is lower than the smallest value of voltage we want to measure in the circuit. In the same way, the term $j\omega \iint_S \boldsymbol{D}(\boldsymbol{r}) \cdot d\boldsymbol{S}$ in eq. (1.44), which takes into account displacement electric current, can be neglected if lower than the smallest value of current to be measured. It is clear that the possibility to perform these simplifications depends on the source as well as on the object under test, in particular on its dimensions and physical parameters [8].

Simplification of eq. (1.43), which leads to the KVL, is customarily called electro-quasistatic approximation (EQS), while simplification of eq. (1.44), which brings to the KCL , is named magneto-quasistatic (MQS) approximation. Summing up, the Maxwell's system, given electric sources only, under the electro-quasistatic regime is reduced to

$$\nabla \times \boldsymbol{E}(\boldsymbol{r}, \omega) = 0 \tag{1.45}$$

$$\nabla \times \boldsymbol{H}(\boldsymbol{r}, \omega) = j\omega \boldsymbol{D}(\boldsymbol{r}, \omega) + \boldsymbol{J}(\boldsymbol{r}, \omega), \tag{1.46}$$

under magneto-quasistatic regime to

$$\nabla \times \boldsymbol{E}(\boldsymbol{r}, \omega) = -j\omega \boldsymbol{B}(\boldsymbol{r}, \omega) \tag{1.47}$$

$$\nabla \times \boldsymbol{H}(\boldsymbol{r}, \omega) = \boldsymbol{J}(\boldsymbol{r}, \omega). \tag{1.48}$$

It's interesting to notice that in both regimes the coupling between electric and magnetic induction is neglected. The choice of the approximation to be used is dictated by considerations about static fields: if, in static conditions, the electric field is dominant with respect to the magnetic field, the EQS approximation could be suitable to represent the problem; if, vice versa, the magnetic field is dominant, the MQS approximation should be taken into account. Typical examples of the two situations just described are respectively a capacitor excited by a voltage generator, whose plates result charged in static conditions but no current flows between them, and an inductor excited by a current generator, in which the circulating current is responsible for the magnetic field generation.

Chapter 2

Integral equations and preconditioning

2.1 Integral equation formulation

2.1.1 Boundary conditions

Differential form of the Maxwell's system is not valid in presence of material discontinuities, since the fields or their derivatives are not continuous at the boundaries between different media. Some relations between the interior and exterior limits of the electric and magnetic fields at these boundaries can be derived from the Maxwell's system in integral form, valid in any case.

Consider the region of space Ω_1 and its smooth boundary Γ, characterized by the outgoing unit surface normal vector $\hat{\boldsymbol{n}}$. The limits of the fields at the boundary outside and inside the region Ω_1 are denoted with the superscripts $^{0/1}$. They satisfy the following boundary conditions:

$$\hat{\boldsymbol{n}} \times (\boldsymbol{E}^0 - \boldsymbol{E}^1) = -\boldsymbol{m}_s \tag{2.1}$$

$$\hat{\boldsymbol{n}} \times (\boldsymbol{H}^0 - \boldsymbol{H}^1) = \boldsymbol{j}_s \tag{2.2}$$

$$\hat{\boldsymbol{n}} \cdot (\boldsymbol{D}^0 - \boldsymbol{D}^1) = \rho_{e,s} \tag{2.3}$$

$$\hat{\boldsymbol{n}} \cdot (\boldsymbol{B}^0 - \boldsymbol{B}^1) = \rho_{m,s}. \tag{2.4}$$

In the previous equations, the subscript $_s$ represents surface quantities: surface current densities, in A/m and V/m, and surface charge densities, in A·s/m^2 and V·s/m^2.

These two couples of conditions are not independent; usually, just the first of them is explicitly enforced in the definition of an integral equation. Moreover, it's important to recall that surface currents and charges are vanishing in case of real

materials, leading to the well-known conditions of continuity of tangential traces of the fields and of normal components of the flux densities. Instead, the surface of a perfect electric conductor (PEC) can support surface electric currents and charges; surface magnetic currents and charges are theoretically possible on the surface of a perfect magnetic conductor (PMC).

2.1.2 The surface equivalence principle

The surface equivalence principle states that the electromagnetic field inside a source-free region Ω is completely determined if the tangential traces of the electric and magnetic fields are known over the surface $\Gamma = \partial\Omega$. It is commonly exploited in the building of boundary integral equations, to reformulate the original problem into a new, equivalent, free-space scattering problem, whose analytic solution has been derived in section 1.4.

Consider for example the problem of scattering from the object Ω_1, with material parameters (ϵ_1, μ_1), subject to an excitation from the outside region $\Omega_0 = \mathbb{R}^3 \backslash \Omega_1$, characterized by (ϵ_0, μ_0) (fig. 2.1) . The boundary between regions Ω_0 and Ω_1 is the surface Γ, characterized in each point by the outgoing (with respect to Ω_1) unit surface normal vector $\hat{\boldsymbol{n}}$. The excitation $(\boldsymbol{E}^{inc}, \boldsymbol{H}^{inc})$ induces some currents in the interior of Ω_1, $(\boldsymbol{j}, \boldsymbol{m})$, which in turn are the sources of the scattered fields $(\boldsymbol{E}^{sc}, \boldsymbol{H}^{sc})$. Evaluation of the scattered field from a knowledge of the incident field is the so-called direct scattering problem.

In order to determine the total field, given by superposition of incident and scattered field, not only currents $(\boldsymbol{j}, \boldsymbol{m})$ are to be retrieved, but also the scattering operators, i.e. the Green's function, specific to geometry and material parameters under test, to link the scattered fields to their sources. In general, this information is not available for non-canonical geometries of the scatterer.

It is to be noticed that free-space electromagnetic scattering solution has been presented in section 1.4. Surface equivalence principle can be exploited to conduct the original problem to the one of free-space scattering. To this purpose, it is desirable to replace true fields inside the scatterer $(\boldsymbol{E}, \boldsymbol{H})$ and true (eventual) surface current densities $(\boldsymbol{j}_{s,0}, \boldsymbol{m}_{s,0})$ at the boundary with some other quantities, denoted as $(\boldsymbol{E}', \boldsymbol{H}')$, $(\boldsymbol{j}_s, \boldsymbol{m}_s)$ containing the same amount of information, such as the fields outside are left unchanged. In particular, equivalence of new and original problems in Ω_0 holds if the boundary conditions

$$\hat{\boldsymbol{n}} \times (\boldsymbol{E}^0 - \boldsymbol{E}'^1) = -\boldsymbol{m}_s \tag{2.5a}$$

$$\hat{\boldsymbol{n}} \times (\boldsymbol{H}^0 - \boldsymbol{H}'^1) = \boldsymbol{j}_s \tag{2.5b}$$

are satisfied. A favorable choice is the so-called Love formulation: interior fields are set to zero (scattered fields are such to balance the incident ones), so that unknown

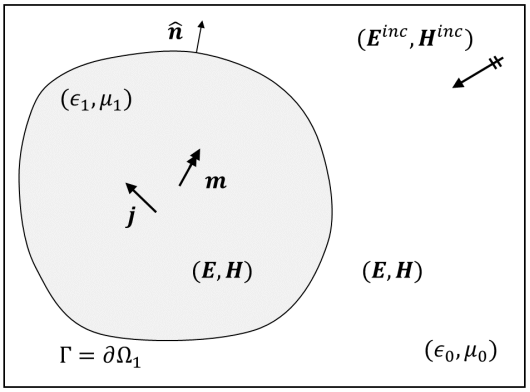

Figure 2.1: Original direct scattering problem.

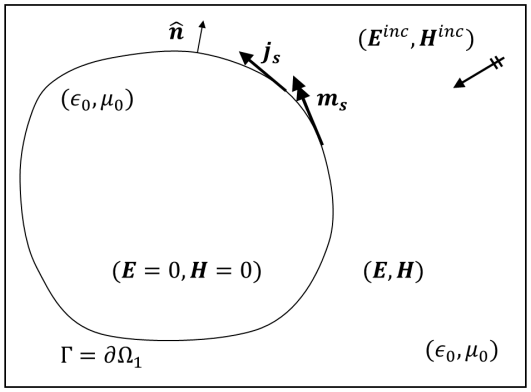

Figure 2.2: Love equivalent formulation of the original exterior scattering problem.

surface current densities have to satisfy

$$\hat{\boldsymbol{n}} \times \boldsymbol{E}^0 = -\boldsymbol{m}_s \tag{2.6a}$$

$$\hat{\boldsymbol{n}} \times \boldsymbol{H}^0 = \boldsymbol{j}_s. \tag{2.6b}$$

Since electric and magnetic fields inside Ω_1 are null, material parameters of the scatterer can be replaced with (ϵ_0, μ_0) of background medium without affecting the problem. So, a free-space scattering problem is obtained: scattered fields outside $(\boldsymbol{E}^{sc}, \boldsymbol{H}^{sc})$ can be reconstructed from scattering of the fictitious surface currents $(\boldsymbol{j}_s, \boldsymbol{m}_s)$ through formulae 1.37 and 1.38. Since currents $(\boldsymbol{j}_s, \boldsymbol{m}_s)$ are defined on a surface instead than on a volume, electric and magnetic vector potentials can be rewritten as

$$\boldsymbol{A}(\boldsymbol{r}) = \mu \iint_{r' \in \Gamma} G(\boldsymbol{r} - \boldsymbol{r'}) \boldsymbol{j}_s(\boldsymbol{r'}) dS' \tag{2.7}$$

$$\boldsymbol{F}(\boldsymbol{r}) = \epsilon \iint_{r' \in \Gamma} G(\boldsymbol{r} - \boldsymbol{r'}) \boldsymbol{m}_s(\boldsymbol{r'}) dS'. \tag{2.8}$$

2.1.3 The electric and magnetic field integral equations

Electric and magnetic field integral equations (EFIE and MFIE) are two of the most common integral equations in computational electromagnetics; they are based respectively on boundary conditions 2.1 and 2.2.

Given the scattering problem presented in section 2.1.2 reformulated by means of the Love formulation of the surface equivalence principle, boundary conditions

are written as

$$\hat{\boldsymbol{n}}(\boldsymbol{r}) \times (\boldsymbol{E}^{inc}(\boldsymbol{r}) + \boldsymbol{E}^{sc}(\boldsymbol{r})) = -\boldsymbol{m}_s(\boldsymbol{r}) \tag{2.9a}$$

$$\hat{\boldsymbol{n}}(\boldsymbol{r}) \times (\boldsymbol{H}^{inc}(\boldsymbol{r}) + \boldsymbol{H}^{sc}(\boldsymbol{r})) = \boldsymbol{j}_s(\boldsymbol{r}). \tag{2.9b}$$

Scattered fields $(\boldsymbol{E}^{sc}, \boldsymbol{H}^{sc})$ can be expressed more explicitly by means of radiation formulae 1.37 and 1.38 containing potentials in eq. (2.7) and eq. (2.8). Special care must be taken in this operation, since the potentials' expressions contain a singularity when evaluated on the boundary Γ.

Before exploring potentials' behaviour at the boundary, it is convenient to manipulate some of the terms in eq. (1.37) and eq. (1.38) by means of vector calculus identities. The following identities can be obtained:

$$\nabla \cdot \iint_{r' \in \Gamma} G(\boldsymbol{r} - \boldsymbol{r'}) \boldsymbol{f}(\boldsymbol{r'}) dS' = \iint_{r' \in \Gamma} G(\boldsymbol{r} - \boldsymbol{r'}) \nabla' \cdot \boldsymbol{f}(\boldsymbol{r'}) dS' \tag{2.10}$$

$$\nabla \times \iint_{r' \in \Gamma} G(\boldsymbol{r} - \boldsymbol{r'}) \boldsymbol{f}(\boldsymbol{r'}) dS' = \iint_{r' \in \Gamma} \nabla G(\boldsymbol{r} - \boldsymbol{r'}) \times \boldsymbol{f}(\boldsymbol{r'}) dS' \tag{2.11}$$

where $\boldsymbol{f}$ stands for $\boldsymbol{j}_s$ or $\boldsymbol{m}_s$ and primed operators are taken with respect to the primed variable $\boldsymbol{r'}$.

Jump relations

Boundary integral equations' formalism take advantage of the concepts of single and double layer potentials [9–11], defined as

$$(Sv)(\boldsymbol{r}) = \iint_{\Gamma} G(\boldsymbol{r} - \boldsymbol{r'}) v(\boldsymbol{r'}) dS' \quad \boldsymbol{r} \in \mathbb{R}^3 \backslash \Gamma \tag{2.12}$$

$$(Dv)(\boldsymbol{r}) = \iint_{\Gamma} \gamma_1' G(\boldsymbol{r} - \boldsymbol{r'}) v(\boldsymbol{r'}) dS' \quad \boldsymbol{r} \in \mathbb{R}^3 \backslash \Gamma \tag{2.13}$$

where γ_1' represents the normal derivative operator. S and D are harmonic operators: they represent a solution of the Laplace equation for any $\boldsymbol{r} \in \mathbb{R}^3 \backslash \Gamma$, for any density function v. Well known properties of these potentials are the following:

- the single layer potential is continuous across Γ: $[S\phi] = 0$;
- the double layer potential is discontinuous across Γ: $[D\psi] = \psi$.
- the normal derivative of the single layer potential is discontinuous across Γ: $[\gamma_1 S\phi] = -\phi$;
- the normal derivative of the double layer potential is continuous across Γ: $[\gamma_1 D\psi] = 0$.

More rigorous formalism and proofs of the results given in this section can be found in [9, 10]. From the jump relations just mentioned (from the first and the third in particular), it is clear that the tangential traces of the terms $\boldsymbol{A}(\boldsymbol{r})$ and $\nabla\nabla\cdot\boldsymbol{A}(\boldsymbol{r})$ in equation 1.37 are continuous across the boundary. More formally, given $\boldsymbol{r}_0 \in \Gamma$,

$$\lim_{\boldsymbol{r}\to\boldsymbol{r}_0} \hat{\boldsymbol{n}}(\boldsymbol{r}) \times \boldsymbol{A}(\boldsymbol{r}) = \hat{\boldsymbol{n}}(\boldsymbol{r}_0) \times \boldsymbol{A}(\boldsymbol{r}_0) \tag{2.14}$$

$$\lim_{\boldsymbol{r}\to\boldsymbol{r}_0} \hat{\boldsymbol{n}}(\boldsymbol{r}) \times (\nabla\nabla\cdot\boldsymbol{A}(\boldsymbol{r})) = \hat{\boldsymbol{n}}(\boldsymbol{r}_0) \times (\nabla\nabla\cdot\boldsymbol{A}(\boldsymbol{r}_0))\,. \tag{2.15}$$

On the other hand, the tangential trace of the curl of $\boldsymbol{F}$ is discontinuous across Γ and the jump height is given by the tangential trace of $\boldsymbol{m}_s(\boldsymbol{r})$. So, for $\boldsymbol{r} \in \Omega_{0/1}$,

$$\begin{aligned}\lim_{\boldsymbol{r}\to\boldsymbol{r}_0} \hat{\boldsymbol{n}}(\boldsymbol{r}) \times (\nabla \times \boldsymbol{F}(\boldsymbol{r})) = \pm\frac{1}{2}\boldsymbol{m}_s(\boldsymbol{r}_0) \\ + \hat{\boldsymbol{n}}(\boldsymbol{r}_0) \times p.v. \iint_{r'\in\Gamma} \nabla G(\boldsymbol{r}-\boldsymbol{r}') \times \boldsymbol{m}_s(\boldsymbol{r}')dS'.\end{aligned} \tag{2.16}$$

Similar results can be obtained also for the terms in equation 1.38 relative to magnetic scattering. Finally, tangential traces of the scattered fields $(\boldsymbol{E}^{sc}, \boldsymbol{H}^{sc})$ evaluated in points $\boldsymbol{r}$ approaching the surface Γ from outside are rewritten as

$$\begin{aligned}\hat{\boldsymbol{n}}(\boldsymbol{r}) \times \boldsymbol{E}^{sc}(\boldsymbol{r}) = &-jk\eta\hat{\boldsymbol{n}}(\boldsymbol{r}) \times \iint_{\boldsymbol{r}'\in\Gamma} G(\boldsymbol{r}-\boldsymbol{r}')\boldsymbol{j}_s(\boldsymbol{r}')d\boldsymbol{r}' \\ &+ \frac{\eta}{jk}\hat{\boldsymbol{n}}(\boldsymbol{r}) \times \nabla \iint_{\boldsymbol{r}'\in\Gamma} G(\boldsymbol{r}-\boldsymbol{r}')\nabla'\cdot\boldsymbol{j}_s(\boldsymbol{r}')d\boldsymbol{r}' \\ &- \frac{1}{2}\boldsymbol{m}_s \\ &- \hat{\boldsymbol{n}}(\boldsymbol{r}) \times \text{p.v.} \iint_{\boldsymbol{r}'\in\Gamma} \nabla G(\boldsymbol{r}-\boldsymbol{r}') \times \boldsymbol{m}_s(\boldsymbol{r}')d\boldsymbol{r}'\end{aligned} \tag{2.17}$$

$$\begin{aligned}\hat{\boldsymbol{n}}(\boldsymbol{r}) \times \boldsymbol{H}^{sc}(\boldsymbol{r}) = &-\frac{jk}{\eta}\hat{\boldsymbol{n}}(\boldsymbol{r}) \times \iint_{\boldsymbol{r}'\in\Gamma} G(\boldsymbol{r}-\boldsymbol{r}')\boldsymbol{m}_s(\boldsymbol{r}')d\boldsymbol{r}' \\ &+ \frac{1}{jk\eta}\hat{\boldsymbol{n}}(\boldsymbol{r}) \times \nabla \iint_{\boldsymbol{r}'\in\Gamma} G(\boldsymbol{r}-\boldsymbol{r}')\nabla'\cdot\boldsymbol{m}_s(\boldsymbol{r}')d\boldsymbol{r}' \\ &+ \frac{1}{2}\boldsymbol{j}_s \\ &+ \hat{\boldsymbol{n}}(\boldsymbol{r}) \times \text{p.v.} \iint_{\boldsymbol{r}'\in\Gamma} \nabla G(\boldsymbol{r}-\boldsymbol{r}') \times \boldsymbol{j}_s(\boldsymbol{r}')d\boldsymbol{r}',\end{aligned} \tag{2.18}$$

where η is the impedance of background medium. By substituting these expressions in equations 2.9a and 2.9b, the electric and magnetic field integral equations are obtained. In order to shorten these expressions, it is convenient to introduce surface integral operators.

Surface integral operators

The electric field integral operator $\mathcal{T}_k$ is defined as a linear combination of the vector and the scalar electric potential operators, $\mathcal{T}_{\boldsymbol{A},k}$ and $\mathcal{T}_{\phi,k}$:

$$\mathcal{T}_k = -jk\mathcal{T}_{\boldsymbol{A},k} + \frac{1}{jk}\mathcal{T}_{\phi,k} \tag{2.19}$$

$$(\mathcal{T}_{\boldsymbol{A},k}\boldsymbol{f})(\boldsymbol{r}) = \hat{\boldsymbol{n}}(\boldsymbol{r}) \times \iint_\Gamma G_k(\boldsymbol{r},\boldsymbol{r}')\boldsymbol{f}(\boldsymbol{r}')d\boldsymbol{r}' \tag{2.20}$$

$$(\mathcal{T}_{\phi,k}\boldsymbol{f})(\boldsymbol{r}) = \hat{\boldsymbol{n}}(\boldsymbol{r}) \times \nabla \iint_\Gamma G_k(\boldsymbol{r},\boldsymbol{r}')\nabla' \cdot \boldsymbol{f}(\boldsymbol{r}')d\boldsymbol{r}'. \tag{2.21}$$

The magnetic field integral operator $\mathcal{K}_k$ is defined as

$$(\mathcal{K}_k\boldsymbol{f})(\boldsymbol{r}) = \hat{\boldsymbol{n}}(\boldsymbol{r}) \times \iint_\Gamma \nabla G_k(\boldsymbol{r},\boldsymbol{r}') \times \boldsymbol{f}(\boldsymbol{r}')d\boldsymbol{r}'. \tag{2.22}$$

Given the above definitions, the EFIE and MFIE relative to the exterior problem can be written as

$$-\hat{\boldsymbol{n}} \times \boldsymbol{E}^{inc} = \eta\,\mathcal{T}_k\,\boldsymbol{j}_s + \frac{1}{2}\,\boldsymbol{m}_s - \mathcal{K}_k\,\boldsymbol{m}_s \tag{2.23}$$

$$\hat{\boldsymbol{n}} \times \boldsymbol{H}^{inc} = -\frac{1}{\eta}\,\mathcal{T}_k\,\boldsymbol{m}_s + \frac{1}{2}\,\boldsymbol{j}_s - \mathcal{K}_k\,\boldsymbol{j}_s. \tag{2.24}$$

In these equations, the surface operators operate on the surface currents $(\boldsymbol{j}_s, \boldsymbol{m}_s)$ and are evaluated on the surface Γ. Solution of the system given by eq. (2.23) and eq. (2.24), which can be rewritten in matrix block form as

$$\begin{pmatrix} \eta\,\mathcal{T}_k & \frac{\mathcal{I}}{2} - \mathcal{K}_k \\ \frac{\mathcal{I}}{2} - \mathcal{K}_k & -\frac{1}{\eta}\,\mathcal{T}_k \end{pmatrix} \begin{pmatrix} \boldsymbol{j}_s \\ \boldsymbol{m}_s \end{pmatrix} = \begin{pmatrix} -\hat{\boldsymbol{n}} \times \boldsymbol{E}^{inc} \\ \hat{\boldsymbol{n}} \times \boldsymbol{H}^{inc} \end{pmatrix}, \tag{2.25}$$

provides information about the fictitious surface currents, from which the scattered fields in Ω_0 can be evaluated. Once the quantities $(\boldsymbol{j}_s, \boldsymbol{m}_s)$ are determined, the exterior scattering problem is considered solved.

2.1.4 The PMCHWT integral equation

The Poggio-Miller-Chang-Harrington-Wu-Tsai equation [12] is an integral formulation which allows to solve at once the interior and the exterior scattering by a penetrable dielectric object.

In the following we will consider a dielectric scatterer Ω_1 with parameters (ϵ_1, μ_1) subject to an excitation from the outside region Ω_0 characterized by (ϵ_0, μ_0). The formulation can be applied to bodies with finite conductivity σ, such that electric permittivity $\epsilon_1 = \epsilon_0\epsilon_r' - j\sigma/\omega$ can take complex values.

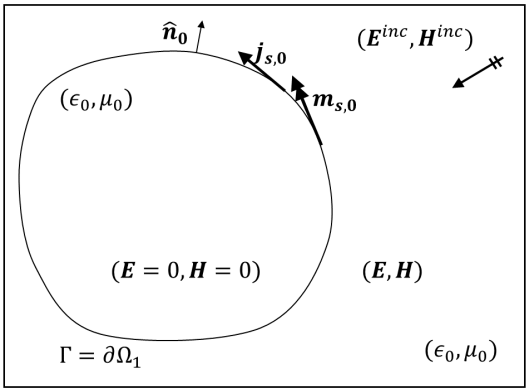

Figure 2.3: Application of surface equivalence principle, exterior problem.

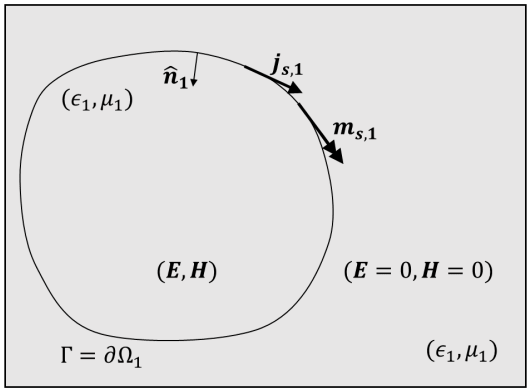

Figure 2.4: Application of surface equivalence principle, interior problem.

The original problem is solved by means of the superposition principle in the Love formulation: at first, the exterior problem is considered (fig. 2.3), in which the excitation is turned on; then the interior one, with excitation off (fig. 2.4). The boundary conditions relative to the exterior problem are written as

$$-\hat{\boldsymbol{n}}_0 \times \boldsymbol{E}^{inc} = \eta_0 \, \mathcal{T}_{k_0} \, \boldsymbol{j}_{s,0} + \frac{1}{2} \, \boldsymbol{m}_{s,0} - \mathcal{K}_{k0} \, \boldsymbol{m}_{s,0} \tag{2.26}$$

$$\hat{\boldsymbol{n}}_0 \times \boldsymbol{H}^{inc} = -\frac{1}{\eta_0} \, \mathcal{T}_{k0} \, \boldsymbol{m}_{s,0} + \frac{1}{2} \, \boldsymbol{j}_{s,0} - \mathcal{K}_{k0} \, \boldsymbol{j}_{s,0}, \tag{2.27}$$

with $\boldsymbol{j}_{s,0} = \hat{\boldsymbol{n}}_0 \times \boldsymbol{H}_0$, $\boldsymbol{m}_{s,0} = -\hat{\boldsymbol{n}}_0 \times \boldsymbol{E}_0$. EFIE and MFIE relative to the interior problem read instead

$$0 = \eta_1 \, \mathcal{T}_{k_1} \, \boldsymbol{j}_{s,1} - \frac{1}{2} \, \boldsymbol{m}_{s,1} - \mathcal{K}_{k1} \, \boldsymbol{m}_{s,1} \tag{2.28}$$

$$0 = -\frac{1}{\eta_1} \, \mathcal{T}_{k1} \, \boldsymbol{m}_{s,1} - \frac{1}{2} \, \boldsymbol{j}_{s,1} - \mathcal{K}_{k1} \, \boldsymbol{j}_{s,1}, \tag{2.29}$$

with $\boldsymbol{j}_{s,1} = \hat{\boldsymbol{n}}_1 \times \boldsymbol{H}_1$, $\boldsymbol{m}_{s,1} = -\hat{\boldsymbol{n}}_1 \times \boldsymbol{E}_1$. Given the continuity of the tangential traces of the fields at the boundary and since $\hat{\boldsymbol{n}}_0 = -\hat{\boldsymbol{n}}_1 =: \hat{\boldsymbol{n}}$,

$$\boldsymbol{j}_{s,0} = -\boldsymbol{j}_{s,1} =: \boldsymbol{j}_s \tag{2.30}$$

$$\boldsymbol{m}_{s,0} = -\boldsymbol{m}_{s,1} =: \boldsymbol{m}_s. \tag{2.31}$$

This fundamental step allows to recognize that the exterior and interior problems, independent of each other, share the same unknown variables $\boldsymbol{j}_s$ and $\boldsymbol{m}_s$. So, it is possible to sum the two sets of equations, canceling the identity terms, to reach

the final formulation

$$\begin{cases} -\hat{\boldsymbol{n}} \times \boldsymbol{E}^{inc} = \eta_0 \mathcal{T}_{k_0} \boldsymbol{j}_s + \eta_1 \mathcal{T}_{k_1} \boldsymbol{j}_s - \mathcal{K}_{k0} \boldsymbol{m}_s - \mathcal{K}_{k1} \boldsymbol{m}_s \\ -\hat{\boldsymbol{n}} \times \boldsymbol{H}^{inc} = \frac{1}{\eta_0} \mathcal{T}_{k_0} \boldsymbol{m}_s + \frac{1}{\eta_1} \mathcal{T}_{k_1} \boldsymbol{m}_s + \mathcal{K}_{k0} \boldsymbol{j}_s + \mathcal{K}_{k1} \boldsymbol{j}_s. \end{cases} \tag{2.32}$$

More compactly, under block matrix form, it reads

$$\begin{pmatrix} \eta_0 \mathcal{T}_{k_0} + \eta_1 \mathcal{T}_{k_1} & -(\mathcal{K}_{k_0} + \mathcal{K}_{k_1}) \\ \mathcal{K}_{k_0} + \mathcal{K}_{k_1} & \frac{1}{\eta_0} \mathcal{T}_{k_0} + \frac{1}{\eta_1} \mathcal{T}_{k_1} \end{pmatrix} \begin{pmatrix} \boldsymbol{j}_s \\ \boldsymbol{m}_s \end{pmatrix} = \begin{pmatrix} -\hat{\boldsymbol{n}} \times \boldsymbol{E}^{inc} \\ -\hat{\boldsymbol{n}} \times \boldsymbol{H}^{inc} \end{pmatrix}. \tag{2.33}$$

2.2 The boundary element method

Integral equations presented in the previous sections can be solved numerically by means of the boundary element method (BEM), a technique which applies the method of moments to a boundary value problem.

Consider for example the electric field integral equation for PEC materials,

$$\eta \mathcal{T}_k \boldsymbol{j}_s = -\hat{\boldsymbol{n}} \times \boldsymbol{E}^{inc}. \tag{2.34}$$

Null electric field inside a PEC object, leading to null magnetic surface current, is a condition required to assume finite current inside the object. $\mathcal{T}_k$ is a linear operator; the unknown current $\boldsymbol{j}_s$ and the RHS $\boldsymbol{b} \coloneqq (-\hat{\boldsymbol{n}} \times \boldsymbol{E}^{inc})$ are functions in the space $\{\Gamma \to \mathbb{C}^3\}$. By means of the method of moment, the problem is transformed into the linear system

$$\eta \mathbf{T}\, \mathrm{j} = \mathrm{b} \tag{2.35}$$

where the matrix $\mathbf{T}$ is the discretization of the EFIO; the arrays j and b represent instead a discretization of the vector fields $\boldsymbol{j}_s$ and $\boldsymbol{b}$. What is meant by discretization in this context is better explained in the following.

First of all, in order to numerically solve the boundary integral equation (BIE) in eq. (2.34), it is necessary to discretize the surface Γ, usually by means of flat triangular elements; the outcome of this operation is called mesh. The level of accuracy by which a mesh approximates Γ is mainly dictated by the average edge length h. It should be chosen in such a way to satisfy at the same time the Nyquist-Shannon sampling theorem, $h < \lambda/2$, with λ wavelength, and the need to capture a satisfactory amount of geometrical details of the surface. The elements of the mesh serve as domain of the basis functions used for discretization of the current and of the RHS.

The steps toward construction of the linear system in 2.35 are the following: the unknown current $\boldsymbol{j}_s$ is approximated as a linear combination of N_s basis functions, called source basis functions, $\boldsymbol{s}_n$:

$$\boldsymbol{j}_s(\boldsymbol{r}) \simeq \sum_{n=1}^{N_s} \mathrm{j}_n \boldsymbol{s}_n(\boldsymbol{r}). \tag{2.36}$$

These basis functions are vectorial ($\boldsymbol{s}_n : \Gamma \to \mathbb{R}^3$), while the coefficients j_n are complex scalars, so that the linear combination in 2.36 can be a valid approximation of $\boldsymbol{j}_s$. Substituting eq. (2.36) in eq. (2.34), by linearity

$$\eta \sum_{n=1}^{N_s} \mathrm{j}_n \mathcal{T}_k \, \boldsymbol{s}_n \simeq \boldsymbol{b}. \tag{2.37}$$

The objective is to find the unknown coefficients j_n such as to minimize the error $\left(\boldsymbol{b} - \eta \sum_{n=1}^{N_s} \mathrm{j}_n \mathcal{T}_k \, \boldsymbol{s}_n\right)$, called residual. To this purpose, the residual is tested against a set of N_t basis functions, called test basis functions, $\boldsymbol{t}_m$, and the result of each of these operations is imposed to be null

$$\begin{aligned}
&\left\langle \boldsymbol{t}_m, \boldsymbol{b} - \eta \sum_{n=1}^{N_s} \mathrm{j}_n \mathcal{T}_k \, \boldsymbol{s}_n \right\rangle = 0 \\
\iff &\eta \sum_{n=1}^{N_s} \mathrm{j}_n \left\langle \boldsymbol{t}_m, \mathcal{T}_k \, \boldsymbol{s}_n \right\rangle = \left\langle \boldsymbol{t}_m, \boldsymbol{b} \right\rangle \\
\iff &\eta \sum_{n=1}^{N_s} \mathbf{T}_{mn} \, \mathrm{j}_n = \mathrm{b}_m \\
\iff &\eta \mathbf{T} \, \mathrm{j} = \mathrm{b}.
\end{aligned} \tag{2.38}$$

Finally, solution of integral equation in 2.34 can be found numerically by solving the linear system in 2.35, where the left hand side (LHS) matrix and the RHS are given by

$$\mathbf{T}_{mn} = \left\langle \boldsymbol{t}_m, \mathcal{T}_k \, \boldsymbol{s}_n \right\rangle \tag{2.39}$$

$$\mathrm{b}_m = \left\langle \boldsymbol{t}_m, \boldsymbol{b} \right\rangle . \tag{2.40}$$

2.2.1 Basis functions

Consider a closed surface Γ, characterized in each point by the outgoing unit normal $\hat{\boldsymbol{n}}$. It is discretized by a triangular mesh containing N_V vertices, N_E edges and N_F flat triangular faces. The genus of Γ is the number of handles, denoted as N_H. For such a geometry, Euler's formula

$$N_E = N_V + N_F + 2N_H - 2 \tag{2.41}$$

holds true. Local basis functions, such as Rao-Wilton-Glisson (RWG), Buffa-Christiansen (BC), loop or star basis functions shown in the following, have local support and are defined on the edges, or on the vertices, or on the faces of the mesh. By contrary, global loops are based on the handles of the geometry and span the entire mesh.

Rao-Wilton-Glisson basis functions

Rao-Wilton-Glisson, or Raviart-Thomas, basis functions are defined on the edges. Given notation in fig. 2.5, for any oriented edge e_i defined by the boundary vertices $\boldsymbol{v}_i^{\pm}$, the RWG definition is

$$\boldsymbol{f}_i(\boldsymbol{r}) = \begin{cases} \dfrac{\boldsymbol{r} - \boldsymbol{r}_i^+}{2A_i^+} & \boldsymbol{r} \in c_i^+ \\ \\ \dfrac{\boldsymbol{r}_i^- - \boldsymbol{r}}{2A_i^-} & \boldsymbol{r} \in c_i^- \end{cases} \tag{2.42}$$

where $A_i^{\pm}$ is the area of the triangle $c_i^{\pm}$. Normalization adopted in definition 2.42 is such that the flux integral through the defining edge equals one. It is to be noticed that another common normalization also includes multiplication by the length of the defining edge, l_i, as in the original paper in which this function has been introduced [13].

A significant property of the RWG basis functions is about continuity at the defining edge. It is easy to demonstrate that the component of $\boldsymbol{f}_i$ normal to the edge e_i is continuous across it; moreover it is constant along the edge at the value

$$|\boldsymbol{f}_i(\boldsymbol{r} \in e_i) \cdot \hat{\boldsymbol{n}}_i| = \frac{1}{l_i}, \tag{2.43}$$

where $\hat{\boldsymbol{n}}_i$ is the unit vector normal to the edge e_i. By contrary, the parallel component of $\boldsymbol{f}_i$ at the edge is discontinuous.

From continuity of the normal component, it derives the fact that the RWG basis function is div-conforming, i.e. its divergence is bounded (not containing Dirac deltas). In particular, its divergence is piece-wise constant patches and reads

$$\nabla \cdot \boldsymbol{f}_i(\boldsymbol{r}) = \begin{cases} \dfrac{1}{A_i^+} & \boldsymbol{r} \in c_i^+ \\ \\ -\dfrac{1}{A_i^-} & \boldsymbol{r} \in c_i^- \end{cases}. \tag{2.44}$$

Whereas, the discontinuity of the tangential component is translated in the property of curl-non-conformity: curl of an RWG basis function is not bounded. By performing a rotation of an RWG basis function through the $\hat{\boldsymbol{n}}\times$ operation, a curl-conforming, but not div-conforming, basis function is obtained.

Buffa-Christiansen basis functions

Buffa Christiansen basis functions, introduced in [14], are local functions defined on edges. They are defined on a barycentric refinement of the original mesh, obtained

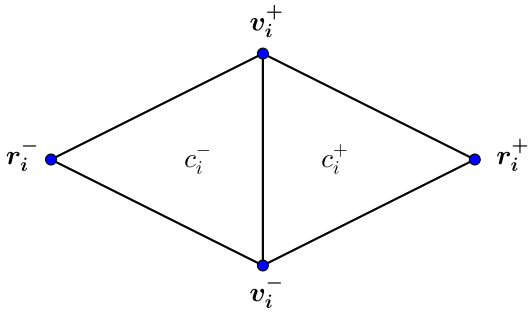

Figure 2.5: Notation used for the definition of RWG functions.

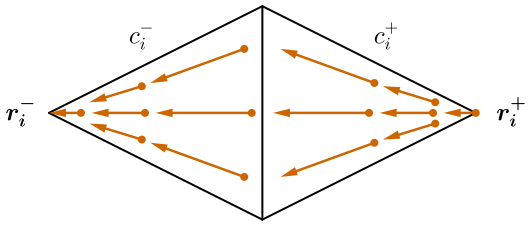

Figure 2.6: Rao-Wilton-Glisson basis function.

by subdividing each triangular face into six new faces, whose vertices lie at the original vertices or at the middle points of the original edges or at the vertex obtained from the intersection of the medians. The BC basis function defined on the edge e_i is built as linear combination of all the RWG basis functions defined on the edges with one (and only one) of the boundary vertices on e_i.

BC basis functions, denoted with the letter $\boldsymbol{g}$, are div-conforming by construction. Moreover, they are quasicurl-conforming, in the sense explained in [15]: the Gram matrix linking BC and rotated RWG functions is well conditioned. Rotated BC functions, $\hat{\boldsymbol{n}} \times \boldsymbol{g}$, are instead curl- and quasidiv-conforming.

Loop basis functions

The loop basis functions are local functions defined on vertices. The loop function on the vertex v_j can be expressed as

$$\boldsymbol{\Lambda}_j(\boldsymbol{r}) = \nabla \times \hat{\boldsymbol{n}}(\boldsymbol{r})\lambda_j(\boldsymbol{r}) = \hat{\boldsymbol{n}}(\boldsymbol{r}) \times \nabla\lambda_j(\boldsymbol{r}) \tag{2.45}$$

where λ_j is the scalar piece-wise linear Lagrange basis function, equal to one on v_j and null on all the other vertices, also called pyramid function [16].

A loop function can also be defined as linear combination of all the RWG functions defined on the edges containing v_j, as

$$\boldsymbol{\Lambda}_j(\boldsymbol{r}) = \sum_{i=1}^{N_e} \boldsymbol{\Lambda}_{ij} \boldsymbol{f}_i(\boldsymbol{r}), \tag{2.46}$$

where the coefficients $\boldsymbol{\Lambda}_{ij}$ are defined as

$$\boldsymbol{\Lambda}_{ij} = \begin{cases} +1 & v_j = v_i^- \\ -1 & v_j = v_i^+ \\ 0 & \text{otherwise} \end{cases} . \tag{2.47}$$

These coefficients can be collected to form the matrix $\mathbf{\Lambda} \in \mathbb{R}^{N_E \times N_V}$, which represents the loop to RWG transformation matrix: elements in column j are the coefficients of loop function $\mathbf{\Lambda}_j$ expressed as linear combination of the RWG functions.

The fundamental characteristic of the loop basis functions is the fact of being solenoidal, as can be simply derived from its definition 2.46 and eq. (2.44).

Star basis functions

The star basis functions are local functions defined on faces. The star function on the face c_j can be expressed as linear combination of the three RWG functions whose defining edges lie on the boundary of c_j:

$$\mathbf{\Sigma}_j(\boldsymbol{r}) = \sum_{i=1}^{N_e} \mathbf{\Sigma}_{ij} \boldsymbol{f}_i(\boldsymbol{r}), \tag{2.48}$$

where the coefficients $\mathbf{\Sigma}_{ij}$ are defined as

$$\mathbf{\Sigma}_{ij} = \begin{cases} +1 & c_j = c_i^+ \\ -1 & c_j = c_i^- \\ 0 & \text{otherwise} \end{cases}. \tag{2.49}$$

Matrix $\mathbf{\Sigma} \in \mathbb{R}^{N_E \times N_C}$ obtained in this way is the star to RWG transformation matrix. From $\mathbf{\Lambda}$ and $\mathbf{\Sigma}$ definitions, it follows that the columns of these matrices are orthogonal:

$$\mathbf{\Sigma}^T \mathbf{\Lambda} = \mathbf{0}. \tag{2.50}$$

It is interesting to notice that the function obtained by substituting the three RWG functions building the star with the corresponding BC functions is solenoidal [16]. It can be expressed as

$$\mathbb{\Sigma}_j(\boldsymbol{r}) = \nabla \times \hat{\boldsymbol{n}}(\boldsymbol{r}) \lambda_j^{bar}(\boldsymbol{r}) = \hat{\boldsymbol{n}}(\boldsymbol{r}) \times \nabla \lambda_j^{bar}(\boldsymbol{r}), \tag{2.51}$$

where λ_j^{bar} is a piece-wise linear, cell centered, function associated to the cell c_j.

Global loops

Global loops are global basis functions defined on handles. Each handle induces two global loops, called toroidal and poloidal, represented for a torus in figure 2.9. On the triangular discretization considered so far, global loops can be defined as linear combination of RWG functions:

$$\boldsymbol{H}_j(\boldsymbol{r}) = \sum_{i=1}^{N_e} \boldsymbol{H}_{ij} \boldsymbol{f}_i(\boldsymbol{r}) \tag{2.52}$$

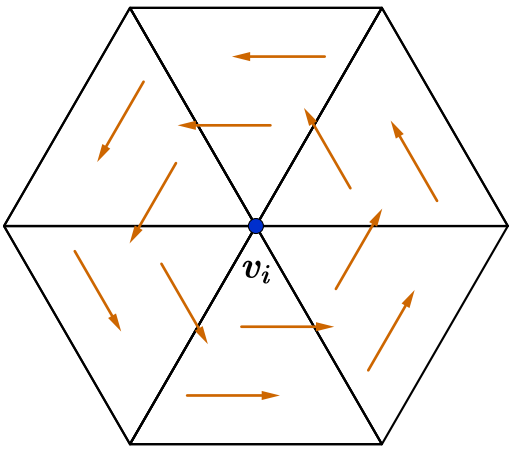

Figure 2.7: Loop basis function.

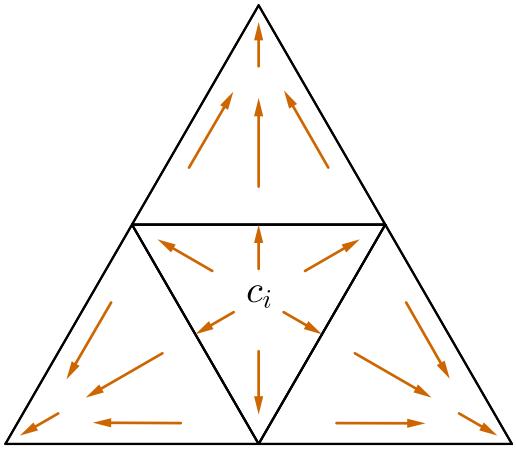

Figure 2.8: Star basis function.

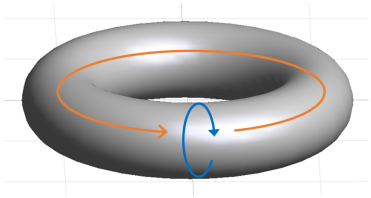

Figure 2.9: Global loops on a torus ($N_H = 1$): toroidal in orange, poloidal in blue.

where matrix $\boldsymbol{H} \in \mathbb{R}^{N_E \times 2N_H}$ is the global loop to RWG transformation matrix.

Computation of $\boldsymbol{H}$ matrix requires a computationally expensive algorithm based on graph theory. A lighter alternative is to evaluate the columns of $\boldsymbol{H}$ as the null-space of the outer and inner magnetic field integral operator, $\mathcal{K} \pm \frac{\mathcal{I}}{2}$. Theoretical reasons behind this operation are explained in [17].

The peculiarity of global loops defined as in 2.52 is that of being solenoidal functions. Consider now global loops defined on the surface Γ (not discretized). Such functions are harmonic: they satisfy the Laplace equation or, equivalently, they are at the same time both solenoidal and irrotational. Global loops defined in 2.52 as linear combination of RWG functions are just solenoidal instead, because curl operator cannot be represented with regularity in the RWG domain.

2.2.2 Discretization of operators and RHS

Testing procedure introduced in section 2.2 consists in an inner product computation. For $\boldsymbol{a}$, $\boldsymbol{b} : \Gamma \to \mathbb{C}^3$,

$$\langle \boldsymbol{a}, \boldsymbol{b} \rangle = \iint_\Gamma \overline{\boldsymbol{a}(\boldsymbol{r})} \cdot \boldsymbol{b}(\boldsymbol{r}) dS, \tag{2.53}$$

where the overline denotes complex conjugation.

A fundamental step in the discretization of an integral equation is the choice of source and test basis functions, derived from regularity considerations about the operator to be used.

Examine again the example of the EFIE for PEC: it is commonly discretized by means of RWG $\boldsymbol{f}$ as source and rotated RWG $\hat{\boldsymbol{n}} \times \boldsymbol{f}$ as test basis functions. By consequence, the RHS is tested against rotated RWG functions, to obtain

$$\mathbf{T}_{mn} = \langle \hat{\boldsymbol{n}} \times \boldsymbol{f}_m, \mathcal{T}_k \boldsymbol{f}_n \rangle \tag{2.54}$$

$$\mathrm{b}_m = \langle \hat{\boldsymbol{n}} \times \boldsymbol{f}_m, \boldsymbol{b} \rangle , \tag{2.55}$$

where then the $\hat{\boldsymbol{n}}\times$ in the testing is simplified with the one contained in definitions of $\boldsymbol{\mathcal{T}}_k$ and $\boldsymbol{b}$. Similarly, the (PEC)-EFIE can be discretized by means of BC $\boldsymbol{g}$ as source and rotated RWG $\hat{\boldsymbol{n}} \times \boldsymbol{g}$ as test basis functions, leading to

$$\mathbb{T}_{mn} = \langle \hat{\boldsymbol{n}} \times \boldsymbol{g}_m, \mathcal{T}_k \boldsymbol{g}_n \rangle \tag{2.56}$$

$$\mathbb{b}_m = \langle \hat{\boldsymbol{n}} \times \boldsymbol{g}_m, \boldsymbol{b} \rangle . \tag{2.57}$$

Also the identity operator can be discretized by means of some source and test basis functions. The outcome of this operation is called Gram-matrix, or specifically mix-Gram matrix in case source and test basis functions are of different types, and reads

$$\mathbf{G}_{mn} = \langle \boldsymbol{t}_m, \boldsymbol{s}_n \rangle . \tag{2.58}$$

Finally, it is worth mentioning a common trick exploited in discretization of $\mathcal{T}_{\phi,k}$ operator to get rid of the gradient present in its definition. Testing to be evaluated is

$$\begin{aligned} \mathbf{T}_{\phi,mn} &= \langle \hat{\boldsymbol{n}} \times \boldsymbol{f}_m, \mathcal{T}_{\phi,k} \boldsymbol{f}_n \rangle \\ &= \iint_{\Gamma_m} d\boldsymbol{r} (\hat{\boldsymbol{n}}(\boldsymbol{r}) \times \boldsymbol{f}_m(\boldsymbol{r})) \cdot \left(\hat{\boldsymbol{n}}(\boldsymbol{r}) \times \nabla \iint_{\Gamma_n} d\boldsymbol{r}' G_k(\boldsymbol{r}, \boldsymbol{r}') \nabla' \cdot \boldsymbol{f}(\boldsymbol{r}') \right) \end{aligned} \tag{2.59}$$

where Γ_m and Γ_n are the supports of the testing and source basis functions considered. After simplification of the $\hat{\boldsymbol{n}}\times$ operators and by defining the scalar quantity $\psi(\boldsymbol{r}) = \iint_{\Gamma_n} d\boldsymbol{r}' G_k(\boldsymbol{r}, \boldsymbol{r}') \nabla' \cdot \boldsymbol{f}(\boldsymbol{r}')$, the above testing reduces to

$$\mathbf{T}_{\phi,mn} = \iint_{\Gamma_m} d\boldsymbol{r} \boldsymbol{f}_m(\boldsymbol{r}) \cdot \nabla \psi(\boldsymbol{r}). \tag{2.60}$$

By applying the vector calculus identity $\nabla \cdot (\psi \boldsymbol{f}_m) = \psi \nabla \cdot \boldsymbol{f}_m + (\nabla \psi) \cdot \boldsymbol{f}_m$,

$$\mathbf{T}_{\psi,mn} = \iint_{\Gamma_m} d\boldsymbol{r} \nabla \cdot (\phi(\boldsymbol{r}) \boldsymbol{f}_m(\boldsymbol{r})) - \iint_{\Gamma_m} d\boldsymbol{r} \psi(\boldsymbol{r}) \nabla \cdot \boldsymbol{f}_m(\boldsymbol{r}). \tag{2.61}$$

By applying divergence theorem and by noticing that the normal component of an RWG function at the boundary of its domain is null, it follows that the first term in eq. (2.61) is null, since

$$\iint_{\Gamma_m} d\boldsymbol{r} \nabla \cdot (\psi(\boldsymbol{r}) \boldsymbol{f}_m(\boldsymbol{r})) = \oint_{\partial\Gamma_m} \psi(\boldsymbol{r}) \left(\boldsymbol{f}_m(\boldsymbol{r}) \cdot \hat{\boldsymbol{n}}(\boldsymbol{r})\right) \cdot d\boldsymbol{l} = 0. \tag{2.62}$$

Finally, the gradient in the definition of $\mathcal{T}_{\phi,k}$ has been removed and a divergence operation has appeared to the testing function, so that finally the expression of $\mathbf{T}_{\phi,mn}$ reads

$$\mathbf{T}_{\phi,mn} = - \iint_{\Gamma_m} d\boldsymbol{r} \nabla \cdot \boldsymbol{f}_m(\boldsymbol{r}) \iint_{\Gamma_n} d\boldsymbol{r}' G_k(\boldsymbol{r}, \boldsymbol{r}') \nabla' \cdot \boldsymbol{f}(\boldsymbol{r}'), \tag{2.63}$$

This discretization operation becomes completely similar to the one of the electric vector potential operator, apart from the fact that divergence is applied to both source and test basis functions.

2.2.3 Computational complexity

When solving numerically a problem, an important parameter to take into account is the computational complexity of the algorithm used, both in terms of time needed to reach a solution and space, such as the required memory. A numerical scheme is considered scalable if its complexity grows linearly or quasi-linearly with the number of unknowns. Unfortunately, this is not the case of the boundary integral equations presented so far, to be solved by means of the BEM, as it will be shown in the following.

Consider again the (PEC)-EFIE example in equation 2.34, to be solved numerically on a mesh with N_e edges. Solution of the problem is obtained in three steps:

1. evaluation of $\mathbf{T}$ matrix. If computed explicitly element by element, time complexity is $\mathcal{O}(N_e^2)$;

2. evaluation of b vector, in time complexity of $\mathcal{O}(N_e)$;

3. solution of the linear system in 2.35. If it is solved for the current vector explicitly as $\eta\,\mathrm{j} = \mathbf{T}^{-1}\mathrm{b}$, time complexity is the one of matrix inversion, $\mathcal{O}(N_e^3)$.

It follows an overall complexity of $\mathcal{O}(N_e^3)$, leading to an unaffordable solution time for increasing number of unknowns. Moreover, also the matrix storage complexity of $\mathcal{O}(N_e^2)$ constitutes an issue toward scalability.

This problem can be overcome by solving the linear system iteratively: the solution is sought inside the Krylov subspace, as span$\{\mathrm{b}, \mathbf{T}\mathrm{b}, \mathbf{T}^2\mathrm{b}, ..., \mathbf{T}^k\mathrm{b}\}$:

$$\eta\,\mathrm{j} = \mathbf{T}^{-1}\mathrm{b} \simeq \sum_{i=1}^{k} \alpha_i \mathbf{T}^i \mathrm{b}. \tag{2.64}$$

Time complexity in this case is given by the product of the number of iterations k necessary to reach the desired accuracy and the cost of matrix-vector multiplication, naively obtained in $\mathcal{O}(N_e^2)$ operations. The effort at this point should be twofold: from one side, the number of iterations should be kept constant; from the other, matrix computation's and matrix-vector product's cost should be reduced to linear. Time complexity required in case of success would then be $\mathcal{O}(k \cdot N_e) = \mathcal{O}(N_e)$.

The second between these tasks can be achieved by means of many techniques available in literature, such as the Adaptive Cross Approximation (ACA) [18, 19], the Fast Multiple Method (FMM) [20] and their multi-level versions [21–23]. They allow reduction of matrix evaluation and storage complexity as well as of matrix-vector product to quasi-linear.

As far as required number of iterations is concerned, the key parameter to take into account is the matrix condition number. For an invertible matrix $\mathbf{A}$, it is defined as

$$\mathrm{cond}(\mathbf{A}) = ||\mathbf{A}|| \cdot ||\mathbf{A}^{-1}||, \tag{2.65}$$

depending on the norm chosen. If Euclidean norm is considered, cond($\mathbf{A}$) is also equal to the ratio between the maximum and the minimum between the singular values of $\mathbf{A}$. The link between condition number and number of iterations can be perceived by noticing that , by virtue of spectral mapping theorem, the approximate equality in eq. (2.64) is translated in the approximate equality involving the eigenvalues of $\mathbf{T}$, λ_n,

$$\frac{1}{\lambda_n} \simeq \sum_{i=1}^{k} \alpha_i \lambda_n^i. \tag{2.66}$$

It is to be recalled then that eigenvalues and singular values of a matrix $\mathbf{A}$ are related quantities: for $\mathbf{A}$ symmetric positive definite (SPD), they are coincident; otherwise, singular values σ_n are defined as the square root of the eigenvalues of the SPD matrix $\mathbf{A}^H\mathbf{A}$, where the superscript ^{H} denotes complex conjugate. By looking at 2.66, it is clear that the lower the variation range of the singular values of $\mathbf{T}$ (the lower the condition number), the fewer terms in the summation 2.66 are required to approximate accurately the values $\frac{1}{\lambda_n}$. For example, in [24] an upper bound for the number of iterations is provided, involving the condition number, for the Conjugate Gradient (CG) method.

In conclusion, in order to keep the number of iterations k constant and low, it is necessary to assure condition number of matrix $\mathbf{T}$ constant and as low as possible. This is the target of matrix preconditioning, introduced in the following section.

2.3 Introduction to preconditioning

As already mentioned in the previous section, the condition number of a matrix is a crucial parameter when solving a linear system: it determines not only the number of iterations needed to reach a solution through an iterative solver, but also the achievable accuracy of the solution. Moreover, if the condition number is too high, the solver cannot reach convergence at all. A matrix is said well-conditioned if its condition number is low and independent of the problem's parameters, such as frequency, number of unknowns, material parameters; otherwise, it is called ill-conditioned.

Matrix preconditioning consists of finding left and/or right preconditioning matrices, $\mathbf{L}$ and $\mathbf{R}$, such that the condition number of the original matrix left and/or right multiplied by $\mathbf{L}$, $\mathbf{R}$ is lower than the one of the original matrix and fixed. Assuming to work with both left and right preconditioning matrices, the linear system $\mathbf{A}\mathrm{x} = \mathrm{b}$ becomes

$$\mathbf{LAR}\mathrm{y} = \mathbf{L}\mathrm{b} \tag{2.67}$$

with the original unknown vector $\mathrm{x} = \mathbf{R}\mathrm{y}$.

Before proceeding in the illustration of some preconditioning techniques exploited in the solution of EFIE and MFIE, it is necessary to give some more definitions. An operator is called compact if its spectrum clusters at zero. Then, given a compact integral operator $\mathcal{A}$, an integral equation in the form

$$\mathcal{A}\rho = f \tag{2.68}$$

is called Fredholm integral equation of first kind, whereas the equation

$$(\mathcal{I} + \mathcal{A})\rho = f \tag{2.69}$$

is a Fredholm integral equation of second kind [25]. Discretization of the operator in eq. (2.69) has the desirable property of a spectrum clustering at the value 1 (determined by the clustering of the identity operator), which is a favorable condition in the optics of convergence of a Krylov solver. Being $\mathcal{K}$ a compact operator, a typical example of second kind operator is $(\mathcal{I}/2 + \mathcal{K})$, whose eigenvalues accumulate at 1/2.

2.3.1 Calderón preconditioning

Calderón preconditioning is based on a couple of identities, which can be easily derived from the EFIE-MFIE system already introduced. Suppose to apply surface equivalence principle on a surface Γ in free space, i.e. interior and exterior medium are the same medium, characterized by impedance η. The exterior scattering problem is written as

$$\begin{pmatrix} \frac{\mathcal{I}}{2} - \mathcal{K} & \mathcal{T} \\ -\mathcal{T} & \frac{\mathcal{I}}{2} - \mathcal{K} \end{pmatrix} \begin{pmatrix} \boldsymbol{m}_s \\ \eta\, \boldsymbol{j}_s \end{pmatrix} = \begin{pmatrix} -\hat{\boldsymbol{n}} \times \boldsymbol{E}^{inc} \\ \eta\, \hat{\boldsymbol{n}} \times \boldsymbol{H}^{inc} \end{pmatrix}. \tag{2.70}$$

Interior scattering problem, obtained by applying the surface equivalence principle in absence of sources and looking for surface currents such that electric and magnetic fields outside are null, reads

$$\begin{pmatrix} \frac{\mathcal{I}}{2} + \mathcal{K} & -\mathcal{T} \\ \mathcal{T} & \frac{\mathcal{I}}{2} + \mathcal{K} \end{pmatrix} \begin{pmatrix} \boldsymbol{m}_s \\ \eta\, \boldsymbol{j}_s \end{pmatrix} = \begin{pmatrix} 0 \\ 0 \end{pmatrix}. \tag{2.71}$$

Operators in 2.70 and 2.71 are the Calderón projectors, respectively denoted by $\mathcal{P}_-$ and $\mathcal{P}_+$. More rigorous definitions and proofs can be found in [9] and [11]. From the property $\mathcal{P}_-\mathcal{P}_+ = 0$, the Calderón identities follow:

$$\mathcal{T}^2 = -\frac{\mathcal{I}}{4} + \mathcal{K}^2 \tag{2.72}$$

$$\mathcal{T}\mathcal{K} = -\mathcal{K}\mathcal{T}. \tag{2.73}$$

In particular, the first of them states that $\mathcal{T}^2$ is a second kind operator and can be exploited to precondition the EFIO discretization, as done in [15], in which the integral equation

$$\mathcal{T}_k^2\, \boldsymbol{j}_s = \mathcal{T}(-\hat{\boldsymbol{n}} \times \boldsymbol{E}^{inc}) \tag{2.74}$$

is solved instead than $\mathcal{T}_k\, \boldsymbol{j}_s = -\hat{\boldsymbol{n}} \times \boldsymbol{E}^{inc}$. The conforming discretization of eq. (2.74) reads

$$\mathbb{T}\mathbf{G}_{mix}^{-1}\mathbf{T}\mathrm{j} = \mathbb{T}\mathbf{G}_{mix}^{-1}\mathrm{b} \tag{2.75}$$

where $(\mathbf{G}_{mix})_{ij} = \langle \hat{\boldsymbol{n}} \times \boldsymbol{f}_i, \boldsymbol{g}_j \rangle$ is the well-conditioned Gram matrix linking the rotated RWG functional space to the BC one. Formulation in 2.75 is immune from both dense discretization and low-frequency breakdown, but is ill-posed, since a null-space in statics has been introduced in matrix $\mathbb{T}\mathbf{G}_{mix}^{-1}\mathbf{T}$. Application of a quasi-Helmholtz decomposition to cure the low-frequency current cancellations, together with the Calderón preconditioning to fix discretization breakdown, leads to a well-conditioned and low-frequency stable EFIE, presented in [26].

2.3.2 Quasi-Helmholtz preconditioning

Low-frequency breakdown

Quasi-Helmholtz preconditioning has been widely used to cure the so-called low-frequency breakdown of the $\mathcal{T}$ operator, i.e. the ill-posedness of the (PEC)-EFIE when decreasing frequency. Solution of this problem, addressed for the first time in [27], has gained crucial importance in the last years, with the growing impact of smaller and smaller electronic devices leading to a strong need of efficient and reliable low-frequency full-wave simulation tools.

Reasons behind the EFIO low-frequency breakdown can be easily understood from its definition in eq. (2.19): for $k \to 0$, the vector potential related term behaves as $\mathcal{O}(k)$, while the scalar potential one like $\mathcal{O}(1/k)$. So, for decreasing frequency, the first term vanishes (its related information is lost), while the other one grows unbounded: $\mathcal{T}_k \simeq 1/(jk)\mathcal{T}_{\phi,k}$, reflecting the decoupling between electric and magnetic fields toward statics. When trying to solve the linear system in eq. (2.35), rewritten as

$$\left[-\eta(jk)^2\,\mathbf{T}_A + \eta\mathbf{T}_\phi\right]\,\mathrm{j} = jk\mathrm{b}, \tag{2.76}$$

it can be noticed that any solenoidal current distribution approximates the solution: the problem is not well-posed.

From an analytical study of the asymptotic behaviour of the $\mathcal{T}$ operator spectrum, it is derived that the condition number of $\mathbf{T}$ scales as $\mathcal{O}(1/k^2)$: at sufficiently low frequency, the matrix is almost (numerically) singular and convergence of an iterative method applied to solve the linear system cannot be reached.

A possible strategy to solve this issue consists in separating the solenoidal and non-solenoidal current contributions and in rescaling the related blocks of the system separately, in order to avoid loss of information and reformulate the problem as well-posed.

Helmholtz decomposition theorem

Any sufficiently smooth and rapidly decaying vector field $\boldsymbol{U}$ can be represented as the sum of an irrotational and of a solenoidal field. Given the vector calculus identities valid for any sufficiently smooth scalar field ψ and vector field $\boldsymbol{V}$, $\nabla \times (\nabla\psi) = 0$ and $\nabla \cdot (\nabla \times \boldsymbol{V}) = 0$, the Helmholtz decomposition can be written as

$$\boldsymbol{U} = \nabla\psi + \nabla \times \boldsymbol{V}, \tag{2.77}$$

where the first term represents the irrotational component, while the second the solenoidal one. If $\boldsymbol{U}$ is defined on a two-dimensional surface Γ, this decomposition can be rewritten by means of surface operators as

$$\boldsymbol{U} = \nabla_s\psi + \hat{\boldsymbol{n}} \times \nabla_s\xi. \tag{2.78}$$

Rotation of 2.78 is still an Helmholtz decomposition:

$$\hat{\boldsymbol{n}} \times \boldsymbol{U} = \hat{\boldsymbol{n}} \times \nabla_s \psi - \nabla_s \xi \tag{2.79}$$

where the roles of solenoidal and irrotational components are exchanged.

If the vector field $\boldsymbol{U}$ is discretized, i.e. written as linear combination of basis functions, such as in eq. (2.36), a complete Helmholtz decomposition is not feasible; a quasi-Helmholtz decomposition can be performed instead. It consists of a separation of the field into a solenoidal, $\boldsymbol{U}^s$, and a non-solenoidal, $\boldsymbol{U}^{ns}$, component:

$$\boldsymbol{U} = \boldsymbol{U}^s + \boldsymbol{U}^{ns}. \tag{2.80}$$

Two different techniques to perform this decomposition and exploit it to fix the low-frequency breakdown are presented in the following.

Loop-Star decomposition

Loop, star and global loops, defined respectively on vertices, cells and handles, have already been presented in this chapter. It can be demonstrated that, for a closed surface Γ, they span the entire RWG space. From Euler equation 2.41, it can be deduced that the columns of $\boldsymbol{\Lambda}$ and $\boldsymbol{\Sigma}$ matrices are not linearly independent: one column from $\boldsymbol{\Lambda}$ and one from $\boldsymbol{\Sigma}$ should be removed to obtain linear independent bases. In the following, these cancellations will always be assumed, such that, from now on, $\boldsymbol{\Lambda} \in \mathbb{R}^{N_E \times (N_V - 1)}$, $\boldsymbol{\Sigma} \in \mathbb{R}^{N_E \times (N_C - 1)}$. The decomposition matrix $\boldsymbol{A}$ is defined as

$$\boldsymbol{A} = (\boldsymbol{\Lambda} \quad \boldsymbol{H} \quad \boldsymbol{\Sigma}). \tag{2.81}$$

Consider again the (PEC)-EFIE example, discretized as $\eta \mathbf{T}\,\mathrm{j} = \mathrm{b}$. By taking $\boldsymbol{A}^T$ and $\boldsymbol{A}$ as left and right preconditioning matrices, the linear system to be solved becomes

$$\begin{cases} \eta \boldsymbol{A}^T \mathbf{T} \boldsymbol{A}\,\mathrm{y} = \boldsymbol{A}^T \mathrm{b} \\ \mathrm{j} = \boldsymbol{A}\mathrm{y} \end{cases}. \tag{2.82}$$

The block multiplication $\boldsymbol{A}^T \mathbf{T} \boldsymbol{A}$ can be easily expanded in

$$\boldsymbol{A}^T \mathbf{T} \boldsymbol{A} = \begin{pmatrix} \boldsymbol{\Lambda}^T \mathbf{T} \boldsymbol{\Lambda} & \boldsymbol{\Lambda}^T \mathbf{T} \boldsymbol{H} & \boldsymbol{\Lambda}^T \mathbf{T} \boldsymbol{\Sigma} \\ \boldsymbol{H}^T \mathbf{T} \boldsymbol{\Lambda} & \boldsymbol{H}^T \mathbf{T} \boldsymbol{H} & \boldsymbol{H}^T \mathbf{T} \boldsymbol{\Sigma} \\ \boldsymbol{\Sigma}^T \mathbf{T} \boldsymbol{\Lambda} & \boldsymbol{\Sigma}^T \mathbf{T} \boldsymbol{H} & \boldsymbol{\Sigma}^T \mathbf{T} \boldsymbol{\Sigma} \end{pmatrix}, \tag{2.83}$$

where $\mathbf{T} = -jk\mathbf{T}_A + \frac{1}{jk}\mathbf{T}_\phi$. By recalling the definition of $\mathbf{T}_\phi$, given in eq. (2.63), and the fact that loop functions are solenoidal, it is clear that

$$\boldsymbol{\Lambda}^T \mathbf{T}_\phi = \mathbf{0} \tag{2.84}$$

$$\boldsymbol{H}^T \mathbf{T}_\phi = \mathbf{0} \tag{2.85}$$

$$\mathbf{T}_\phi \boldsymbol{\Lambda} = \mathbf{0} \tag{2.86}$$

$$\mathbf{T}_\phi \boldsymbol{H} = \mathbf{0}. \tag{2.87}$$

From these considerations, the product $\boldsymbol{A}^T\mathbf{T}\boldsymbol{A}$ can be rewritten as

$$\begin{aligned}\boldsymbol{A}^T\mathbf{T}\boldsymbol{A} &= \begin{pmatrix} \boldsymbol{\Lambda}^T(-jk\mathbf{T}_A)\boldsymbol{\Lambda} & \boldsymbol{\Lambda}^T(-jk\mathbf{T}_A)\boldsymbol{H} & \boldsymbol{\Lambda}^T(-jk\mathbf{T}_A)\boldsymbol{\Sigma} \\ \boldsymbol{H}^T(-jk\mathbf{T}_A)\boldsymbol{\Lambda} & \boldsymbol{H}^T(-jk\mathbf{T}_A)\boldsymbol{H} & \boldsymbol{H}^T(-jk\mathbf{T}_A)\boldsymbol{\Sigma} \\ \boldsymbol{\Sigma}^T(-jk\mathbf{T}_A)\boldsymbol{\Lambda} & \boldsymbol{\Sigma}^T(-jk\mathbf{T}_A)\boldsymbol{H} & \boldsymbol{\Sigma}^T(-jk\mathbf{T}_A + \frac{1}{jk}\mathbf{T}_\phi)\boldsymbol{\Sigma} \end{pmatrix} \\ &= \begin{pmatrix} \mathcal{O}(k) & \mathcal{O}(k) & \mathcal{O}(k) \\ \mathcal{O}(k) & \mathcal{O}(k) & \mathcal{O}(k) \\ \mathcal{O}(k) & \mathcal{O}(k) & \mathcal{O}(\frac{1}{k}) \end{pmatrix}. \end{aligned} \tag{2.88}$$

The conditioning behaviour of this matrix can be studied by means of the Gershgorin circle theorem.

Theorem 1 *(Gershgorin circle theorem). Given a matrix $\boldsymbol{M} \in \mathbb{C}^{N\times N}$, define, for any $i = 1, ..., N$, $R_i = \sum_{j\neq i} |(\boldsymbol{M})_{ij}|$ and $D_i(\boldsymbol{M}_{ii}, R_i)$ as the closed disk of center $\boldsymbol{M}_{ii}$ and radius R_i; these last are called Gershgorin disks. Then, all the eigenvalues of $\boldsymbol{M}$ are in the union of the Gershgorin disks.*

From Gershgorin theorem application, two eigenvalues clustering can be identified: one approaching zero as $\mathcal{O}(k)$, the other going at infinity as $\mathcal{O}(1/k)$, leading to a condition number scaling of $\mathcal{O}(1/k^2)$, as anticipated in section 2.3.2. This low-frequency breakdown can be cured by including some scalings in the decomposition matrix:

$$\boldsymbol{A}_s = \begin{pmatrix} \frac{1}{\sqrt{k}}\boldsymbol{\Lambda} & \frac{1}{\sqrt{k}}\boldsymbol{H} & \sqrt{k}\boldsymbol{\Sigma} \end{pmatrix}. \tag{2.89}$$

Indeed, the block scalings of the preconditioned matrix $\boldsymbol{A}_s^T\mathbf{T}\boldsymbol{A}_s$ becomes

$$\boldsymbol{A}_s^T\mathbf{T}\boldsymbol{A}_s = \begin{pmatrix} \mathcal{O}(1) & \mathcal{O}(1) & \mathcal{O}(k) \\ \mathcal{O}(1) & \mathcal{O}(1) & \mathcal{O}(k) \\ \mathcal{O}(k) & \mathcal{O}(k) & \mathcal{O}(1) \end{pmatrix}. \tag{2.90}$$

From Gershgorin theorem, the eigenvalues of this matrix cluster at constant values with vanishing radii: the problem is now well-conditioned, in the sense that the condition number of $\boldsymbol{A}_s^T\mathbf{T}\boldsymbol{A}_s$ is constant in frequency.

The major drawback of this kind of preconditioning is the fact that the loop-star decomposition introduces another kind of ill-conditioning, related to the mesh discretization. As analyzed in [16], the condition number of $\mathbf{G}^{\Lambda\Sigma} = [\boldsymbol{\Lambda} \quad \boldsymbol{\Sigma}]^T\,\mathbf{G}\,[\boldsymbol{\Lambda} \quad \boldsymbol{\Sigma}]$, with $\mathbf{G}$ being the well-conditioned Gram matrix of the RWG basis, grows as $\mathcal{O}(1/h^2)$, leading to a degradation of the condition number of the decomposed (PEC)-MFIE operator. This issue is related to the fact that the quasi-Helmholtz decomposition in this case is obtained by means of differential operators, whose spectrum is not flat. It can be fixed indeed by exploiting projectors, operators characterized by flat rectangular spectra, as shown in the following section.

Quasi-Helmholtz projection

Quasi-Helmholtz projectors are operators capable of projecting a vector into the solenoidal and the non-solenoidal subspaces, orthogonal between each other.

Consider first a vector field $\boldsymbol{x}$ discretized by means of RWG functions: we seek a mapping operator $\mathbf{P}^{\Sigma}$ such that $\mathbf{P}^{\Sigma}\boldsymbol{x} = \boldsymbol{x}^{ns}$, with $\boldsymbol{x}^{ns}$ lying in the non-solenoidal subspace, range of $\boldsymbol{\Sigma}$, denoted as $\mathcal{R}(\boldsymbol{\Sigma})$, and at minimum distance from $\boldsymbol{x}$. By virtue of projection theorem, the difference $(\boldsymbol{x} - \boldsymbol{x}^{ns})$ is orthogonal to $\mathcal{R}(\boldsymbol{\Sigma})$, i.e. it lies in the nullspace of $\boldsymbol{\Sigma}^T$, denoted as $\mathcal{N}(\boldsymbol{\Sigma}^T)$:

$$\begin{aligned} &\boldsymbol{\Sigma}^T(\boldsymbol{x} - \mathbf{P}^{\Sigma}\boldsymbol{x}) = 0 \\ \iff\ &\boldsymbol{\Sigma}^T\boldsymbol{x} = \boldsymbol{\Sigma}^T\mathbf{P}^{\Sigma}\boldsymbol{x}. \end{aligned} \tag{2.91}$$

Matrix $\mathbf{P}^{\Sigma} = \boldsymbol{\Sigma}\,(\boldsymbol{\Sigma}^T\,\boldsymbol{\Sigma})^{+}\boldsymbol{\Sigma}^T$, where $^+$ represents Moore-Penrose pseudo-inversion, satisfies equation 2.91. Moreover, it is a projector, i.e. $(\mathbf{P}^{\Sigma})^2 = \mathbf{P}^{\Sigma}$; more specifically, it is an orthogonal projector ($\mathcal{R}(\mathbf{P}^{\Sigma}) \perp \mathcal{N}(\mathbf{P}^{\Sigma})$) [28]. The projector to the solenoidal space, denoted as $\mathbf{P}^{\Lambda H}$, is simply defined as its complementary: it projects on the entire RWG solenoidal subspace, including both local and global loops. Finally, the quasi-Helmholtz projectors for the RWG functional space have expressions

$$\mathbf{P}^{\Sigma} = \boldsymbol{\Sigma}\,(\boldsymbol{\Sigma}^T\boldsymbol{\Sigma})^{+}\,\boldsymbol{\Sigma}^T \tag{2.92}$$

$$\mathbf{P}^{\Lambda H} = 1 - \mathbf{P}^{\Sigma}. \tag{2.93}$$

Similarly, the dual quasi-Helmholtz projectors can be defined, projecting respectively on the BC non solenoidal and solenoidal subspaces:

$$\mathbb{P}^{\Lambda} = \boldsymbol{\Lambda}\,(\boldsymbol{\Lambda}^T\boldsymbol{\Lambda})^{+}\,\boldsymbol{\Lambda}^T \tag{2.94}$$

$$\mathbb{P}^{\Sigma H} = 1 - \mathbb{P}^{\Lambda}. \tag{2.95}$$

Quasi-Helmholtz projectors can be exploited to separate the blocks of the operator corresponding to solenoidal or non-solenoidal source and testing functions employed and to rescale them independently. The electric field integral operator $\mathbf{T}$, left- and right- multiplied by the identity $\mathbf{I} = \mathbf{P}^{\Lambda H} + \mathbf{P}^{\Sigma}$, is written as

$$\begin{aligned} \mathbf{T} &= (\mathbf{P}^{\Lambda H} + \mathbf{P}^{\Sigma})\,\mathbf{T}\,(\mathbf{P}^{\Lambda H} + \mathbf{P}^{\Sigma}) \\ &= -jk\mathbf{P}^{\Lambda H}\mathbf{T}_A\mathbf{P}^{\Lambda H} - jk\mathbf{P}^{\Lambda H}\mathbf{T}_A\mathbf{P}^{\Sigma} - jk\mathbf{P}^{\Sigma}\mathbf{T}_A\mathbf{P}^{\Lambda H} \\ &+ \mathbf{P}^{\Sigma}\left(-jk\mathbf{T}_A + \frac{1}{jk}\mathbf{T}_{\phi}\right)\mathbf{P}^{\Sigma}, \end{aligned} \tag{2.96}$$

where the simplifications $\mathbf{P}^{\Lambda H}\mathbf{T}_{\phi} = \mathbf{T}_{\phi}\mathbf{P}^{\Lambda H} = \mathbf{0}$ have been enforced.

Preconditioning of the (PEC)-EFIE by means of quasi-Helmholtz projectors is obtained for example by means of left and right preconditioning matrices defined as

$$\mathbf{L} = \alpha \mathbf{P}^{\Lambda H} + \beta \mathbf{P}^{\Sigma} \tag{2.97}$$

$$\mathbf{R} = \gamma \mathbf{P}^{\Lambda H} + \delta \mathbf{P}^{\Sigma}, \tag{2.98}$$

where the multiplicative coefficients are chosen such as to obtain a well-conditioned matrix, as in the loop-star decomposition case. Finally, the system to be solved is written as

$$\begin{cases} \eta \boldsymbol{L}^T \mathbf{T} \boldsymbol{R} \mathrm{y} = \boldsymbol{L}^T \mathrm{b} \\ \mathrm{j} = \boldsymbol{R} \mathrm{y} \end{cases}. \tag{2.99}$$

This preconditioning strategy, differently from the previously presented loop-star decomposition, doesn't suffer from a mesh discretization ill-conditioning: condition number of $\boldsymbol{L}^T \mathbf{T} \boldsymbol{R}$ cannot be higher than cond($\mathbf{T}$). As already mentioned, it derives from the non-differential form of the projectors (overall differential contribution of $\mathbf{\Sigma}$ is cancelled in $\mathbf{P}^{\Sigma}$ expression, fig. 2.10). Another advantage resides in the fact that explicit detection of global loops is not required. Nevertheless, it is worth noticing that this benefit is also related to a loss of freedom in the rescaling coefficients' choice: global loop related blocks cannot be rescaled independently from the rest of the solenoidal functions.

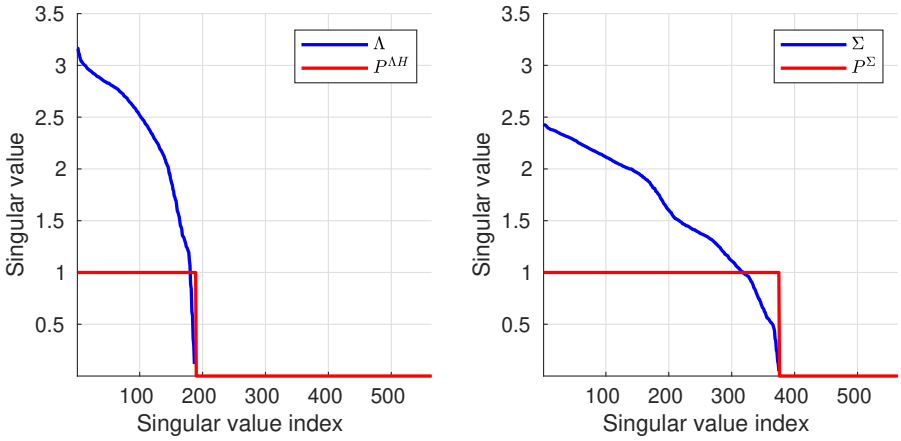

Figure 2.10: Singular values of $\mathbf{\Lambda}$ and $\mathbf{P}^{\Lambda H}$ (left) and of $\mathbf{\Sigma}$ and $\mathbf{P}^{\Sigma}$ (right) for a sphere discretized with 188 vertices, 376 cells and 564 edges.

Chapter 3

Low frequency stabilization of the PMCHWT formulation

This chapter will provide an overview on the low-frequency stabilization strategy of the PMCHWT integral equation, presented and detailed in [2]. The resulting formulation, based on quasi-Helmholtz decomposition and preconditioning, is stable and well-conditioned over a wide range of frequencies and conductivities, including the eddy current regime, which is the operating regime of numerous applications.

3.1 Eddy current regime

The first Maxwell's equation (1.1) in absence of magnetic current density states that a time varying flux integral of the magnetic field over a surface S induces a proportional circulation of the electric field along $C = \partial S$, that is a potential difference. By consequence, if C lies in a conductive medium, a conductive current flows along it. If a massive conductive object is considered, time-varying magnetic field induces voltages in it, leading to current loops difficult to predict by intuition; they are usually referred to as eddy currents [29]. Many well-known physical effects can be traced back to simple manifestations of the first Maxwell's equation: for example, magnetic flux variations induced by a time-varying current flowing in a conducting wire determine the so-called skin effect.

Many examples of applications exploiting eddy currents can be given, either based on the related ohmic losses in form of heating, called induction heating, or depending on the magnetic reaction field generated. Metallurgical treatment, non-destructive material testing techniques [30], induction motors are just few

of them. In other contexts, eddy current presence can be completely undesired. In printed circuit boards (PCBs) manufacturing for instance, unwanted loop currents contribute to a useless heating up of the board. Moreover, non-uniform current distributions in conducting lines due to both skin and proximity effects are detrimental for the metallic material itself, subject to electromigration. Whether eddy currents are beneficially exploited or undesired, their proper modelling is of great importance.

If displacement currents are negligible with respect to conduction currents, the problem is said to be in the eddy current regime, thus characterized by

$$\omega\epsilon_0 \ll \sigma. \tag{3.1}$$

Eddy current solvers look for electromagnetic field distributions satisfying the Maxwell's system in its magneto quasi-static approximation eq. (1.47), eq. (1.48) [1]. Validity of this approximation decreases when increasing the frequency, or equivalently when increasing the electrical size of the objects under test.

On the one hand, available commercial electromagnetic compatibility and interference circuit simulators are based, up to now, on the eddy current approximation in eq. (3.1). A couple of examples are the so-called JKHE and KHJ formulations, presented in [31]. Recalling that both integrated circuits' area and clock frequency increase at a rate of approximately 1.5 every 3 years predicted by the Moore's law [32], it is clear that eddy current solvers become less and less reliable with advancements of technological processes.

On the other hand, the PMCHWT integral equation presented in section 2.1.4, capable of modelling conductive objects, is a full-wave formulation, hence valid in any frequency condition. The severe low-frequency breakdown which affects it is one of the main reasons why it has not been exploited yet for exact electromagnetic compatibility and interference (EMC/EMI) circuit simulations.

3.2 Background and notation

Given the notation already presented in section 2.1.4, the PMCHWT formulation reads

$$\begin{pmatrix} \eta_0 \mathcal{T}_{k_0} + \eta_1 \mathcal{T}_{k_1} & -(\mathcal{K}_{k_0} + \mathcal{K}_{k_1}) \\ \mathcal{K}_{k_0} + \mathcal{K}_{k_1} & \frac{1}{\eta_0} \mathcal{T}_{k_0} + \frac{1}{\eta_1} \mathcal{T}_{k_1} \end{pmatrix} \begin{pmatrix} \boldsymbol{j}_s \\ \boldsymbol{m}_s \end{pmatrix} = \begin{pmatrix} -\hat{\boldsymbol{n}} \times \boldsymbol{E}^{inc} \\ -\hat{\boldsymbol{n}} \times \boldsymbol{H}^{inc} \end{pmatrix}. \tag{3.2}$$

Wavenumber inside the scatterer Ω_1 takes the complex value

$$k_1 = \omega\sqrt{(\epsilon_0\epsilon_r' - j\sigma/\omega)\mu_1} = \sqrt{\omega^2\epsilon_0\epsilon_r'\mu_1 - j\omega\sigma\mu_1} \tag{3.3}$$

which can be approximated in the eddy current regime as

$$k_1 \simeq \sqrt{-j\omega\sigma\mu_1} = \frac{1-j}{\delta} \tag{3.4}$$

with δ being the skin depth parameter, defined as $\delta = \sqrt{2/(\omega\sigma\mu_1)}$.

To obtain the BEM linear system, surface currents are discretized by means of div-conforming RWG source functions, while curl-conforming rotated RWG basis functions are used as test functions. Finally, the problem is reduced to

$$\begin{pmatrix} \mathbf{T}_{upper} & -\mathbf{K} \\ \mathbf{K} & \mathbf{T}_{lower} \end{pmatrix} \begin{pmatrix} \mathrm{j} \\ \mathrm{m} \end{pmatrix} = \begin{pmatrix} \mathrm{e} \\ \mathrm{h} \end{pmatrix} \tag{3.5}$$

where the matrix blocks are given by linear combinations of the matrices which discretize the interior and exterior EFIO and MFIO

$$\mathbf{K} = \mathbf{K}_{k_0} + \mathbf{K}_{k_1} \tag{3.6}$$
$$\mathbf{T}_{upper} = \mathbf{T}_{A,upper} + \mathbf{T}_{\phi,upper} \tag{3.7}$$
$$\mathbf{T}_{lower} = \mathbf{T}_{A,lower} + \mathbf{T}_{\phi,lower} \tag{3.8}$$
$$\mathbf{T}_{A,upper} == -jk_0\eta_0\mathbf{T}_{A,k_0} - jk_1\eta_1\mathbf{T}_{A,k_1} \tag{3.9}$$
$$\mathbf{T}_{\phi,upper} = \frac{\eta_0}{jk_0}\mathbf{T}_{\phi,k_0} + \frac{\eta_1}{jk_1}\mathbf{T}_{\phi,k_1} \tag{3.10}$$
$$\mathbf{T}_{A,lower} = -j\frac{k_0}{\eta_0}\mathbf{T}_{A,k_0} - j\frac{k_1}{\eta_1}\mathbf{T}_{A,k_1} \tag{3.11}$$
$$\mathbf{T}_{\phi,lower} = \frac{1}{jk_0\eta_0}\mathbf{T}_{\phi,k_0} + \frac{1}{jk_1\eta_1}\mathbf{T}_{\phi,k_1}. \tag{3.12}$$

Discretization of the continuous electric and magnetic operators are given by

$$(\mathbf{K}_k)_{mn} = \langle \hat{\boldsymbol{n}} \times \boldsymbol{f}_m, \mathcal{K}_k(\boldsymbol{f}_n) \rangle \tag{3.13}$$
$$(\mathbf{T}_{A,k})_{mn} = \langle \hat{\boldsymbol{n}} \times \boldsymbol{f}_m, \mathcal{T}_{A,k}(\boldsymbol{f}_n) \rangle \tag{3.14}$$
$$(\mathbf{T}_{\phi,k})_{mn} = \langle \hat{\boldsymbol{n}} \times \boldsymbol{f}_m, \mathcal{T}_{\phi,k}(\boldsymbol{f}_n) \rangle . \tag{3.15}$$

The unknown array contains the coefficients of the RWG expansions of the fictitious surface currents $\boldsymbol{j}_s$, $\boldsymbol{m}_s$; the RHS is given by the testing of the known term in eq. (3.2) against rotated RWG functions:

$$(\mathrm{e})_m = \left\langle \hat{\boldsymbol{n}} \times \boldsymbol{f}_m, -\hat{\boldsymbol{n}} \times \boldsymbol{E}^{inc} \right\rangle \tag{3.16}$$
$$(\mathrm{h})_m = \left\langle \hat{\boldsymbol{n}} \times \boldsymbol{f}_m, -\hat{\boldsymbol{n}} \times \boldsymbol{H}^{inc} \right\rangle . \tag{3.17}$$

3.3 Low frequency asymptotic analysis

In order to enlighten the reasons behind the PMCHWT low frequency breakdown and identify possible solutions for its regularization, it is necessary to perform a low frequency asymptotic analysis of all the operators involved in the PMCHWT

formulation, as well as of the possible excitations. This study is carried out in the eddy current regime, under the approximation $\omega\epsilon_0 \ll \sigma$, and makes use of the quasi-Helmholtz decomposition presented in section 2.3.2. In particular, application of the loop-star decomposition matrices to the system in eq. (3.5) results in the loop-star decomposed system

$$\mathbf{Z}_{\Lambda H \Sigma}\, \mathrm{y} = \mathrm{b}_{\Lambda H \Sigma}, \tag{3.18}$$

where the LHS matrix and RHS are given by

$$\mathbf{Z}_{\Lambda H \Sigma} = \begin{pmatrix} \mathbf{A}^T & \\ & \mathbf{A}^T \end{pmatrix} \begin{pmatrix} \mathbf{T}_{upper} & -\mathbf{K} \\ \mathbf{K} & \mathbf{T}_{lower} \end{pmatrix} \begin{pmatrix} \mathbf{A} & \\ & \mathbf{A} \end{pmatrix} \tag{3.19}$$

$$\mathrm{b}_{\Lambda H \Sigma} = \begin{pmatrix} \mathbf{A}^T & \\ & \mathbf{A}^T \end{pmatrix} \begin{pmatrix} \mathrm{e} \\ \mathrm{h} \end{pmatrix} \tag{3.20}$$

with $\mathbf{A}$ being the loop-star decomposition matrix previously defined as

$$\boldsymbol{A} = (\boldsymbol{\Lambda} \quad \boldsymbol{H} \quad \boldsymbol{\Sigma}) \tag{3.21}$$

The following sections will focus more on the method employed to perform the analysis, rather than on its intermediate results, which can be found instead in [2].

3.3.1 Magnetic field integral operator

The static part of the magnetic field integral operator cancels out when solenoidal functions (but not both harmonic) are used as testing and source functions [33]. Partial simplifications, which are not considered in this work, also arise in case of source and test harmonic functions, depending on the relative positions between source and test global loops [34]. The previous statement can be translated in matrix form as

$$\boldsymbol{\Lambda}^T \mathbf{K}_0 \boldsymbol{\Lambda} = \mathbf{0}, \quad \boldsymbol{H}^T \mathbf{K}_0 \boldsymbol{\Lambda} = \mathbf{0}, \quad \boldsymbol{\Lambda}^T \mathbf{K}_0 \boldsymbol{H} = \mathbf{0}, \tag{3.22}$$

where $\mathbf{K}_0$ represents the discretization of the static part of $\mathcal{K}$ operator,

$$(\mathcal{K}_0 \boldsymbol{f})(\boldsymbol{r}) = \hat{\boldsymbol{n}}(\boldsymbol{r}) \times \iint_\Gamma \nabla \frac{1}{4\pi|\boldsymbol{r} - \boldsymbol{r}'|} \times \boldsymbol{f}(\boldsymbol{r}') d\boldsymbol{r}'. \tag{3.23}$$

The asymptotic behaviour of $\mathbf{K}_{k_0}$, $\mathbf{K}_{k_1}$ and $\mathbf{K}_{k_0,d}$, $\mathbf{K}_{k_1,d}$, representing discretizations of the exterior and interior MFIOs, complete or without their static parts (subscript $_d$ stands for dynamic), can be retrieved by means of an analysis of their kernels. In particular, given the definition of $\mathbf{K}_k$,

$$(\mathbf{K}_k)_{mn} = \iint_\Gamma \boldsymbol{f}_m(\boldsymbol{r}) \iint_\Gamma \nabla G(\boldsymbol{r}, \boldsymbol{r}') \times \boldsymbol{f}_n(\boldsymbol{r}') d\boldsymbol{r}' d\boldsymbol{r}, \tag{3.24}$$

behaviours of $\Re((\mathbf{K}_k)_{mn})$ and $\Im((\mathbf{K}_k)_{mn})$ are the same as $\Re(\nabla G_k)$ and $\Im(\nabla G_k)$.

The Green's function's gradient can be written in terms of the Maclaurin expansion of G_k for $k \to 0$,

$$G_k(R) = \frac{1}{4\pi}\left[\frac{1}{R} - jk - \frac{k^2 R}{2} + \frac{jk^3 R^2}{6} + \mathcal{O}(k^4)\right] \tag{3.25}$$

$$\nabla G_k(R) = \frac{1}{4\pi}\left[\nabla\left(\frac{1}{R}\right) - \frac{k^2}{2}\nabla R + \frac{jk^3}{6}\nabla R^2 + \mathcal{O}(k^4)\right] \tag{3.26}$$

with $R = |\boldsymbol{r} - \boldsymbol{r}'|$. The first terms in 3.25 and 3.26 are frequency independent and clearly represent the static parts of G_k and ∇G_k. By recalling definitions of exterior and interior wavenumbers, leading to the scalings $k_0 = \mathcal{O}(\omega)$, $\Re(k_1) = \mathcal{O}(\sqrt{\omega})$,$\Im(k_1) = \mathcal{O}(\sqrt{\omega})$, it is finally possible to retrieve the asymptotic behaviours of $\mathbf{K} = \mathbf{K}_{k_0} + \mathbf{K}_{k_1}$ and $\mathbf{K}_d = \mathbf{K}_{k_0,d} + \mathbf{K}_{k_1,d}$ which read

$$||\Re(\mathbf{K})|| = \mathcal{O}(1), \quad ||\Im(\mathbf{K})|| = \mathcal{O}(\omega), \tag{3.27}$$

$$||\Re(\mathbf{K}_d)|| = \mathcal{O}(\omega^{3/2}), \quad ||\Im(\mathbf{K}_d)|| = \mathcal{O}(\omega). \tag{3.28}$$

3.3.2 Electric field integral operator

To study the low frequency behaviour of the diagonal blocks $\mathbf{T}_{upper}$ and $\mathbf{T}_{lower}$, an asymptotic analysis of the kernels of $\mathcal{T}_{A,k}$ and $\mathcal{T}_{\phi,k}$ operators should be performed. Given the definitions

$$(\mathbf{T}_{A,k})_{mn} = \iint_\Gamma \boldsymbol{f}_m(\boldsymbol{r}) \cdot \iint_\Gamma G(\boldsymbol{r},\boldsymbol{r}')\, \boldsymbol{f}_n(\boldsymbol{r}')d\boldsymbol{r}'d\boldsymbol{r} \tag{3.29}$$

$$(\mathbf{T}_{\phi,k})_{mn} = -\iint_\Gamma \nabla\cdot\boldsymbol{f}_m(\boldsymbol{r}) \iint_\Gamma G(\boldsymbol{r},\boldsymbol{r}')\, \nabla'\cdot\boldsymbol{f}_n(\boldsymbol{r}')d\boldsymbol{r}'d\boldsymbol{r}, \tag{3.30}$$

it follows that $(\mathbf{T}_{A,k})_{mn}$ and $(\mathbf{T}_{\phi,k})_{mn}$ in their real and imaginary parts show the same behaviours as the Green's function. It is necessary then to analyze the Maclaurin expansion of the Green's function in eq. (3.25).

As far as $\mathbf{T}_{A,k}$ is considered, a further care must be taken in case of use of solenoidal source basis function, of type local or global loop, generically denoted as $\boldsymbol{l}$, for which

$$\iint_\Gamma \boldsymbol{l}(\boldsymbol{r}')d\boldsymbol{r}' = 0. \tag{3.31}$$

Simplification 3.31 applies in particular to the second term in the Green's function expansion, spatially constant.

From these considerations, the following scalings are obtained:

$$||\Re(\mathbf{T}_{A,k_0})|| = \mathcal{O}(1), \quad ||\Im(\mathbf{T}_{A,k_0})|| = \begin{cases} \mathcal{O}(\omega^3) & \text{if } \boldsymbol{f}_n \text{ solenoidal} \\ \mathcal{O}(\omega) & \text{otherwise} \end{cases}, \tag{3.32}$$

$$||\Re(\mathbf{T}_{\phi,k_0})|| = \mathcal{O}(1), \quad ||\Im(\mathbf{T}_{\phi,k_0})|| = \mathcal{O}(\omega), \tag{3.33}$$

$$||\Re(\mathbf{T}_{A,k_1})|| = \mathcal{O}(1), \quad ||\Im(\mathbf{T}_{A,k_1})|| = \begin{cases} \mathcal{O}(\omega) & \text{if } \boldsymbol{f}_n \text{ solenoidal} \\ \mathcal{O}(\omega^{1/2}) & \text{otherwise} \end{cases}, \tag{3.34}$$

$$||\Re(\mathbf{T}_{\phi,k_1})|| = \mathcal{O}(1), \quad ||\Im(\mathbf{T}_{\phi,k_1})|| = \mathcal{O}(\omega^{1/2}). \tag{3.35}$$

Moreover, from definition 3.30, it follows immediately that $\mathbf{T}_{\phi,k}$ contribution vanishes every time a solenoidal function is used as source or test function, translated in formulae as

$$\boldsymbol{\Lambda}^T\mathbf{T}_{\phi,k} = \mathbf{0}, \quad \boldsymbol{H}^T\mathbf{T}_{\phi,k} = \mathbf{0}, \quad \mathbf{T}_{\phi,k}\boldsymbol{\Lambda} = \mathbf{0}, \quad \mathbf{T}_{\phi,k}\boldsymbol{H} = \mathbf{0}. \tag{3.36}$$

Putting together all the considerations seen so far, the following scalings are obtained:

$$||\Re(\mathbf{T}_{A,upper})|| = \begin{cases} \mathcal{O}(\omega^2) & \text{if } \boldsymbol{f}_n \text{ solenoidal} \\ \mathcal{O}(\omega^{3/2}) & \text{otherwise} \end{cases}, \quad ||\Im(\mathbf{T}_{A,upper})|| = \mathcal{O}(\omega), \tag{3.37}$$

$$||\Re(\mathbf{T}_{\phi,upper})|| = \mathcal{O}(1), \quad ||\Im(\mathbf{T}_{\phi,upper})|| = \mathcal{O}(\omega^{-1}), \tag{3.38}$$

$$||\Re(\mathbf{T}_{A,lower})|| = \mathcal{O}(1), \quad ||\Im(\mathbf{T}_{A,lower})|| = \begin{cases} \mathcal{O}(\omega) & \text{if } \boldsymbol{f}_n \text{ solenoidal} \\ \mathcal{O}(\omega^{1/2}) & \text{otherwise} \end{cases}, \tag{3.39}$$

$$||\Re(\mathbf{T}_{\phi,upper})|| = \mathcal{O}(\omega^{-1/2}), \quad ||\Im(\mathbf{T}_{\phi,upper})|| = \mathcal{O}(\omega^{-1}). \tag{3.40}$$

3.3.3 Quasi-Helmholtz decomposition of the reaction matrix

All the pieces of information collected in the previous sections can be summarized by writing the various scalings of the nine-by-nine block matrix $\mathbf{Z}_{\Lambda H\Sigma}$ in the following form:

$$\Re(\mathbf{Z}_{\Lambda H\Sigma}) = \mathcal{O}\left(\begin{array}{ccc|ccc} \omega^2 & \omega^2 & \omega^{3/2} & \omega^{3/2} & \omega^{3/2} & 1 \\ \omega^2 & \omega^2 & \omega^{3/2} & \omega^{3/2} & 1 & 1 \\ \omega^2 & \omega^2 & 1 & 1 & 1 & 1 \\ \hline \omega^{3/2} & \omega^{3/2} & 1 & 1 & 1 & 1 \\ \omega^{3/2} & 1 & 1 & 1 & 1 & 1 \\ 1 & 1 & 1 & 1 & 1 & \omega^{-1/2} \end{array}\right) \tag{3.41}$$

$$\Im(\mathbf{Z}_{\Lambda H\Sigma}) = \mathcal{O}\left(\begin{array}{ccc|ccc} \omega & \omega & \omega & \omega & \omega & \omega \\ \omega & \omega & \omega & \omega & \omega & \omega \\ \omega & \omega & \omega^{-1} & \omega & \omega & \omega \\ \hline \omega & \omega & \omega & \omega & \omega & \omega^{1/2} \\ \omega & \omega & \omega & \omega & \omega & \omega^{1/2} \\ \omega & \omega & \omega & \omega & \omega & \omega^{-1} \end{array}\right). \tag{3.42}$$

By definition of $\mathbf{Z}_{\Lambda H\Sigma}$, first and fourth rows correspond to local loop testing, first and fourth columns to local loop source functions and so on.

From the application of Gershgorin circle theorem on the quasi-Helmholtz decomposition of the PMCHWT interaction matrix just obtained, it is possible to understand the source of ill-conditioning. Indeed, three eigenvalues clusterings can be identified:

1. one set of eigenvalues going at zero as $\mathcal{O}(\omega)$, corresponding to the first and second rows;

2. one set diverging at infinity as $\mathcal{O}(\omega^{-1})$, corresponding to the third and sixth rows;

3. one set constant in frequency, corresponding to fourth and fifth rows.

These scalings, similar to the (PEC)-EFIE ones, lead to a diverging condition number, increasing as $\mathcal{O}(\omega^{-2})$ when moving toward lower frequencies. In conclusion, the reason behind the ill-conditioning is the inverse frequency scalings of the matrix diagonal blocks, corresponding to different scalings of the parts of the EFIO related to the vector and scalar potentials as well as their multiplicative coefficients. As already seen in the previous chapter it can be effectively cured by separating the solenoidal and non-solenoidal components of the system and by rescaling them independently.

3.3.4 Loss of solution accuracy

Evidently, a preconditioning strategy should be capable of handling and curing the low-frequency breakdown shown previously. However, another problem to be tackled at low frequency is the loss of digits of accuracy in the solution due to finite precision arithmetic. The technique presented in [2] to overcome this issue consists in the identification of the solution components needed to correctly retrieve the electromagnetic field in near of far field, depending on the application: accuracy in the evaluation of these components is to be guaranteed by the preconditioning strategy employed. Clearly, they depend on the excitation chosen; in [2], results

relative to a plane wave excitation, as well as to capacitive or inductive magnetic frill lumped excitations are reported.

More precisely, from the system $\mathbf{Z}_{\Lambda H\Sigma}\mathrm{y} = \mathrm{b}_{\Lambda H\Sigma}$, the analysis presented so far can be implemented in the following steps:

1. for a given type of excitation, evaluate the asymptotic scalings of the loop-star decomposed RHS $\mathrm{b}_{\Lambda H\Sigma}$;
2. derive the asymptotic scalings of the blocks of $\mathbf{Z}^{-1}_{\Lambda H\Sigma}$;
3. derive the asymptotic scalings of the intermediate solution y by multiplying $\mathrm{y} = \mathbf{Z}^{-1}_{\Lambda H\Sigma}\mathrm{b}_{\Lambda H\Sigma}$;
4. from the outcome of previous point, determine the scalings of the scattered near and far field: the solution components which produce the dominant components of the scattered fields are the ones that should be preserved.

3.4 Preconditioning strategy

Once the objectives to be pursued are clear, the preconditioning strategy can be designed. The rescaling coefficients of the different components of the system are grouped in the diagonal matrices

$$\mathbf{L} = \mathrm{diag}(a_L, b_L, c_L, d_L, e_L, f_L) \tag{3.43}$$

$$\mathbf{R} = \mathrm{diag}(a_R, b_R, c_R, d_R, e_R, f_R) \tag{3.44}$$

and the behaviours of the blocks of $\mathbf{L}\mathbf{Z}_{\Lambda H\Sigma}\mathbf{R}$ are studied for different choices of $\mathbf{L}$, $\mathbf{R}$. The resulting preconditioned matrix should gain a frequency independent conditioning behaviour. Moreover, the rescaling shouldn't introduce any nullspace and should be able to preserve accuracy of the previously identified solution's components which determine the dominant components of the scattered fields. The solution identified in [2] satisfies these requirements for all the considered types of excitations. The rescaling coefficients chosen are

$$\begin{pmatrix} a_L \\ b_L \\ c_L \\ d_L \\ e_L \\ f_L \end{pmatrix} = \begin{pmatrix} (\omega\mu_0)^{-1/2} \\ (\omega\mu_0)^{-1/2} \\ (\omega\epsilon_0)^{1/2} \\ (\omega\sigma)^{-1/2} \\ (\omega\mu_0)^{1/2} \\ (\omega\mu_0)^{1/2} \end{pmatrix}, \quad \begin{pmatrix} a_R \\ b_R \\ c_R \\ d_R \\ e_R \\ f_R \end{pmatrix} = \begin{pmatrix} (\omega\mu_0)^{-1/2} \\ (\omega\mu_0)^{-1/2} \\ (\omega\epsilon_0)^{1/2} \\ (\omega/\sigma)^{1/2} \\ (\omega/\sigma)^{1/2} \\ (\omega\mu_0)^{1/2} \end{pmatrix}. \tag{3.45}$$

It is also important to notice that the coefficients relative to the harmonic subspace are chosen to be equal to the adjacent loop or star ones; this has been

enforced to allow the use of quasi-Helmholtz projectors, defined in section 2.3.2. Finally, the preconditioned system reads

$$\begin{pmatrix} \boldsymbol{M}_1 & \mathbf{0} \\ \mathbf{0} & \mathbb{M}_2\boldsymbol{G}^{-1} \end{pmatrix} \boldsymbol{Z} \begin{pmatrix} \boldsymbol{M}_3 & \mathbf{0} \\ \mathbf{0} & \boldsymbol{M}_4 \end{pmatrix} \mathrm{y} = \begin{pmatrix} \boldsymbol{M}_1 & \mathbf{0} \\ \mathbf{0} & \mathbb{M}_2\boldsymbol{G}^{-1} \end{pmatrix} \mathrm{b} \tag{3.46}$$

where the preconditioning matrices are defined as

$$\boldsymbol{M}_1 = (\omega\mu_0)^{-1/2}\, \boldsymbol{P}^{\Lambda H} + (\omega\epsilon_0)^{1/2}\, \boldsymbol{P}^{\Sigma} \tag{3.47}$$

$$\mathbb{M}_2 = (\omega\sigma)^{-1/2}\, \mathbb{P}^{\Lambda} + (\omega\mu_0)^{1/2}\, \mathbb{P}^{\Sigma H} \tag{3.48}$$

$$\boldsymbol{M}_3 = (\omega\mu_0)^{-1/2}\, \boldsymbol{P}^{\Lambda H} + (\omega\epsilon_0)^{1/2}\, \boldsymbol{P}^{\Sigma} \tag{3.49}$$

$$\boldsymbol{M}_4 = (\omega/\sigma)^{1/2}\, \boldsymbol{P}^{\Lambda H} + (\omega\mu_0)^{1/2}\, \boldsymbol{P}^{\Sigma}. \tag{3.50}$$

The mix-Gram matrix in eq. (3.46) is defined as

$$(\boldsymbol{G})_{mn} = \langle \hat{\boldsymbol{n}} \times \boldsymbol{f}_m, \boldsymbol{g}_n \rangle \tag{3.51}$$

where $\boldsymbol{f}_m$ and $\boldsymbol{g}_n$ represents respectively RWG and BC functions, following the usual notation. Introduction of this matrix is required to link the rotated-RWG functional space, over which the operators are defined, to the BC space of the dual projectors. Its evaluation can lead to an important overhead if computed trivially; computational complexity can be significantly reduced by means of fast Gram matrix evaluation techniques recently developed inside the team.

The surface current solution is finally retrieved as

$$\begin{pmatrix} \mathrm{j} \\ \mathrm{m} \end{pmatrix} = \begin{pmatrix} \boldsymbol{M}_3 & \mathbf{0} \\ \mathbf{0} & \boldsymbol{M}_4 \end{pmatrix} \mathrm{y}. \tag{3.52}$$

3.5 Numerical results

In the following chapters, the validity and accuracy of the new formulation is demonstrated with a variety of experiments. In this section instead, reported numerical results focus on its conditioning behaviour.

In figure 3.1, a comparison between current densities in each cell of a copper sphere of radius 1 m, excited by a plane-wave oscillating at 1 mHz is shown. It is visible that preconditioning of the PMCHWT, by means of both loop-star decomposition and quasi-Helmholtz projectors, leads to results comparable with the ones provided by the two eddy-current solvers considered. Standard PMCHWT instead, highly ill-conditioned (with a condition number in the order of 10^{18}), does not provide a correct solution.

In figure 3.2, the condition number of the original PMCHWT formulation, as well as of its preconditioned versions, is shown as a function of frequency. It

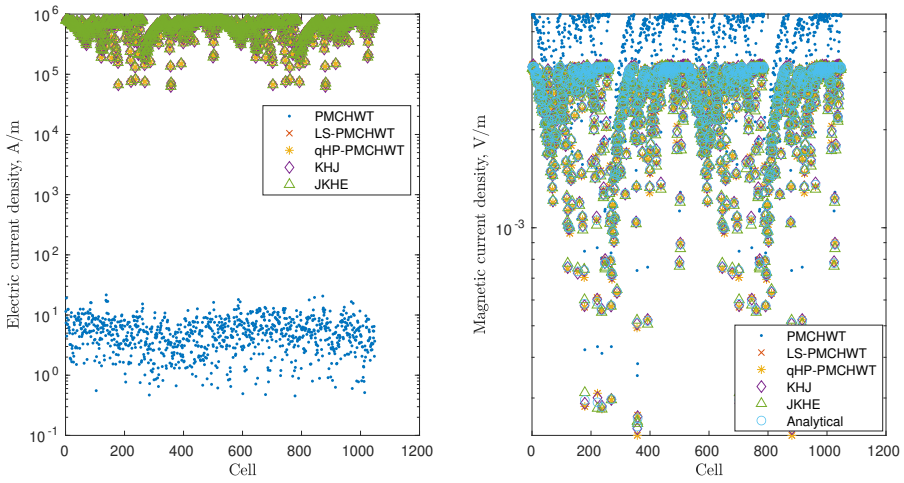

Figure 3.1: Sphere of radius 1 m discretized with 1048 elements, conductivity 5.8×10^7 S/m: electric and magnetic current density amplitude given an exciting plane wave of frequency 1 mHz along $-\hat{\boldsymbol{x}}$ with $B_0 = 1$ T.

is visible that the condition number of the PMCHWT formulation increases as $\mathcal{O}(\omega^2)$, as predicted theoretically. The preconditioned formulations instead are very well-conditioned in frequency.

In figure 3.3 instead, the conditioning behaviour is explored as function of discretization refinement. The conditioning behaviour of the formulation based on quasi-Helmholtz projectors is the same as the one of the original PMCHWT formulation: $\text{cond}(Z) = \mathcal{O}(h^{-2})$. This property of the PMCHWT operator, which can be seen as a compact perturbation of a matrix containing linear combinations of EFIOs on the diagonal blocks [35], follows directly from the conditioning of the $\mathcal{T}$ operator. The loop-star decomposition on the other hand introduces a further refinement ill-conditioning, so that the condition number scaling of the related formulation is $\mathcal{O}(h^{-4})$.

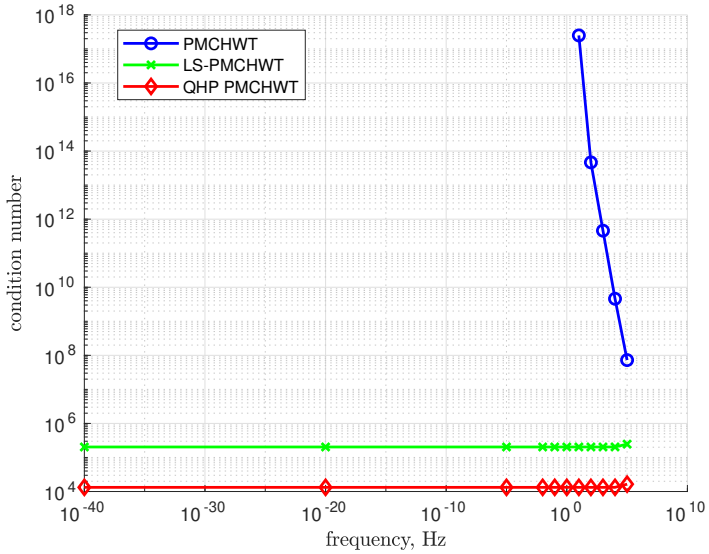

Figure 3.2: Sphere of radius 1 m discretized with 1048 elements, conductivity 1 S/m: condition number's behaviour in frequency.

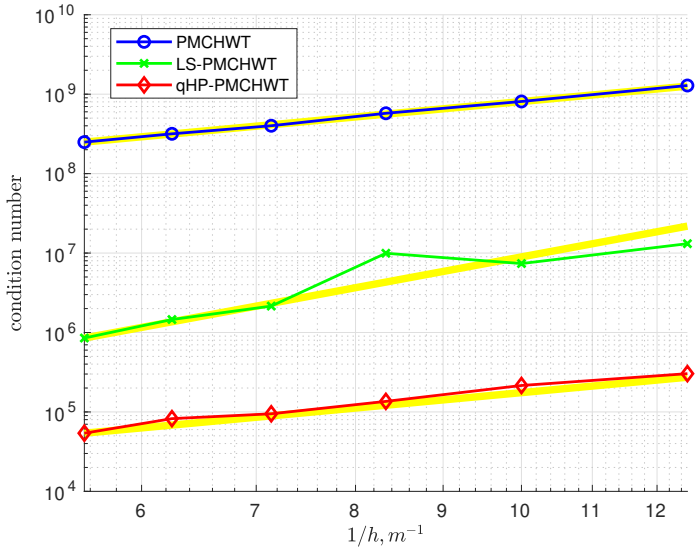

Figure 3.3: Sphere of radius 1 m, conductivity 1 S/m, excited by a plane wave at frequency 10 kHz: condition number's behaviour in discretization refinement.

Chapter 4

Radiation integrals

As seen in the previous chapters, solving an integral equation means looking for the tangential traces of the electric and magnetic fields at the boundaries of a scatterer. From this information then, by means of the equivalence principle, the electromagnetic field in the whole space can be reconstructed. Operators involved are the same already analyzed in the construction of the PMCHWT formulation, but the way in which they are discretized to reach a numerical solution is different.

4.1 Scattering inside and outside

Given the surface equivalent electric and magnetic currents retrieved by solving the PMCHWT system, $\boldsymbol{j}_s$ and $\boldsymbol{m}_s$, the electric and magnetic fields scattered outside or inside the object, denoted respectively by 0 and 1 superscript, are given by

$$\boldsymbol{E}^{0/1}(\boldsymbol{r}) = -j\omega\boldsymbol{A}^{0/1}(\boldsymbol{r}) + \frac{1}{j\omega\mu_{0/1}\epsilon_{0/1}}\nabla\nabla\cdot\boldsymbol{A}^{0/1}(\boldsymbol{r}) - \frac{1}{\epsilon_{0/1}}\nabla\times\boldsymbol{F}^{0/1}(\boldsymbol{r}) \tag{4.1}$$

$$\boldsymbol{H}^{0/1}(\boldsymbol{r}) = -j\omega\boldsymbol{F}^{0/1}(\boldsymbol{r}) + \frac{1}{j\omega\mu_{0/1}\epsilon_{0/1}}\nabla\nabla\cdot\boldsymbol{F}^{0/1}(\boldsymbol{r}) + \frac{1}{\mu_{0/1}}\nabla\times\boldsymbol{A}^{0/1}(\boldsymbol{r}) \tag{4.2}$$

where the potentials take the form

$$\boldsymbol{A}^{0}(\boldsymbol{r}) = \mu_0 \iint_{r'\in\Gamma} G_{k_0}(\boldsymbol{r}-\boldsymbol{r}')\boldsymbol{j}_s(\boldsymbol{r}')d\boldsymbol{r}' \tag{4.3}$$

$$\boldsymbol{F}^{0}(\boldsymbol{r}) = \epsilon_0 \iint_{r'\in\Gamma} G_{k_0}(\boldsymbol{r}-\boldsymbol{r}')\boldsymbol{m}_s(\boldsymbol{r}')d\boldsymbol{r}' \tag{4.4}$$

$$\boldsymbol{A}^{1}(\boldsymbol{r}) = \mu_1 \iint_{r'\in\Gamma} G_{k_1}(\boldsymbol{r}-\boldsymbol{r}')[-\boldsymbol{j}_s(\boldsymbol{r}')]d\boldsymbol{r}' \tag{4.5}$$

$$\boldsymbol{F}^{1}(\boldsymbol{r}) = \epsilon_1 \iint_{r'\in\Gamma} G_{k_1}(\boldsymbol{r}-\boldsymbol{r}')[-\boldsymbol{m}_s(\boldsymbol{r}')]d\boldsymbol{r}'. \tag{4.6}$$

Particular care should be taken in the implementation of these operators, both in the multiplicative coefficient and in the integrals evaluation, especially in the low-frequency scattering case.

Initially, the already implemented scattering code has been exploited to obtain some results. Its main limitation is the fact that complex values of permittivities are not taken into account, so that interior scattering cannot be evaluated directly. This can be easily fixed by adding externally a complex scaling of $\sqrt{\epsilon_r}$ to the first two terms, so that the coded operations are:

$$\begin{aligned}\boldsymbol{E}^1(\boldsymbol{r}) = -jk_1\frac{1}{\sqrt{\mu_1\epsilon_0}}\mu_1 \cdot \frac{1}{\sqrt{\epsilon_r}} \iint_{r'\in\Gamma} G_{k_1}(\boldsymbol{r}-\boldsymbol{r}')[-\boldsymbol{j}_s(\boldsymbol{r}')]d\boldsymbol{r}' \\ + \frac{1}{jk_1\frac{1}{\sqrt{\mu_1\epsilon_0}}\epsilon_0} \cdot \frac{1}{\sqrt{\epsilon_r}} \nabla\nabla \cdot \iint_{r'\in\Gamma} G_{k_1}(\boldsymbol{r}-\boldsymbol{r}')[-\boldsymbol{j}_s(\boldsymbol{r}')]d\boldsymbol{r}' \\ - \nabla \times \iint_{r'\in\Gamma} G_{k_1}(\boldsymbol{r}-\boldsymbol{r}')[-\boldsymbol{m}_s(\boldsymbol{r}')]d\boldsymbol{r}' \quad (4.7)\end{aligned}$$

$$\begin{aligned}\boldsymbol{H}^1(\boldsymbol{r}) = -jk_1\frac{1}{\sqrt{\mu_1\epsilon_0}}\epsilon_0 \cdot \sqrt{\epsilon_r} \iint_{r'\in\Gamma} G_{k_1}(\boldsymbol{r}-\boldsymbol{r}')[-\boldsymbol{m}_s(\boldsymbol{r}')]d\boldsymbol{r}' \\ + \frac{1}{jk_1\frac{1}{\sqrt{\mu_1\epsilon_0}}\mu_1} \cdot \sqrt{\epsilon_r}\, \nabla\nabla \cdot \iint_{r'\in\Gamma} G_{k_1}(\boldsymbol{r}-\boldsymbol{r}')[-\boldsymbol{m}_s(\boldsymbol{r}')]d\boldsymbol{r}' \\ + \nabla \times \iint_{r'\in\Gamma} G_{k_1}(\boldsymbol{r}-\boldsymbol{r}')[-\boldsymbol{j}_s(\boldsymbol{r}')]d\boldsymbol{r}'. \quad (4.8)\end{aligned}$$

However, this kind of formulation is not suitable to the low frequency regime, because of numerical cancellations arising both in multiplicative coefficients and in integral evaluations.

A better alternative is to implement directly 4.1 and 4.2, enforcing, where needed, the simplifications with the multiplicative coefficients in the potentials. As far as integral evaluation is concerned, a couple of useful manipulations are

$$\nabla\nabla \cdot \boldsymbol{A}(\boldsymbol{r}) = \mu \iint_{r'\in\Gamma} \nabla G_k(\boldsymbol{r}-\boldsymbol{r}')\nabla' \cdot \boldsymbol{j}_s(\boldsymbol{r}')d\boldsymbol{r} \quad (4.9)$$

$$\nabla \times \boldsymbol{A}(\boldsymbol{r}) = \mu \iint_{r'\in\Gamma} \nabla G(\boldsymbol{r}-\boldsymbol{r}') \times \boldsymbol{j}_s(\boldsymbol{r}')dS', \quad (4.10)$$

which can also be moved to the magnetic vector potential case. Moreover, other simplifications related to the solenoidal components of the currents, $\mathrm{j}^{\Lambda H}$ and $\mathrm{m}^{\Lambda H}$, and to the Green's function evaluation should be carefully enforced to move at extremely low frequency. They are listed in the following.

1. The solenoidal components of the currents do not contribute to the second terms in equations 4.1 and 4.2.

2. By expanding in power series the Green's function, a constant term (with respect to the space variable) arises. The result of integrating the product of a constant times a solenoidal function is zero (3.31): this has to be enforced.

3. When evaluating the gradient of the Green's function, the gradient of the constant term of its power series expansion (constant with respect to the space variable) should be enforced to be null.

Finally, the scattered fields are evaluated as

$$\begin{aligned}\boldsymbol{E}^{0/1}(\boldsymbol{r}) = &-j\omega\mu_{0/1}\iint_{r'\in\Gamma} G_{k_{0/1}}(\boldsymbol{r}-\boldsymbol{r}')[\pm\boldsymbol{j}_s^{\Sigma}(\boldsymbol{r}')]d\boldsymbol{r}' \\ &- j\omega\mu_{0/1}\iint_{r'\in\Gamma} G^{\Lambda H}_{k_{0/1}}(\boldsymbol{r}-\boldsymbol{r}')[\pm\boldsymbol{j}_s^{\Lambda H}(\boldsymbol{r}')]d\boldsymbol{r}' \\ &+ \frac{1}{j\omega\epsilon_{0/1}}\iint_{r'\in\Gamma} \nabla G_{k_{0/1}}(\boldsymbol{r}-\boldsymbol{r}')\nabla'\cdot[\pm\boldsymbol{j}_s^{\Sigma}(\boldsymbol{r}')]d\boldsymbol{r}' \\ &- \iint_{r'\in\Gamma} \nabla G_{k_{0/1}}(\boldsymbol{r}-\boldsymbol{r}')\times[\pm\boldsymbol{m}_s(\boldsymbol{r}')]d\boldsymbol{r}' \quad (4.11)\end{aligned}$$

$$\begin{aligned}\boldsymbol{H}^{0/1}(\boldsymbol{r}) = &-j\omega\epsilon_{0/1}\iint_{r'\in\Gamma} G_{k_{0/1}}(\boldsymbol{r}-\boldsymbol{r}')[\pm\boldsymbol{m}_s^{\Sigma}(\boldsymbol{r}')]d\boldsymbol{r}' \\ &- j\omega\epsilon_{0/1}\iint_{r'\in\Gamma} G^{\Lambda H}_{k_{0/1}}(\boldsymbol{r}-\boldsymbol{r}')[\pm\boldsymbol{m}_s^{\Lambda H}(\boldsymbol{r}')]d\boldsymbol{r}' \\ &+ \frac{1}{j\omega\mu_{0/1}}\iint_{r'\in\Gamma} \nabla G_{k_{0/1}}(\boldsymbol{r}-\boldsymbol{r}')\nabla'\cdot[\pm\boldsymbol{m}_s^{\Sigma}(\boldsymbol{r}')]d\boldsymbol{r}' \\ &+ \iint_{r'\in\Gamma} \nabla G_{k_{0/1}}(\boldsymbol{r}-\boldsymbol{r}')\times[\pm\boldsymbol{j}_s(\boldsymbol{r}')]d\boldsymbol{r}', \quad (4.12)\end{aligned}$$

where the coefficients of the solenoidal and non-solenoidal current components in RWG basis are $(\mathrm{j/m})^{\Lambda H} = \mathbf{P}^{\Lambda H}(\mathrm{j/m})$ and $(\mathrm{j/m})^{\Sigma} = \mathbf{P}^{\Sigma}(\mathrm{j/m})$; the Green's function denoted by the superscript ΛH is a modification of G such that, for $R = |\boldsymbol{r}-\boldsymbol{r}'| \to 0$, the constant term of its Taylor expansion is cancelled:

$$G(R)_k^{\Lambda H} = \frac{1}{4\pi}\left[\frac{1}{R} - k^2 R + \mathcal{O}(R^2)\right]. \quad (4.13)$$

A final consideration to be pointed out is about the evaluation of the integrals in eq. (4.11), eq. (4.12) in case the point of evaluation $\boldsymbol{r}$ approaches surface Γ in $\boldsymbol{r}'$. In such conditions, the kernels become singular, so that singularity extraction techniques are needed to numerically evaluate the integrals. In particular, a singularity subtraction approach is implemented, briefly presented in section 6.2.1.

Its performances are good when used to evaluate near field radiation integrals; when increasing the distance between scatterer and evaluation points instead, singularity extraction is not needed any more. Moreover, singularity subtraction based integration results unstable for increasing values of distances R, so that its exploitation in far field evaluation leads to dramatic error. So, it is necessary to implement a control on the distance between scatterer and evaluation points to decide whether to enforce singularity extraction or not in radiation integrals' evaluation.

4.2 Numerical results

4.2.1 Scattering from a sphere in far-field

In this section, the far-field scattering from a sphere excited by an incident plane-wave is considered. The analytic solution of this problem can be found in the framework of the Mie theory: incident and scattered fields are expanded in terms of vector spherical waves and enforcement of boundary conditions at Γ allows to retrieve the unknown coefficients of the series representing the scattered field [36]. This can be used as benchmark to estimate the accuracy of fields evaluated from eq. (4.11) and eq. (4.12).

They can also be compared with the far field approximations, given by

$$\boldsymbol{E}^0_{FF}(\boldsymbol{r}) = -j\omega(\boldsymbol{A}_{FF}(\boldsymbol{r}) - (\boldsymbol{A}_{FF}(\boldsymbol{r})\cdot\hat{\boldsymbol{r}})\,\hat{\boldsymbol{r}}) + j\omega\eta_0\,\hat{\boldsymbol{r}}\times\boldsymbol{F}_{FF}(\boldsymbol{r}) \tag{4.14}$$

$$\boldsymbol{H}^0_{FF}(\boldsymbol{r}) = -j\omega(\boldsymbol{F}_{FF}(\boldsymbol{r}) - (\boldsymbol{F}_{FF}(\boldsymbol{r})\cdot\hat{\boldsymbol{r}})\,\hat{\boldsymbol{r}}) - \frac{j\omega}{\eta_0}\,\hat{\boldsymbol{r}}\times\boldsymbol{A}_{FF}(\boldsymbol{r}) \tag{4.15}$$

where the vector potentials take the form

$$\boldsymbol{A}_{FF}(\boldsymbol{r}) = \mu_0\frac{e^{-jk|\boldsymbol{r}|}}{4\pi|\boldsymbol{r}|}\iint_{\boldsymbol{r}'\in\Gamma} e^{jk\hat{\boldsymbol{r}}\cdot\boldsymbol{r}'}\,j_s(\boldsymbol{r}')\,dS \tag{4.16}$$

$$\boldsymbol{F}_{FF}(\boldsymbol{r}) = \epsilon_0\frac{e^{-jk|\boldsymbol{r}|}}{4\pi|\boldsymbol{r}|}\iint_{\boldsymbol{r}'\in\Gamma} e^{jk\hat{\boldsymbol{r}}\cdot\boldsymbol{r}'}\,m_s(\boldsymbol{r}')\,dS. \tag{4.17}$$

These simplifications of radiation formulae derive from some considerations, valid in the far-field region, i.e. at observation points $\boldsymbol{r}$ far enough from the object, $R \gg D$, with D characteristic size of the scatterer:

1. assuming the origin of the reference system at the scatterer, R can be approximated as $R = |\boldsymbol{r} - \boldsymbol{r}'| \simeq |\boldsymbol{r}| - \hat{\boldsymbol{r}}\cdot\boldsymbol{r}'$;

2. for $R \to \infty$, the second terms in equations 4.11 and 4.12 is negligible with respect to the others;

3. $\boldsymbol{E}^0_{FF}$, $\boldsymbol{H}^0_{FF}$ behave locally as plane waves: their radial components are vanishing and need to be cancelled.

When examining far fields, it is customary to deal with radar cross sections. Given a scatterer excited by an impinging field $\boldsymbol{E}^{inc}$, the radar cross section is defined as «the area intercepting that amount of power which, when scattered isotropically, produces at the receiver a density which is equal to that scattered by the actual target» [37]. It can be evaluated as

$$RCS(\theta, \phi) = 4\pi|\boldsymbol{r}|^2 \frac{|\boldsymbol{E}^0_{FF}(\boldsymbol{r})|^2}{|\boldsymbol{E}^{inc}(\boldsymbol{r})|^2} \tag{4.18}$$

independently from the distance.

Numerical results shown in the following represent, for a given ϕ angle, RCS(θ) of a sphere of radius 1 m, conductivity 1 S/m, excited by an impinging plane wave propagating in the $-\hat{\boldsymbol{z}}$ direction with amplitude 1 V/m. The green curves represent analytical solutions, while the blue and red ones display numerical results obtained from equations 4.14, 4.15 (far field approximation) and 4.11, 4.12. In figure 4.2, it is visible that relative errors of numerical results (compared against the analytical ones) decrease with mesh refinement as $\mathcal{O}(1/h^2)$. Finally, from a comparison between figures 4.3a and 4.3b, the importance of avoiding singularity extraction in far field becomes evident. In fig. 4.3b, just the onset of instabilities related to singularity subtraction are visible; oscillations become much more important when further increasing the evaluation distance, providing completely wrong results.

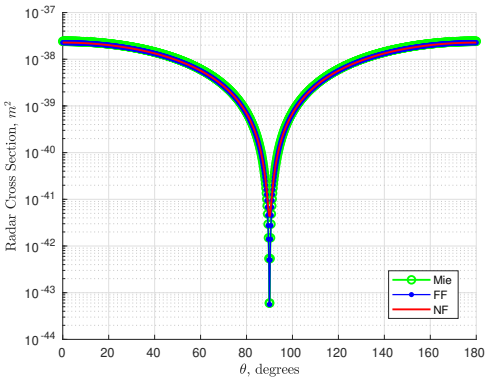

Figure 4.1: Radar Cross Section at $\phi = 0\,°$, distance 1×10^{12} m, given an exciting plane wave of frequency 0.01 Hz along $-\hat{\boldsymbol{z}}$.

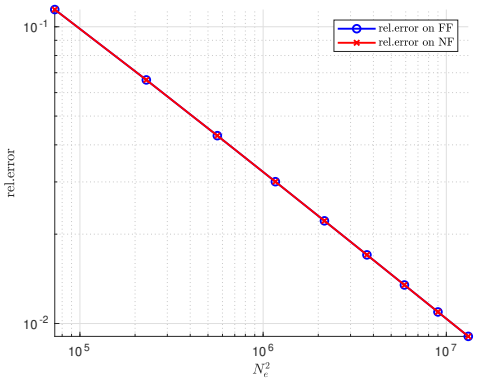

Figure 4.2: Relative error (in norm) on the Radar Cross Section at $\phi = 0\,°$, distance 1×10^{12} m, given an exciting plane wave of frequency 100 Hz along $-\hat{\boldsymbol{z}}$.

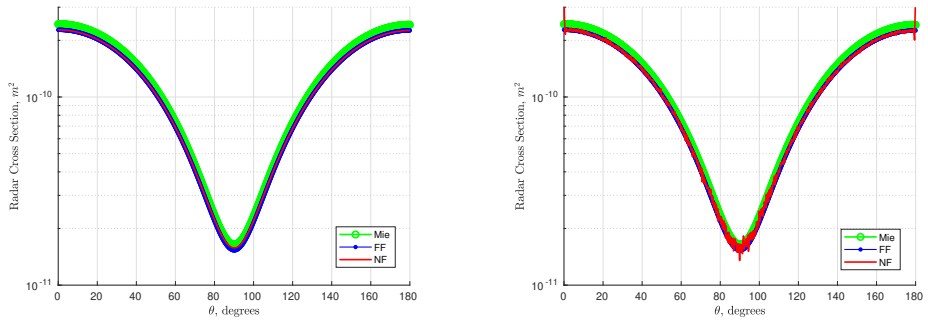

(a) Integration without singularity extraction **(b)** Enforcement of singularity extraction

Figure 4.3: Radar Cross Section at $\phi = -15\,°$, distance 20 km, given an exciting plane wave of frequency 100 kHz along $-\hat{\boldsymbol{z}}$: NF labeled curve obtained (a) without singularity extraction and (b) with singularity extraction.

4.2.2 Scattering from a sphere in near-field

The Mie theory provides analytical solution also to the near field scattering problem considered in the previous section, providing a valid benchmark for error estimation of numerical results. In the following, near scattering from a sphere of radius 1 m, conductivity 1 S/m, excited by an incident plane wave along $-\hat{\boldsymbol{z}}$, with amplitude 1 V/m is considered. By recalling the way in which the PMCHWT formulation has been assembled, i.e. as superposition of an exterior scattering problem with excitation from outside and an interior, source-less, one, it is clear that the total fields inside and outside are given by

$$[\boldsymbol{E}/\boldsymbol{H}(\boldsymbol{r})]_{outside} = \boldsymbol{E}^0/\boldsymbol{H}^0(\boldsymbol{r}) + \boldsymbol{E}^{inc}/\boldsymbol{H}^{inc}(\boldsymbol{r}) \tag{4.19}$$

$$[\boldsymbol{E}/\boldsymbol{H}(\boldsymbol{r})]_{inside} = \boldsymbol{E}^1/\boldsymbol{H}^1(\boldsymbol{r}). \tag{4.20}$$

Total field is simulated in a specific direction, given by $[\theta, \phi]$: the error behaviour is then estimated along ρ (a reference system with the origin in the center of the sphere is considered, $[\theta, \phi, \rho]$ denote spherical coordinates: polar angle, azimuthal angle and radial distance). Simulations shown are at the frequency of 100 kHz, required for stability of the formulation based on combination of vector spherical harmonics which provides the analytical solution.

In figure 4.4, the relative error on the electric and magnetic fields is represented for different mesh refinements (in legend, the number of basis functions, equal to N_e, is reported). A good converging behaviour is visible, for both inside and outside fields. This test is also useful to evaluate the minimum distance from the boundary Γ at which the radiators still provide correct results. The fact that

the analytical solution is correct at indefinitely small distance from Γ (lower than machine precision) can be deduced from the fact that boundary conditions are always satisfied, both in tangential and in normal form. Therefore, provided this reliable benchmark, it is possible to estimate the maximum ρ in the interior of the object, or equivalently the minimum distance $d_{min} = \text{radius} - \rho_{max}$, at which the error is still acceptable, for example lower than 10%. It is obtained that this minimum distance d_{min} decreases from 1.4 cm to 2 mm when increasing the number of edges of the discretization from 1,227 to 3,594 ·

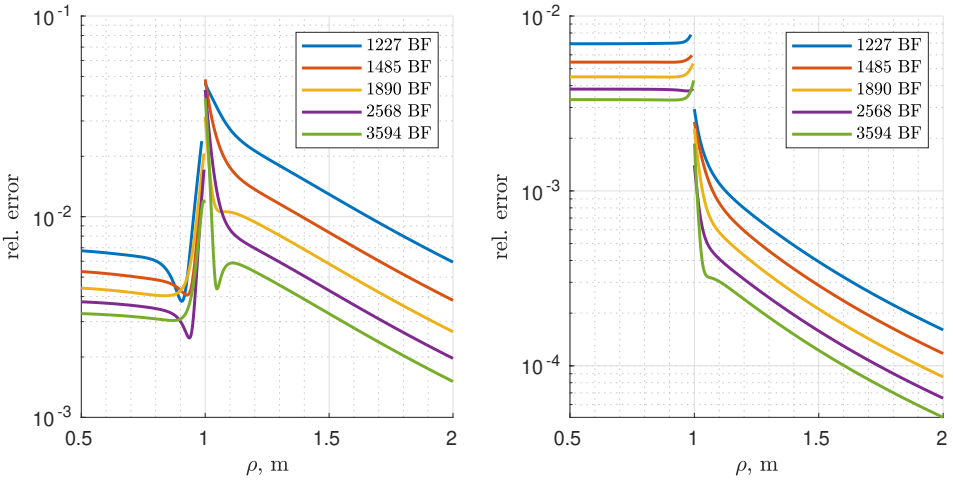

Figure 4.4: Relative error on the electric field (left) and the magnetic field (right) between numerical and analytical solutions. Measured scattering is in direction $[\theta, \phi] = \left[\frac{3\pi}{4}, \frac{\pi}{6}\right]$.

4.2.3 Self-consistency test

Finally, a self consistency test can be considered to further check validity of the implemented scattering operators. It is based on comparison between a known field distribution and the numerical scattering from some currents directly derived from the known distribution, correct by definition. More specifically, the test setup comprehends an electric dipole scattering in free-space, such that field distribution is known everywhere from theory [38]. Then, it is possible to assume a surface Γ, such that the electric dipole lies in its interior. Introduction of this fictitious surface doesn't establish any material discontinuity: both interior and exterior media are free space. By use of surface equivalence principle, the surface currents are defined

on Γ

$$\boldsymbol{m}_s(\boldsymbol{r}) = -\hat{\boldsymbol{n}}(\boldsymbol{r}) \times \boldsymbol{E}_d(\boldsymbol{r}), \quad \boldsymbol{r} \in \Gamma \tag{4.21}$$

$$\boldsymbol{j}_s(\boldsymbol{r}) = \hat{\boldsymbol{n}}(\boldsymbol{r}) \times \boldsymbol{H}_d(\boldsymbol{r}), \quad \boldsymbol{r} \in \Gamma \tag{4.22}$$

such that their radiation $\boldsymbol{E}^{sc}$, $\boldsymbol{H}^{sc}$ is opposite to the electromagnetic field radiated from the dipole, $\boldsymbol{E}_d$, $\boldsymbol{H}_d$, in the outside, source-free, region Ω_0, while $\boldsymbol{E}^{sc}$, $\boldsymbol{H}^{sc}$ vanishes in the inside region Ω_1:

$$\boldsymbol{E}^{sc} = -\boldsymbol{E}_d, \ \boldsymbol{H}^{sc} = -\boldsymbol{H}_d, \quad \boldsymbol{r} \in \Omega_0 \tag{4.23}$$

$$\boldsymbol{E}^{sc} = 0, \ \boldsymbol{H}^{sc} = 0, \quad \boldsymbol{r} \in \Omega_1. \tag{4.24}$$

In figures 4.5 and 4.6, relative error on the outside field, $|\boldsymbol{E}^{sc} + \boldsymbol{E}_d|/|\boldsymbol{E}_d|$, is shown, as well as the norm of the scattered field inside, $|\boldsymbol{E}^{sc}|$. Both quantities decrease with mesh refinement and are constant in a wide frequency range. In particular, results in figure 4.5 have been obtained for a spherical surface Γ_1 with radius 1 m centered in the origin; in figure 4.6 instead, a toroidal surface Γ_2 is considered (with major radius of 1 m, minor radius of 0.2 m), allowing validation of the radiators implemented also in presence of multiply connected geometries.

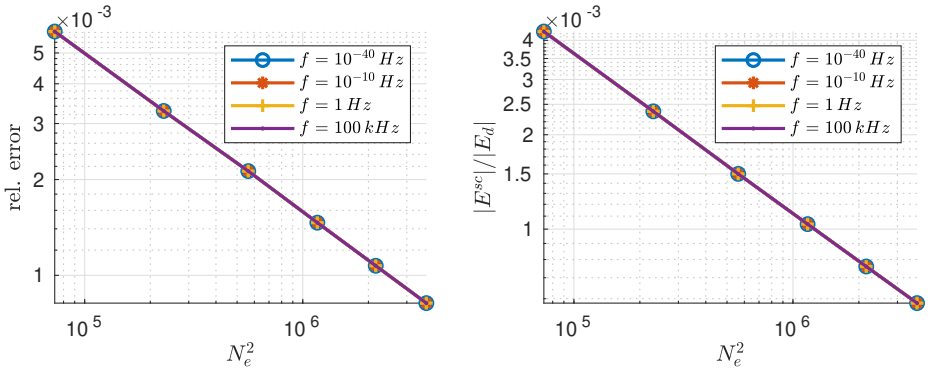

Figure 4.5: Electric dipole radiating from inside the spherical surface Γ_1: relative error on the exterior scattered electric field (left) and norm of the interior scattered electric field (right).

Similarly, the complementary test can be performed: the fictitious surface Γ is assumed such that the radiating dipole lies in its exterior, Ω_0. In this case, surface equivalence principle can be applied by defining $\boldsymbol{m}_s$, $\boldsymbol{j}_s$ such that the fields scattered from them are opposite to the ones radiated from the dipole in the interior (source-free) region Ω_1, while they vanish on the exterior region:

$$\boldsymbol{E}^{sc} = -\boldsymbol{E}_d, \ \boldsymbol{H}^{sc} = -\boldsymbol{H}_d, \quad \boldsymbol{r} \in \Omega_1 \tag{4.25}$$

$$\boldsymbol{E}^{sc} = 0, \ \boldsymbol{H}^{sc} = 0, \quad \boldsymbol{r} \in \Omega_0. \tag{4.26}$$

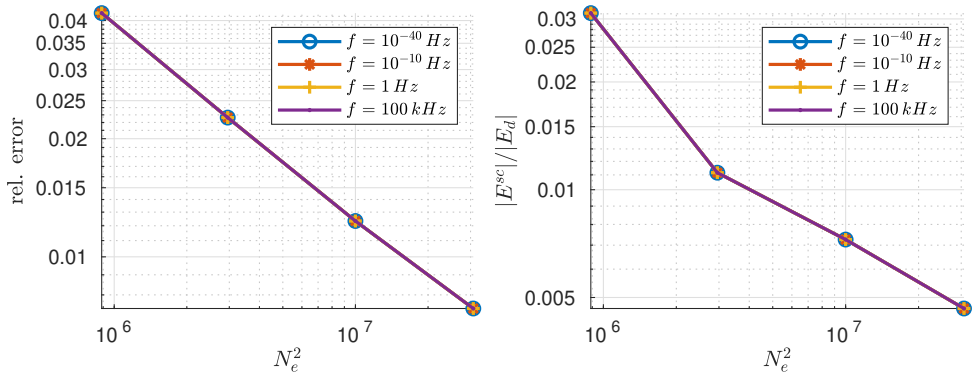

Figure 4.6: Electric dipole radiating from inside the toroidal surface Γ_2: relative error on the exterior scattered electric field (left) and norm of the interior scattered electric field (right).

Similar results as in the previous case are obtained, shown in figures 4.7 for the spherical Γ_1, fig. 4.8 for the toroidal Γ_2.

By considering the field radiated by a magnetic dipole instead, the magnetic field correctness can be assured. Analogue results as the ones already reported have been obtained; for sake of brevity, just the ones relative to a magnetic dipole radiating from inside a sphere are shown in figure 4.9.

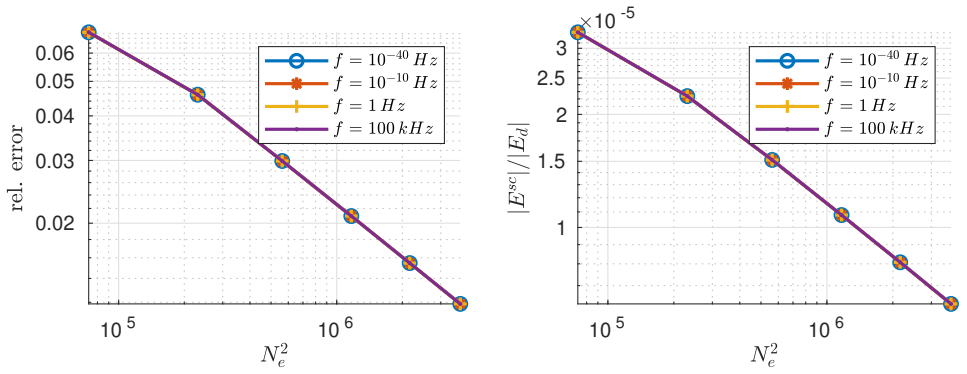

Figure 4.7: Electric dipole radiating from outside the spherical surface Γ_1: relative error on the interior scattered electric field (left) and norm of the exterior scattered electric field (right).

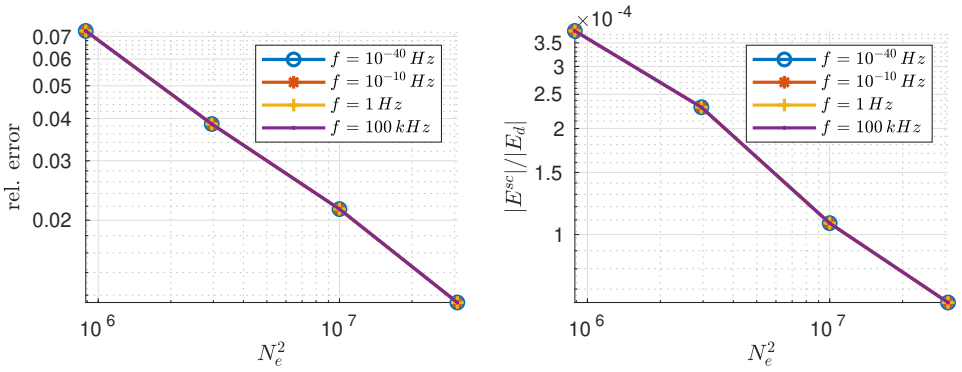

Figure 4.8: Electric dipole radiating from outside the toroidal surface Γ_2: relative error on the interior scattered electric field (left) and norm of the exterior scattered electric field (right).

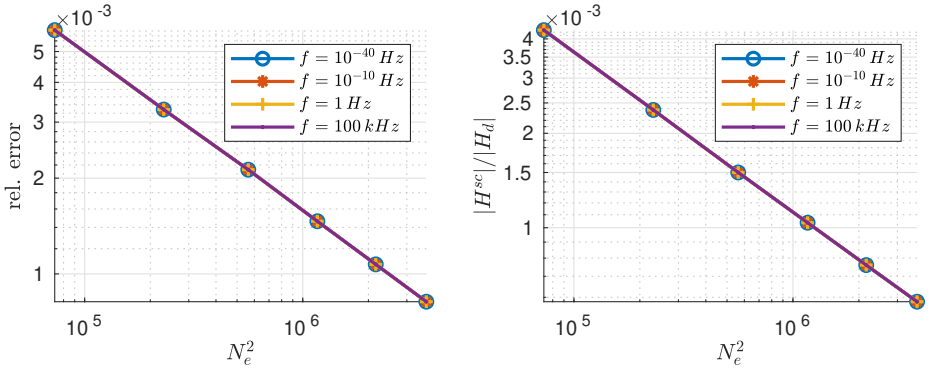

Figure 4.9: Magnetic dipole radiating from inside the spherical surface Γ_1: relative error on the exterior scattered magnetic field (left) and norm of the interior scattered magnetic field (right).

Implementation notes

Some implementation notes related to the test presented in this section are still to be given. In particular, from what said so far, it is not clear how to retrieve the coefficients of the expansions

$$\boldsymbol{m}_s(\boldsymbol{r}) \simeq \sum_{n=1}^{N_e} \mathrm{m}_n \boldsymbol{f}_n(\boldsymbol{r}) \tag{4.27}$$

$$\boldsymbol{j}_s(\boldsymbol{r}) \simeq \sum_{n=1}^{N_e} \mathrm{j}_n \boldsymbol{f}_n(\boldsymbol{r}) \tag{4.28}$$

where $\boldsymbol{f}_n$ are RWG functions. These coefficients are indeed the input to the radiations, while $\boldsymbol{m}_s$ and $\boldsymbol{j}_s$ are in this case known vector fields, continuous on Γ. Given $\boldsymbol{m}_s$, $\boldsymbol{j}_s$, and an RWG functional space defined on a mesh, two different strategies can be exploited to find the coefficients m_n, j_n. The first one is the so called interpolatory method: the coefficients are just given by the sampling of the vector fields $\boldsymbol{m}_s$, $\boldsymbol{j}_s$ on some points of the mesh (for example, on the central point of the defining edges of $\boldsymbol{f}_n$). This technique allows to minimize the interpolatory error in the sampling points.

To minimize instead the error norm on the whole surface, the projecting method is more suited: it consists in testing the residual $\boldsymbol{m}_s(\boldsymbol{r}) - \sum_{n=1}^{N_e} \mathrm{m}_n \boldsymbol{f}_n(\boldsymbol{r})$ against the set of N_e RWG basis functions and imposing the result of each of these operations to be null, similarly to what done in section 2.2 to build the MoM linear system:

$$\begin{aligned} & \left\langle \boldsymbol{f}_m, \boldsymbol{m}_s - \sum_{n=1}^{N_e} \mathrm{m}_n \boldsymbol{f}_n \right\rangle = 0 \\ \iff & \sum_{n=1}^{Ne} \mathrm{m}_n \left\langle \boldsymbol{f}_m, \boldsymbol{f}_n \right\rangle = \left\langle \boldsymbol{f}_m, \boldsymbol{m}_s \right\rangle \\ \iff & \mathbf{G}\mathrm{m} = \mathrm{b} \end{aligned} \tag{4.29}$$

where $\mathbf{G}$ is the RWG-to-RWG Gram matrix, m is the array containing the coefficients m_n, and b is the array whose elements are obtained from the testing of the vector field $\boldsymbol{m}_s$ against the basis functions.

Chapter 5

Validation on circuital structures

A good way to test the solver is to apply it to some simple circuital structures in the low-frequency regime and to verify that the behaviour of the simulated electric and magnetic fields is consistent with that predicted by circuit theory. Increasing the ratio between wavelength and characteristic size of the object under test, the structure under consideration can be approximated as a lumped circuit, so that simulation's outcome and analytic results derived from quasi-static approximations should converge.

5.1 Source modelling

The most natural way to induce an excitation on a circuital structure is to impose a potential difference at its ends, for example by means of a battery. This can be modelled by what is known in literature as a voltage gap. Two kinds of voltage gaps can be enforced: of finite or infinitesimal width. These are presented in the following, as well as some practical indications on their implementation on a discretized surface domain.

Moreover, it is possible to distinguish between inductive and capacitive excitation depending on whether a global loop of the structure is excited or not.

5.1.1 Finite width voltage gap

To enforce a voltage difference, a feed region should be identified, also called gap. It is the spatial region at which the excitation is imposed. In the case of a cylindrical wire, the feed region would be a small portion of the wire. Assuming not too sharp curvature radius of the wire, the gap can be approximated as a cylinder with height

d much smaller than the wire length. Moreover, it is also necessary to assume $d \ll \lambda$, such that quasi-static approximations and, consequently, Kirchhoff laws hold true. Under these conditions, it is necessary to enforce an exciting electric field inside the feed region, which can be approximated as [39]

$$\boldsymbol{E}^{inc}(\boldsymbol{r}) = \hat{\boldsymbol{z}} \frac{V_0}{d} \Pi_g(\boldsymbol{r}), \tag{5.1}$$

where $\hat{\boldsymbol{z}}$ is the unit vector parallel to the cylinder height extension, V_0 is the potential difference to impose, $\Pi_g(\boldsymbol{r})$ is a three-dimensional port function equal to 1 for points $\boldsymbol{r}$ belonging to the gap and to 0 otherwise.

Given the reduced dimensions of the gap region, which leads to the fulfilment of quasi-static approximations, it is possible to assume that the excitation imposed inside the gap does not radiate outside it. From this consideration, once the PMCHWT equation has been solved under the voltage gap excitation conditions, the electric and magnetic fields inside and outside the object can be retrieved from the scattering of the surface currents $\boldsymbol{j}_s$, $\boldsymbol{m}_s$, solution of the problem, only.

To build the PMCHWT formulation introduced in section 2.1.4, it is necessary to evaluate the RHS vector

$$\mathrm{e}_m = \left\langle \hat{\boldsymbol{n}} \times \boldsymbol{f}_m, -\hat{\boldsymbol{n}} \times \boldsymbol{E}^{inc} \right\rangle = \left\langle \boldsymbol{f}_m, -\boldsymbol{E}^{inc} \right\rangle. \tag{5.2}$$

It means that, for any RWG function $\boldsymbol{f}_m$ with support partially or completely lying inside the gap, the integral

$$\mathrm{e}_m = -\frac{V_0}{d} \iint_{\boldsymbol{r}' \in \Gamma} \boldsymbol{f}_m(\boldsymbol{r}') \cdot \hat{\boldsymbol{z}}\, \Pi_g(\boldsymbol{r}')\, d\boldsymbol{r}' \tag{5.3}$$

has to be evaluated. At this point, it is worth noticing that the supports of the RWG functions on the boundary of the cylindrical gap assumed so far are triangles lying on planes parallel to $\hat{\boldsymbol{z}}$, so that the dot product $\boldsymbol{f}_m(\boldsymbol{r}') \cdot \hat{\boldsymbol{z}}$ can be expressed as linear combinations of normal and parallel (to the defining edge) RWG's components only. Coefficients of the linear combination are respectively $\sin(\theta)$ and $\cos(\theta)$, where θ is defined as the angle between $\hat{\boldsymbol{z}}$ and the direction parallel to the defining edge. Normal and parallel components then assume linear behaviours on the RWG's support, as shown in figures 5.1 and 5.2, so they can be easily integrated analytically. Finally, if the support of $\boldsymbol{f}_m$ lies completely on the gap, the integral in 5.3 can be evaluated as

$$\begin{aligned} \mathrm{e}_m = &-\frac{V_0}{d}\left[\frac{2}{3}\frac{1}{l_m}\left(A_m^- + A_m^+\right)\sin(\theta)\right] \\ &-\frac{V_0}{d}\left[\left(\frac{h_m^-}{12A_m^-}\left((l_m^{-+})^2 - (l_m^{--})^2\right) + \frac{h_m^+}{12A_m^+}\left((l_m^{+-})^2 - (l_m^{++})^2\right)\right)\cos(\theta)\right], \end{aligned} \tag{5.4}$$

where $h_m^{\pm}$ is the height of triangle $c_m^{\pm}$ normal to the defining edge, $l_m^{-\pm}$ is the projection of the vector $(\boldsymbol{r}_m^- - \boldsymbol{v}_m^{\pm})$ on the defining edge, $l_m^{+\pm}$ is the projection of the vector $(\boldsymbol{r}_m^+ - \boldsymbol{v}_m^{\pm})$ on the defining edge. Just the terms relative to one of the two triangles are taken into account if the support of $\boldsymbol{f}_m$ is not completely included in the gap.

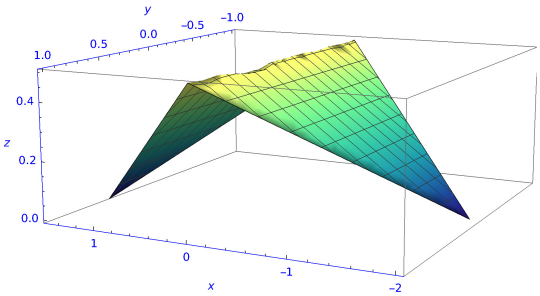

Figure 5.1: Representation of the RWG functions' component normal to the defining edge.

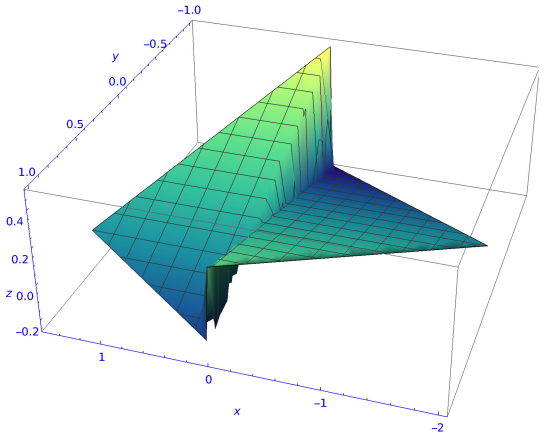

Figure 5.2: Representation of the RWG functions' component parallel to the defining edge.

5.1.2 Delta voltage gap

The kind of excitation presented in the previous section is customarily re-considered in the limit $d \to 0$. In this case, the exciting field in eq. (5.1) can be written as

$$\boldsymbol{E}^{inc}(\boldsymbol{r}) \to \hat{\boldsymbol{z}}\, V_0\, \delta(\boldsymbol{r} - \boldsymbol{r}_g) \tag{5.5}$$

where $\delta(\boldsymbol{r} - \boldsymbol{r}_g)$ is the Dirac delta distribution centered in the infinitesimal thickness gap region.

The intersection between the feed region and the boundary of the wire structure considered so far is a circumference. A favorable choice is to define a mesh on Γ such that some edges are places to discretize this circumference, as shown in figure 5.3. At this point, just the elements of the RHS corresponding to testing with the RWG functions defined on these edges (in red in the figure) are non zero. They are evaluated as [40]

$$\mathrm{e}_m = -V_0 \iint_{\boldsymbol{r}' \in \Gamma} \boldsymbol{f}_m(\boldsymbol{r}') \cdot \hat{\boldsymbol{z}}\, \delta(\boldsymbol{r}' - \boldsymbol{r}_g) = -V_0. \tag{5.6}$$

This great simplification arises from the fact that $\boldsymbol{f}_m(\boldsymbol{r}') \cdot \hat{\boldsymbol{z}}$ is just the normal component of $\boldsymbol{f}_m$ evaluated at the gap and its value is constant over the edge at $1/l_m$. Finally, integration of the Dirac delta brings a l_m factor which simplifies.

The delta voltage gap excitation has been widely exploited in the field of electromagnetic simulations, by virtue of its ease of implementation and capability of modelling a potential difference with quite a good level of accuracy. During the thesis work, both types of voltage gap excitation have been successfully implemented. For sake of brevity and simplicity, only the results obtained from the delta voltage gap are presented in the following sections, given that the two models provide comparable results in all the cases considered.

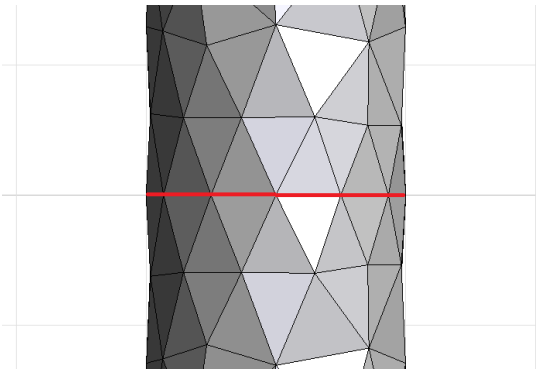

Figure 5.3: Example of mesh required for the implementation of the delta voltage gap.

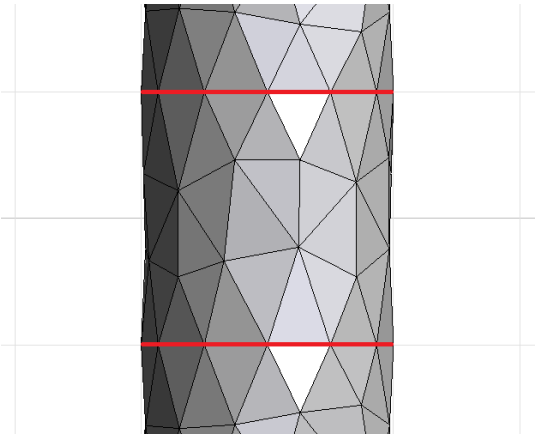

Figure 5.4: Example of mesh required for the implementation of the finite width voltage gap (the gap region lies between the red lines).

5.2 Toroidal inductor

5.2.1 Equivalent circuit and expected behaviour

In this section, a toroidal structure excited by a voltage gap is considered. The first step is to draw its equivalent circuit and to analyze its expected behaviour. The imposed voltage gap excites the toroidal global loop, so the excitation is called inductive and an RL circuit should be considered, shown in figure 5.5.

A preliminary analysis of the circuit is based on circuit theory considerations, valid under quasi-static assumptions. From the equivalent circuit, the potential difference imposed is expected to be balanced by the two voltage drops on the resistive and on the inductive parts: $V_0 = V_R + V_L$. To better understand these

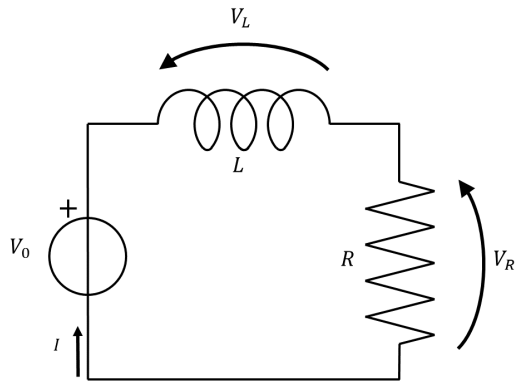

Figure 5.5: Circuital model of the structure under test: RL circuit.

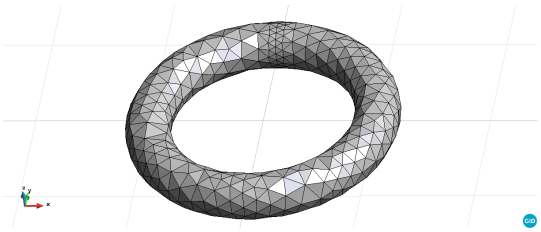

Figure 5.6: A mesh of the structure under test, a torus.

voltage contributions, the electric field inside the structure is written in terms of scalar and vector potentials,

$$\boldsymbol{E} = -j\omega\boldsymbol{A} - \nabla\phi_e. \tag{5.7}$$

Its circulation along a closed line is null in static conditions $\oint_{C_1} \boldsymbol{E} \cdot d\boldsymbol{l} = 0$ as it goes to zero when the frequency decreases. Thus only the part related to vector potential remains, since

$$\oint_{C_1=\partial S_1} \nabla\phi \cdot d\boldsymbol{l} = \iint_{S_1} (\nabla \times \nabla\phi_e) \cdot d\boldsymbol{S} = 0, \tag{5.8}$$

obtained from Stokes' theorem application and by recalling the vector calculus identity about curl of a gradient. Applying again Stokes' theorem on circulation of the electric field and recalling relation about magnetic field and electric vector potential $\boldsymbol{A}$, one obtains

$$\oint_{C_1} \boldsymbol{E} \cdot d\boldsymbol{l} = -\oint_{C_1} j\omega\boldsymbol{A} \cdot d\boldsymbol{l} = -\iint_{S_1} (\nabla \times j\omega\boldsymbol{A}) \cdot d\boldsymbol{S} = -j\omega\mu \iint_{S_1} \boldsymbol{H} \cdot d\boldsymbol{S}. \tag{5.9}$$

By letting C_1 being a toroidal closed loop inside the structure, as shown in figure 5.7, the left hand side of this equation becomes the circulation integral of the total electric field inside the structure, due to both excitation and reaction to it. In the voltage delta gap excitation case, it is a non classical field, containing a Dirac delta function at the excitation point. It is convenient to split the integral in two contributions: the line integral along an open line excluding the battery, called $C_{1,a}$, with the same length of the closed line C_1, and the line integral along an open line inside the battery, of infinitesimal length, called $C_{1,b}$, resulting in

$$\oint_{C_1} \boldsymbol{E} \cdot d\boldsymbol{l} = \int_{C_{1,a}} \boldsymbol{E} \cdot d\boldsymbol{l} + \int_{C_{1,b}} \boldsymbol{E} \cdot d\boldsymbol{l} \tag{5.10}$$

where $\int_{C_{1,b}} \boldsymbol{E} \cdot d\boldsymbol{l} = V_0$. Finally,

$$V_0 + \int_{C_{1,a}} \boldsymbol{E} \cdot d\boldsymbol{l} = -j\omega\mu \iint_{S_1} \boldsymbol{H} \cdot d\boldsymbol{S}. \tag{5.11}$$

In the term $-\int_{C_{1,a}} \boldsymbol{E} \cdot d\boldsymbol{l}$, it is possible to recognize the voltage drop on the resistive part

$$V_R = -\int_{C_{1,a}} \boldsymbol{E} \cdot d\boldsymbol{l}, \tag{5.12}$$

while, in the term $-j\omega\mu_0 \iint_{S_1} \boldsymbol{H} \cdot d\boldsymbol{S}$, the voltage drop on the inductive part

$$V_L = -j\omega\mu \iint_{S_1} \boldsymbol{H} \cdot d\boldsymbol{S}. \tag{5.13}$$

In statics, $V_0 = V_R$ and $V_L = 0$, consistently with the fact that the inductance can be modeled as a short circuit. For finite values of frequencies, the expected behaviour is given by $V_0 - V_R = V_L \to 0$.

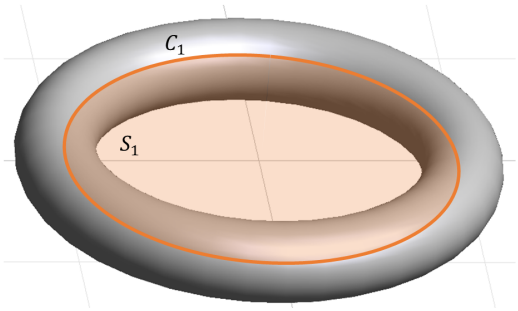

Figure 5.7: Representation of surface S_1 and contour $C_1 = \partial S_1$.

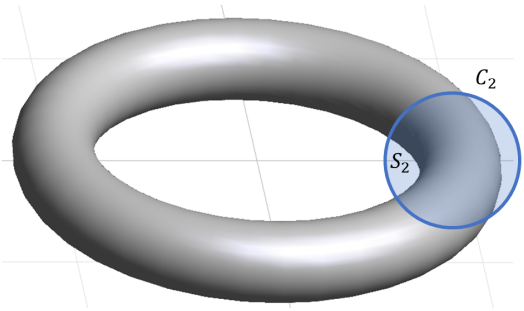

Figure 5.8: Representation of surface S_2 and contour $C_2 = \partial S_2$.

5.2.2 Numerical results at mid-frequency regime

The toroidal structure considered has major radius, i.e. distance from the origin to the central point of any cross section, $R_M = 1\,\text{m}$ and minor radius, i.e. radius of the cross section, $R_m = 0.2\,\text{m}$. Material parameters used are conductivity $\sigma = 1\,\text{S/m}$, real relative permittivity $\epsilon_r' = 1$, relative permeability $\mu_r = 1$. At the frequency of 100 kHz, the wavelength in free space is about $\lambda_0 \simeq 3{,}000\,\text{m}$, while in the medium it is $\lambda_1 \simeq 10\,\text{m}$. Characteristic size of the object is approximately $\lambda_1/5$, which means

a condition of mid-frequency regime. A potential difference of 1 mV is imposed to the structure.

The purpose of this section is to extract circuit parameters related to this structure from the solution of the PMCHWT formulation, i.e. the surface equivalent electric and magnetic currents. The only physical information which can be directly extracted from these equivalent currents is about the electric and magnetic fields scattered inside and outside the object. As already mentioned in section 5.1, it is reasonable to assume that the excitation imposed does not radiate outside the voltage gap region, so that the total electric and magnetic fields are the ones scattered by the currents.

Voltage drop across the circuit is measured as the sum of the potential differences across resistive and inductive parts, given by eq. (5.12) and eq. (5.13). Line and surface field integrations are required in the two cases. The first one can be performed by means of Simpson's integration rule, also called trapezoidal rule, more suited to the purpose than a Gaussian rule because of the loop nature of the integration domain. Instead, two-dimensional integration over a disk can be performed through the Gauss-Legendre rules found in [41]. Notice that surface S_1 enclosed by contour $C_{1,a}$ as represented in figure 5.7 is intersecting both the interior and the exterior of the structure, so the integral in eq. (5.13) involves magnetic field scattered inside and outside. Given the discontinuity of the first derivative of the magnetic field at the boundary between different materials, in order to correctly evaluate integral in eq. (5.12), it is convenient to split the integration domain in its interior and exterior parts and then sum the two contributions. Gauss integration rules over the two parts of the integration domain S_1, consisting of a disk and of a surface obtained from the difference between two concentric disks, are obtained in appendix A.

The current flowing in the structure can be measured in two different ways, either exploiting the second Maxwell's equation (1.2), also called Ampere's circuital law, or the Ohm's law:

$$I_1 = \oint_{C_2} \boldsymbol{H} \cdot d\boldsymbol{l} \tag{5.14}$$

$$I_2 = j\omega\epsilon_0\epsilon_r \iint_{S_2} \boldsymbol{E} \cdot d\boldsymbol{S} = (j\omega\epsilon_0\epsilon_r' + \sigma) \iint_{S_2} \boldsymbol{E} \cdot d\boldsymbol{S}. \tag{5.15}$$

In both cases, conduction and displacement currents are correctly detected, although conduction current is expected to be dominant in the eddy current frequency regime under study. As far as integration methods are concerned, similar considerations as for voltage measurement can be applied also in this case. As shown in figure 5.8, contour C_2 needs to be in the exterior of the object in order to retrieve the whole current flowing in it. From equation 5.15, it is clear that both conduction and displacement current are flowing in the interior of the structure, even if the first is

dominant, while just displacement current flows outside, given the assumption that the conductivity of the exterior medium is null.

From voltages and current, impedance of the circuit is easily obtained: $Z = R + j\omega L$, where $R = \Re\{(V_R + V_L)/I\}$ and $\omega L = \Im\{(V_R + V_L)/I\}$. Real and imaginary part operators in the previous relations are useful to take into account respectively the in-phase and in-quadrature parts of the total voltage drop across the circuit with respect to the current.

Measured voltage drops, current and derived values of resistance and inductance obtained for a toroidal surface discretized with 12,738 cells are shown in table 5.1. In terms of notation, R_x denotes resistance obtained from current measurement I_x; the same applies for L_x. In the table, the data denoted as BS, standing for Biot-Savart, is present. Given the simple geometry of the structure considered, the Biot-Savart law, valid under magneto-quasistatic conditions, permits the computation of the current flowing in the torus just from a measurement of the magnetic field in its center of symmetry (the origin in the reference system considered) in direction parallel to the axis of symmetry,

$$I_{BS} = 2R_M \boldsymbol{H}(\boldsymbol{r} = \boldsymbol{O}) \cdot \hat{\boldsymbol{z}}. \tag{5.16}$$

	$h = 4\,\text{cm}$, 12,738 basis functions	
V_R, mV	$(9.890 \times 10^{-1} - \text{j}3.453 \times 10^{-2})$	
V_L, mV	$(2.048 \times 10^{-3} + \text{j}3.431 \times 10^{-2})$	
I_1, µA	$(2.005 \times 10^{1} - \text{j}6.259 \times 10^{-1})$	
I_2, µA	$(1.932 \times 10^{1} - \text{j}6.011 \times 10^{-1})$	
I_{BS}, µA	$(2.026 \times 10^{1} - \text{j}7.638 \times 10^{-1})$	
R_1, Ω	49.38	$\lvert R_1 - R_i\rvert/\lvert R_i\rvert \simeq 0.01$
R_2, Ω	51.24	$\lvert R_2 - R_i\rvert/\lvert R_i\rvert \simeq 0.02$
R_{BS}, Ω	48.85	$\lvert R_{BS} - R_i\rvert/\lvert R_i\rvert \simeq 0.02$
L_1, µH	2.435	$\lvert L_1 - L_i\rvert/\lvert L_i\rvert \simeq 0.14$
L_2, µH	2.519	$\lvert L_2 - L_i\rvert/\lvert L_i\rvert \simeq 0.19$
L_{BS}, µH	2.914	$\lvert L_{BS} - L_i\rvert/\lvert L_i\rvert \simeq 0.37$

Table 5.1: Circuit parameters relative to a torus with major and minor radii of 1.0 m and 0.2 m discretized with approximately 8.5×10^3 elements (average mesh size $h \simeq 4\,\text{cm}$), $\sigma = 1\,\text{S/m}$. Voltage imposed is of value 1 mV at $f = 100\,\text{kHz}$.

Values of resistance and inductance reported in table 5.1 can be compared with the impedance predicted by circuit theory. From the so-called microscopical form

of Ohm's law, ideal resistance R_i is obtained as

$$R_i = \frac{l_{cond}}{\sigma A_{cross}} = 50\ \Omega, \tag{5.17}$$

where the length of the conductor is $l_{cond} = 2\pi R_M$ and the area of the wire cross section is $A_{cross} = \pi R_m^2$. Instead, theoretical value of auto-inductance of a toroidal structure can be obtained from [42]

$$L_i \simeq \mu_0 R_M \left(\ln \frac{8R_M}{R_m} - 2 \right) \simeq 2.12\ \mu\text{H}, \tag{5.18}$$

valid under the assumptions of current uniformly distributed over the wire cross section and $R_M \gg R_m$.

Finally, converging behaviour of the numerically obtained phasors is shown in figure 5.9. In particular, it is visible that, decreasing the mesh refinement parameter h, the total voltage drop across resistive and inductive parts converge to the imposed potential difference V_0 and that the values of current obtained from the two methods described above becomes nearer and nearer.

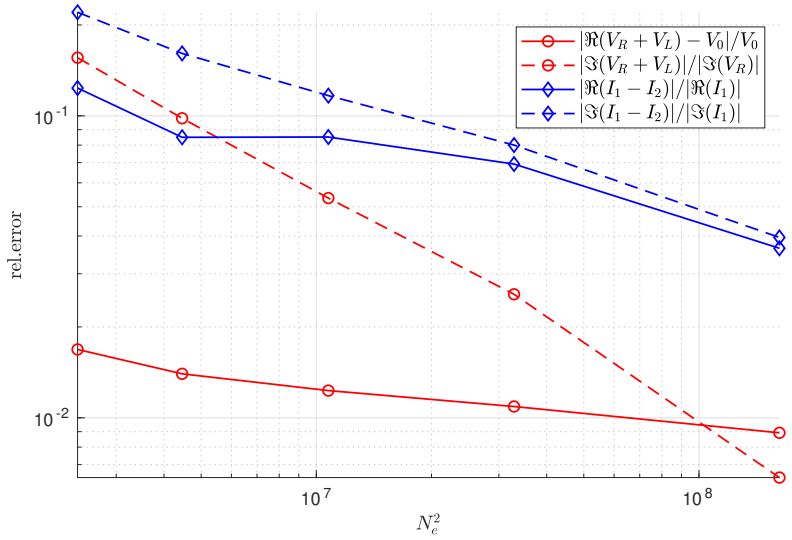

Figure 5.9: Relative error between voltages and currents evaluated from the two Maxwell's equations against mesh refinement.

A further insight on the fields

It is also interesting to observe the electric and magnetic fields behaviour inside and outside the structure. Results presented in the following are related to the same

geometry presented in the previous section under identical conditions. As clear from figures 5.10, 5.12, and 5.11, the electric field inside the structure is toroidally directed and with a magnitude constant along the azimuthal angle ϕ. Instead, the magnitude of $\boldsymbol{E}$ field in the cross section is linear with respect to $\sqrt{x^2+y^2}$, increasing toward the origin, in such a way that the line integral in 5.12 which gives the voltage across the structure is constant for any possible toroidal line $C_{1,a}$ inside the cross section.

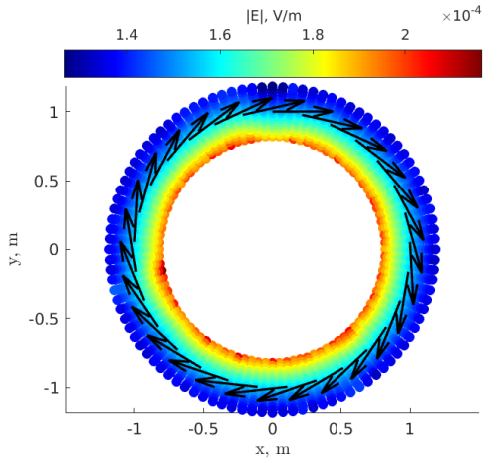

Figure 5.10: Electric field magnitude and direction inside the torus excited with a voltage gap of $V_0 = 1\,\mathrm{mV}$ in the plane $z = 0$.

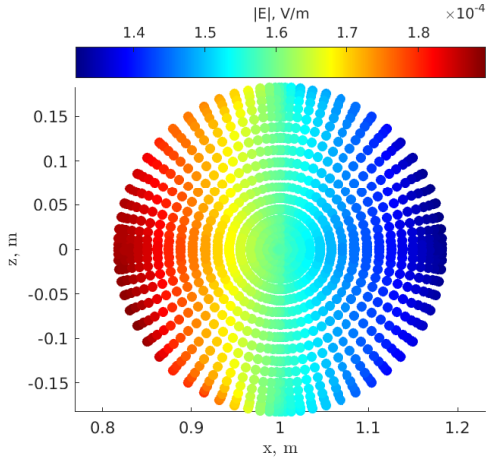

Figure 5.11: Electric field magnitude in a cross section of the torus excited with a voltage gap of $V_0 = 1\,\mathrm{mV}$, on the plane $y = 0$.

5.2.3 Frequency variation toward statics

To move toward low-frequency regime, it is necessary to take a deeper look at the voltage and current phasors related to the resistive and inductive parts of the structure, especially as far as frequency dependence is concerned. Their frequency behaviors are easily derived from circuit theory formulae as

$$V_R = \frac{V_0}{R + j\omega L} R \rightarrow \Re(V_R) = \mathcal{O}(1), \Im(V_R) = \mathcal{O}(\omega) \tag{5.19}$$

$$I = \frac{V_R}{R} \rightarrow \Re(I) = \mathcal{O}(1), \Im(I) = \mathcal{O}(\omega) \tag{5.20}$$

$$V_L = j\omega L I \rightarrow \Re(V_L) = \mathcal{O}(\omega^2), \Im(V_L) = \mathcal{O}(\omega). \tag{5.21}$$

Equations 5.19 and 5.21 should be interpreted in the following way: the voltage across resistance V_R is a complex phasor given by $V_R = V_0 e^{j\phi}$, lying in the complex

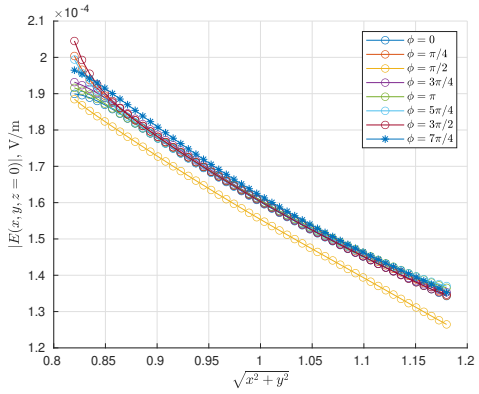

Figure 5.12: Electric field magnitude in the plane $z = 0$ in many cross sections. Azimuth angle ϕ is from direction $\hat{x}$ to $\hat{y}$.

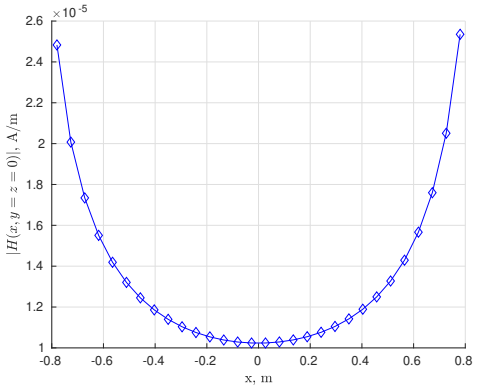

Figure 5.13: Magnetic field magnitude along a line lying in the "donut's hole", at $y = z = 0$.

plane in the circumference centered in the origin with radius V_0. When decreasing the frequency, ϕ goes to zero as ω, so $\Re(V_0 - V_R) = V_0 - V_0\cos(\phi) = \mathcal{O}(\phi^2) = \mathcal{O}(\omega^2)$. At the same time, $\Im(V_0 - V_R) = V_0\sin(\phi) = \mathcal{O}(\phi) = \mathcal{O}(\omega)$.

By recalling the way in which voltage and current phasors are evaluated, from equation 5.20 it is deduced that the expected frequency behaviour of the interior electric field flux integral across the cross section is $\mathcal{O}(1 + j\omega)$; from equation 5.21 it is derived that exterior magnetic field flux integral across S_1 goes like $\mathcal{O}(1 + j\omega)$ as well. Once theoretical scalings of fields and phasors have been clarified, it is necessary to check them numerically. The results of this analysis are shown in figure 5.14, from which it is visible that the extracted values of resistance and inductance remain constant in a wide frequency range.

In figure 5.15, frequency behaviour of the angles between the obtained phasors is shown: it is visible that, decreasing the frequency, the angle between V_R and the current decreases as ω, the absolute error on the angle between V_L and I with respect to $\pi/2$ decreases as ω as well. Indeed, decreasing the frequency, numerical results converge to the circuit theory scenario, in which voltage across a resistance is in phase with respect to current flowing in it, while voltage across an inductance is in quadrature.

Finally, an analysis on the validity of the magneto quasi-static approximation on the structure under test has been carried out. The two quantities

$$I_2 = (j\omega\epsilon_0\epsilon_r' + \sigma) \iint_{S_2} \boldsymbol{E} \cdot d\boldsymbol{S} \tag{5.22}$$

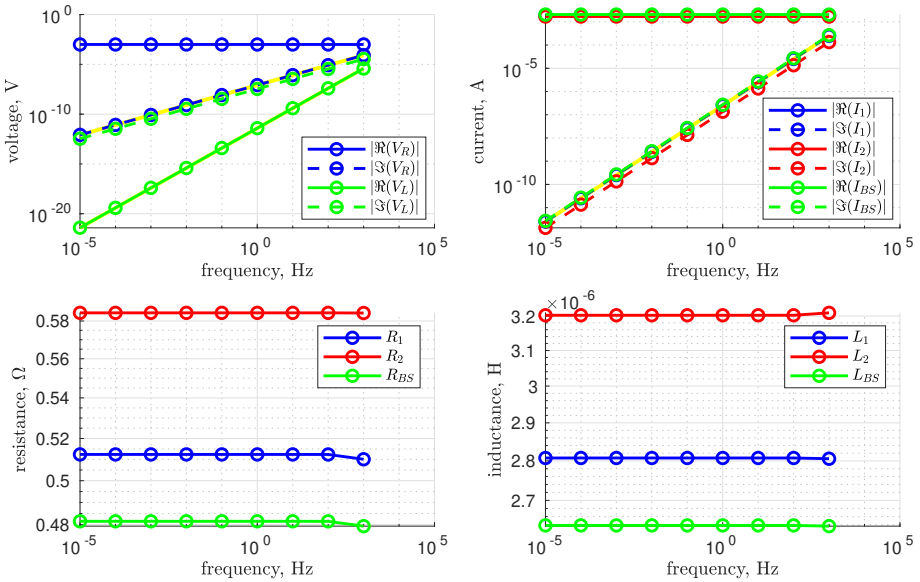

Figure 5.14: Frequency behaviour of extracted system parameters for a toroidal inductor with major and minor radii of 1.0 m and 0.2 m discretized with approximately 1.5×10^3 elements (average mesh size $h \simeq 12$ cm), $\sigma = 100$ S/m. Voltage imposed is of value 1 mV.

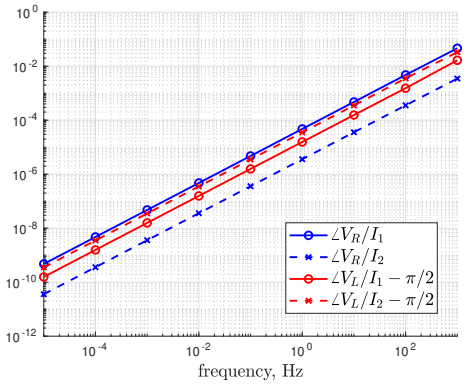

Figure 5.15: Frequency behaviour of angles between voltage and current phasors.

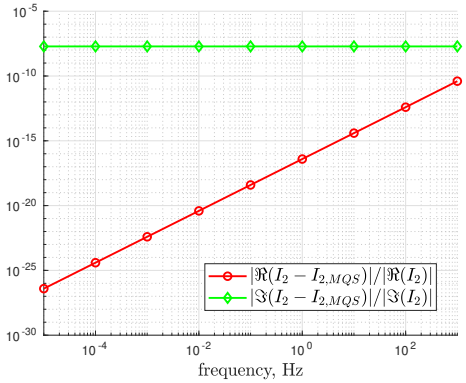

Figure 5.16: Analysis on validity of the MQS approximation: relative error between I_2 and $I_{2,MQS}$.

$$I_{2,MQS} = \sigma \iint_{S_{2,a}} \boldsymbol{E} \cdot d\boldsymbol{S} \tag{5.23}$$

are considered, where $S_{2,a}$ is defined as the intersection between S_2 and the interior of the structure. Figure 5.16 shows the relative contribution of $j\omega\epsilon_0\epsilon'_r \iint_{(S_2-S_{2,a})} \boldsymbol{E}\cdot d\boldsymbol{S}$ on the integral I_2, in its real and imaginary parts. The represented behaviour is consistent with the theoretically expected (and numerically checked) frequency behaviour of the electric field. It follows that the real part relative contribution decreases in frequency as ω, while the imaginary one is constant and low (in the order of 10^{-8}), leading to an absolute contribution decreasing as ω. These results confirm validity of the magneto-quasistatic approximation $I_2 \simeq I_{2,MQS}$ and its increasing accuracy moving toward lower frequency.

5.3 Parallel plates capacitor

5.3.1 Equivalent circuit and expected behaviour

The structure under study in this section is made of a couple of circular parallel plates connected by a thin strip, represented in figure 5.18. As for the toroidal inductor, a preliminary study of the equivalent circuit under quasi-static approximation is going to allow an overview on the expected behaviour of the fields. In this case, no global loop is excited by the voltage gap, so the excitation is classified as capacitive and the equivalent circuit is of RC type, shown in figure 5.17.

By applying Kirchoff voltage law to the circuit, the imposed voltage V_0 is expected to be balanced by the sum of the voltage drop on the resistance V_R and of the voltage drop on the capacitance V_C: $V_0 = V_R + V_C$. Current flowing through the resistance is mainly conductive in the eddy current frequency regime examined, characterized by $\omega\epsilon_0 \ll \sigma$, while current flowing through the capacitance is of displacement type. Symmetrically to what done for the toroidal inductor, it is possible to write the magnetic field in terms on magnetic scalar and vector potentials, as

$$\boldsymbol{H} = -j\omega\boldsymbol{F} - \nabla\phi_m. \tag{5.24}$$

Circulation of the magnetic field along the closed line C_1 gives the total current flowing across the surface S_1, equal to the difference between the conduction current across the strip connecting the plates and the displacement current flowing between the plates. As in the previous section, by exploitation of Stokes theorem, the following relation is obtained:

$$\oint_{C_1} \boldsymbol{H}\cdot d\boldsymbol{l} = -\oint_{C_1} j\omega\boldsymbol{F}\cdot d\boldsymbol{l} = -\iint_{S_1} (\nabla\times j\omega\boldsymbol{F})\cdot d\boldsymbol{S} = j\omega\epsilon \iint_{S_1} \boldsymbol{E}\cdot d\boldsymbol{S}. \tag{5.25}$$

It is convenient to split the surface S_1 in two parts: the one crossing the strip called S'_1 and the rest, $S''_1 = S_1 - S'_1$. So, the last integral becomes

$$j\omega\epsilon \iint_{S_1} \boldsymbol{E}\cdot d\boldsymbol{S} = j\omega\epsilon_0\epsilon_r \iint_{S'_1} \boldsymbol{E}\cdot d\boldsymbol{S} + j\omega\epsilon_0 \iint_{S''_1} \boldsymbol{E}\cdot d\boldsymbol{S} \tag{5.26}$$

where in the first term $j\omega\epsilon_0\epsilon_r \simeq \sigma$. So, it is possible to recognize in the first term the current flowing through the strip,

$$I_C = j\omega\epsilon_0\epsilon_r \iint_{S_1'} \boldsymbol{E} \cdot d\boldsymbol{S} \simeq \sigma \iint_{S_1'} \boldsymbol{E} \cdot d\boldsymbol{S}, \tag{5.27}$$

in the second term, the displacement current flowing between the plates changed in sign,

$$I_D = -j\omega\epsilon_0 \iint_{S_1''} \boldsymbol{E} \cdot d\boldsymbol{S}. \tag{5.28}$$

Given the arrangement of the equivalent circuit, it is clear that $I_C = I_D$. When decreasing the frequency, the displacement current is expected to vanish, so as the conduction current across the strip. It is consistent with the modelling of the capacitor as an open circuit in static regime.

5.3.2 Numerical results at mid frequency regime

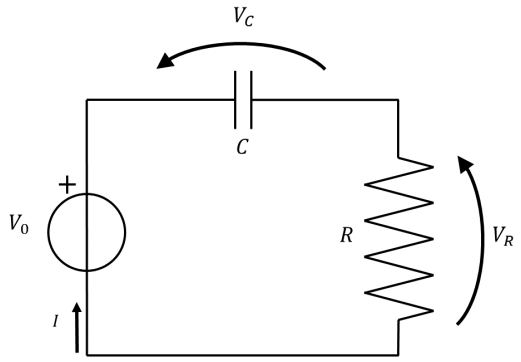

Figure 5.17: Circuital model of the structure under test: RC circuit.

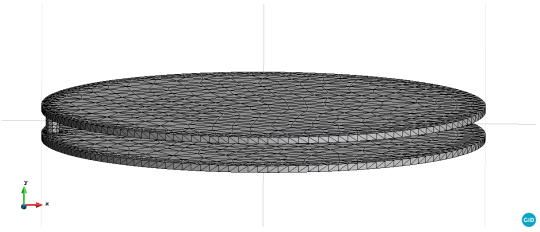

Figure 5.18: A mesh of the structure under test: a parallel plates capacitor.

The two parallel plates are of circular shape with radius $R = 1\,\text{m}$, thickness $1\,\text{cm}$; their separation is of $d = 10\,\text{cm}$. The strip connecting the plates is cylindrical, with cross section's radius of $3\,\text{cm}$, placed at the border of the plates. Same material parameters and frequency as in section 5.2.2 are used, so that the characteristic size of the object is approximately $\lambda_1/5$. The potential difference imposed is $10\,\text{mV}$.

The potential difference between the two plates can be measured directly as the line integral of the electric field along any path connecting them. It represents the voltage drop on the capacitance:

$$V_C = \int_{l_1} \boldsymbol{E} \cdot d\boldsymbol{l}. \tag{5.29}$$

This one-dimensional integration over a segment can be easily handled through Gauss-Legendre integration rules. Voltage across the resistive part cannot be measured directly, but is derived as

$$V_R = V_0 - V_C. \tag{5.30}$$

Finally, the current flowing in the circuit can be measured as the (mainly) conduction current flowing in the thin strip, theoretically equal to the displacement current flowing between the plates:

$$I = j\omega\epsilon_0\epsilon_r \iint_{S_1'} \boldsymbol{E} \cdot d\boldsymbol{S} = (j\omega\epsilon_0\epsilon_r' + \sigma) \iint_{S_1'} \boldsymbol{E} \cdot d\boldsymbol{S}. \tag{5.31}$$

Once voltages and current are known, impedance of the circuit is evaluated as $Z = R + 1/(j\omega C)$, where $R = \Re\{V_R/I\}$ and $\omega C = \Im\{I/V_C\}$. Results can be compared with theoretical values of resistance and capacitance known from circuit theory. In particular, the resistance of the whole structure is expected to be higher than resistance of the thin strip only, evaluated from the Ohm's law as

$$R_{i,strip} = \frac{l_{strip}}{\sigma A_{strip}} \simeq 35\Omega, \tag{5.32}$$

while the theoretical capacitance of the parallel plates is given by

$$C_i = \frac{\epsilon_0 A_{plate}}{d} = 278\text{pF}, \tag{5.33}$$

where A_{plate} is the area of the plate and the material between the plates is free space.

In table 5.2, the obtained circuit parameters are obtained for the structure discretized by means of 4,893 elements, given an excitation at frequency 100 kHz.

	4,893 basis functions	
V_C, mV	$(9.995 - \text{j}2.302 \times 10^{-1})$	
V_R, mV	$(4.743 \times 10^{-3} + \text{j}2.302 \times 10^{-1})$	
I, µA	$(4.022 \times 10^{-2} - \text{j}1.825)$	
C, pF	290.6	$\lvert C - C_i\rvert/\lvert C_i\rvert \simeq 0.04$
R, Ω	126.1	

Table 5.2: Circuit parameters relative to a parallel plates capacitor with circular plates of radius 1 m at distance 10 cm discretized with approximately 5×10^3 elements, $\sigma = 1$ S/m. Voltage imposed is of value 10 mV at $f = 100$ kHz.

The obtained capacitance is affected by a relative error of about 4% with respect to the ideal value, which can be lowered by mesh refinement. Moreover, also the capacitance behaviour when increasing the distance between plates is the one expected from theory: it decreases to 147 pF at $d = 20$ cm, to 86.8 pF at $d = 30$ cm.

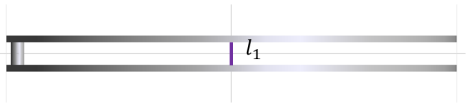

Figure 5.19: Representation of line l_1.

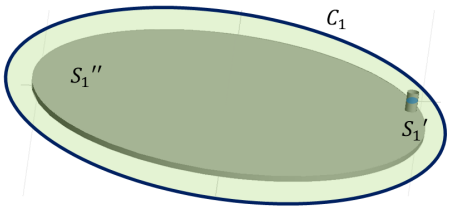

Figure 5.20: Representation of surfaces S_1', S_1'', such that $S_1' + S_1'' = S_1$, and contour $C_1 = \partial S_1$ (upper plate has been removed for sake of clarity).

A further insight on the fields

It is also interesting to notice that the electric field between the two plates is quite uniform, apart from near the string, and normal to the plates, as shown in figures 5.21 and 5.22.

5.3.3 Frequency variation toward statics

As in the case of the RL circuit, it is necessary to evaluate theoretical scalings of voltage and current phasors, which provide a reference for numerical results. Moving toward statics, the capacitor can be modeled as an open circuit. The current flowing in the structure is expected to decrease when decreasing the frequency, so that the whole potential difference imposed drops on the capacitive part. Frequency scaling of phasor V_R is derived as

$$V_R = \frac{V_0}{R + \frac{1}{j\omega C}} R \rightarrow \Re(V_R) = \mathcal{O}(\omega^2), \Im(V_R) = \mathcal{O}(\omega). \tag{5.34}$$

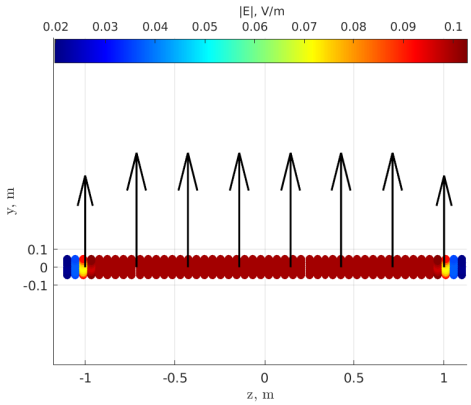

Figure 5.21: Electric field magnitude and direction between the plates of the capacitor excited with a voltage gap of $V_0 = 10\,\mathrm{mV}$, in the plane $z = 0$ normal to them.

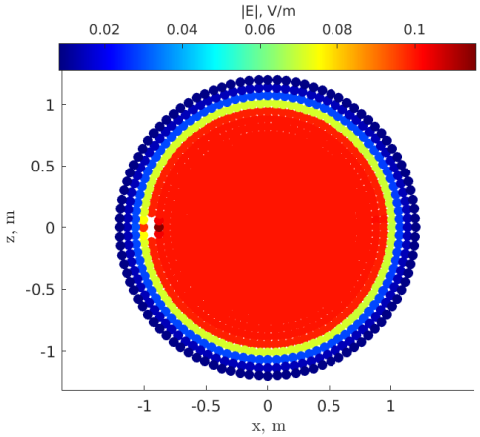

Figure 5.22: Electric field magnitude between the plates of the capacitor excited with a voltage gap of $V_0 = 10\,\mathrm{mV}$, in the plane $y = 0$ parallel to them.

By consequence,

$$V_C = V_0 - V_R \rightarrow \Re(V_C) = \mathcal{O}(1), \Im(V_C) = \mathcal{O}(\omega) \tag{5.35}$$

$$I = \frac{V_R}{R} \rightarrow \Re(I) = \mathcal{O}(\omega^2), \Im(I) = \mathcal{O}(\omega). \tag{5.36}$$

These are consistent with numerical results, shown in figure 5.23. Extracted values of resistance and capacitance are thus constant in frequency.

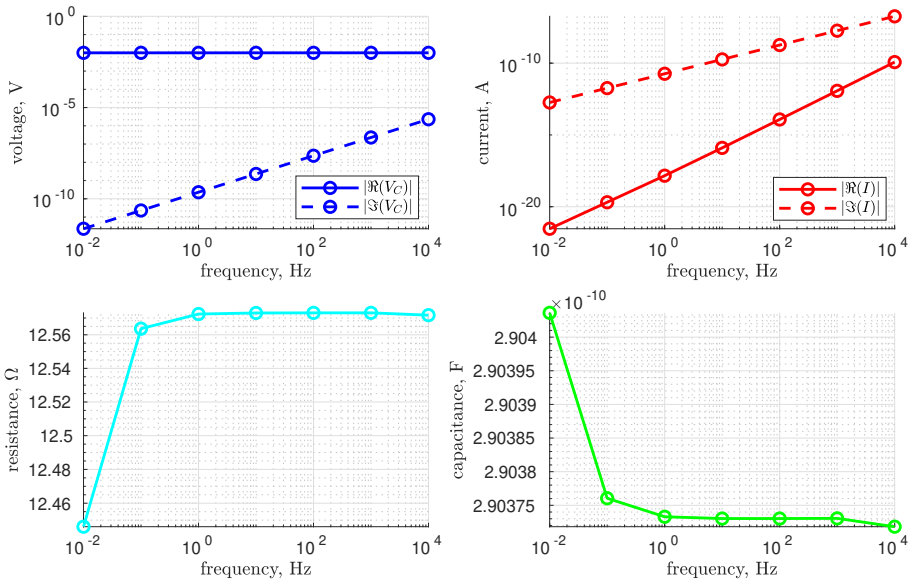

Figure 5.23: Frequency behaviour of extracted system parameters for a capacitor made of parallel circular plates of radius 1.0 m discretized with approximately 3×10^3 elements, $\sigma = 10\,\mathrm{S/m}$. Voltage imposed is of value 10 mV.

Chapter 6

Integration of highly lossy materials' Green's function

6.1 Overview of the issue

The PMCHWT formulation addressed in this work requires, for the building of the interaction matrix, explicit evaluation of integrals involving the Green's function in the interior lossy medium. This is an additional difficulty with respect to exterior integral equation problems, in which only Green's functions in free-space background media (not lossy) are integrated to build the formulation. The issue arises from the finite conductivity term, σ, which leads to a complex wavenumber, translated into an exponential damping of the Green's function with the space constant $-1/\Im(k)$,

$$G(\boldsymbol{r}-\boldsymbol{r}') = \frac{e^{-jkR}}{4\pi R} = \frac{1}{4\pi R}\left[e^{-j\,\Re(k)\,R}\,e^{\Im(k)\,R}\right], \tag{6.1}$$

where $R = |\boldsymbol{r}-\boldsymbol{r}'|$, $k = \omega\sqrt{\mu(\epsilon_0\epsilon_r' - j\frac{\sigma}{\omega})}$, $\Im(k) < 0$.

In the eddy current regime, characterized by $\omega\epsilon_0 \ll \sigma$, the approximation $k \simeq (1-j)/\delta$ holds true, with $\delta = \sqrt{2/(\omega\sigma\mu)}$ being the skin depth. As a consequence, real and imaginary parts of the wavenumber take approximately the same value in modulus, leading to a strict correlation between wavelength and damping space constant, both proportional to $1/\sqrt{\omega\sigma}$.

Once fixed the electrical size of the objects under test, the damping constant (normalized with respect to the characteristic size considered) is σ dependent, as shown in figure 6.1. To the Green's function decay in R related to the static part of G, $1/(4\pi R)$, in black in figure, it is generally superimposed the exponential damping due to material losses, $\exp(\Im(k)\,R)$. Finally, the visible oscillations are related to the dynamic, lossless, component of the Green's function, $\exp(-j\,\Re(k)\,R)$.

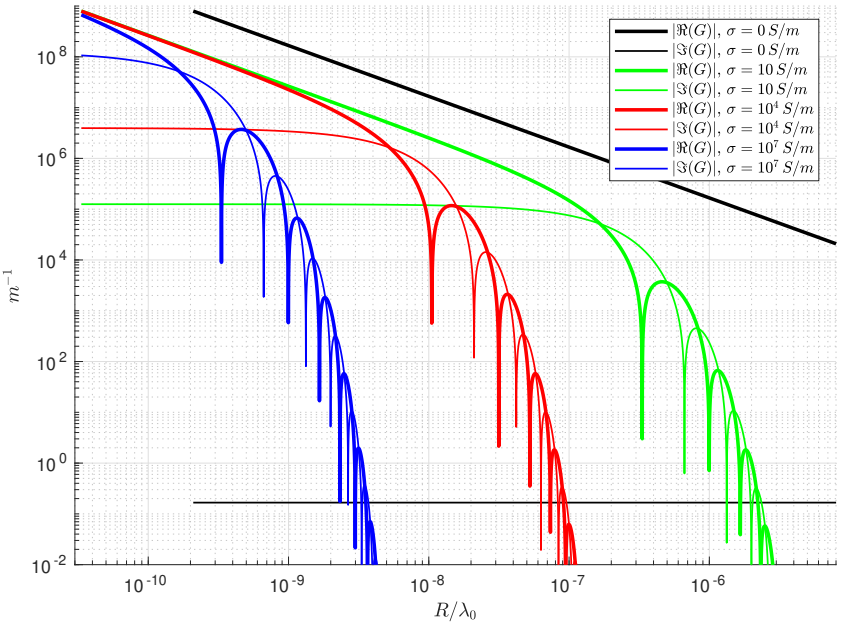

Figure 6.1: Green's function decay at different values of conductivities.

To better understand the issue under test in relation to integral equations' solution, consider for example the interaction matrices arising from discretization of the interior EFIE and MFIE (equations 2.28 and 2.29). Fixed the conductivity and the mesh, sparsity of such matrices is highly frequency dependent: at lower frequencies, they can be full or almost full because of the weak exponential decay of the Green's function with distance R; increasing the frequency, far interactions become progressively less significant and the matrices' structure moves toward diagonality. The same considerations can be done when fixing the frequency instead and increasing the conductivity, as the spatial damping coefficient is proportional to $1/\sqrt{\omega\sigma}$ as already noticed. A broadband integration technique, capable of providing sufficient accuracy in case of both near and far interactions, without changing drastically the discretization refinement depending on frequency and conductivity, is needed; a discussion on possible strategies is the topic of this chapter.

From figure 6.1, it is also visible that the wavelength inside the lossy medium decreases when increasing conductivity as $\mathcal{O}(1/\sqrt{\sigma})$. Indeed, it can be evaluated as $\lambda_1 = \Re\left(\frac{c_0}{\sqrt{\epsilon_r\mu_r}f}\right) \simeq 2\pi\delta = 2\pi\sqrt{2/(\omega\sigma\mu_1)}$ in the eddy current regime. From a comparison with the values of wavelength in the background medium λ_0 (assumed to be air), shown in figure 6.2, it is clear that, depending on the frequency and on the conductivity considered, the interior wavelength can be significantly shorter than the

exterior one. Average edge length of the Γ discretization on which the PMCHWT integral equation is formulated should be chosen such as to satisfy Shannon theorem requirements on the shorter (interior) wavelength involved: $h < \lambda_1/2 \simeq \pi\delta$. Figure 6.2 can give an idea of the discretization to be used for a certain range of frequency and conductivity values.

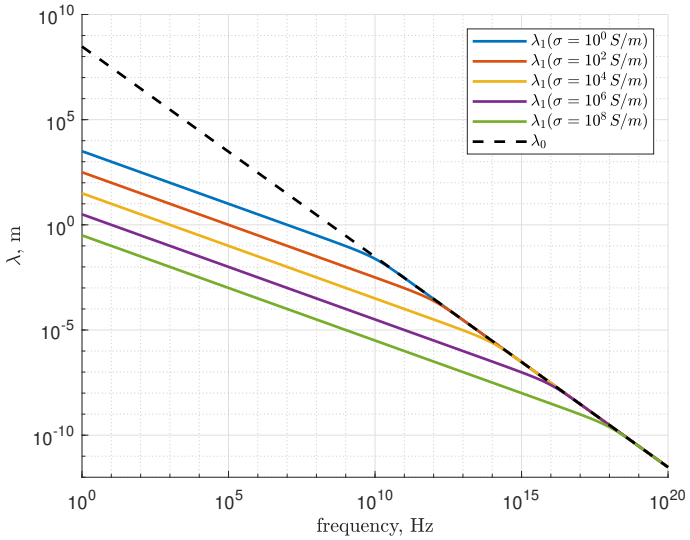

Figure 6.2: Comparison between interior and exterior wavelength at different values of conductivities.

However, this limitation on the average edge size can lead to dramatic increase of computational complexity. Consider for example the case of a copper sphere with radius 5 mm ($\sigma = 5.8 \times 10^7$ S/m), simulated at the frequency of 1 MHz. Values of outside and inside wavelengths are approximately $\lambda_0 = 300$ m and $\lambda_1 = 0.4$ mm: discretization parameters for the exterior problem are chosen to describe accurately the geometry (figure 6.3), while, for the interior problem, the limitation $h < \lambda_1/2$ is stringent and leads to an overdiscretized mesh (figure 6.4). The increase in complexity is even more dramatic when considering larger structure, since, up to characteristic sizes in the order of hundreds of meters, discretization for the exterior problem is only determined by geometrical considerations. The number of unknowns in the system increases as $1/h^2 = \mathcal{O}(\omega\sigma)$, becoming soon unacceptable.

It would be desirable to formulate an integration scheme capable of overcoming this stringent limit, allowing to build the MoM matrix with sufficient accuracy even on a discretization similar to the one which would have been used for the exterior problem only. This is possible indeed, because of the overdamped nature of the lossy Green's function, which masks its oscillatory behaviour.

Before presenting the integration schemes considered in this work, it can be useful

to introduce briefly integration and singularity extraction techniques commonly used to build the interaction matrices.

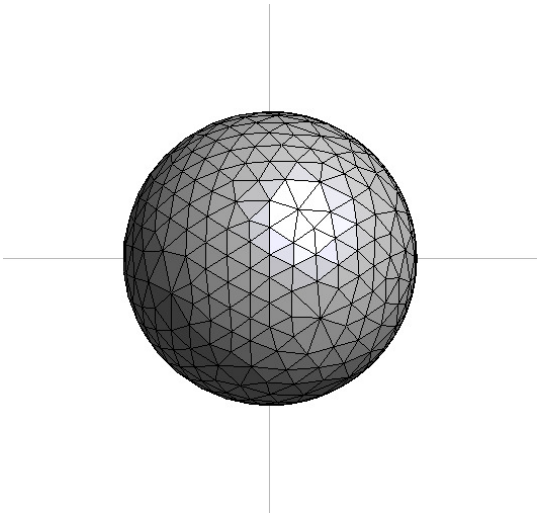

Figure 6.3: Sphere of radius 5 mm discretized with 922 elements, $h = 0.8$ mm.

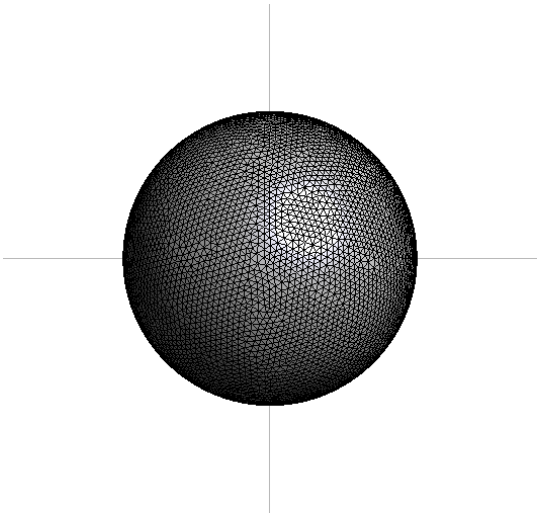

Figure 6.4: Sphere of radius 5 mm discretized with 13,742 elements, $h = 0.2$ mm.

6.2 Introduction to singularity extraction

Given an RWG functional space, the MoM matrices used to solve the most common integral formulations are

$$[\mathbf{T}_A]_{mn} = \iint_{\boldsymbol{r}\in\Gamma} \boldsymbol{f}_m(\boldsymbol{r}) \cdot \iint_{\boldsymbol{r}'\in\Gamma} G(\boldsymbol{r}-\boldsymbol{r}')\boldsymbol{f}_n(\boldsymbol{r}')dS'dS \tag{6.2}$$

$$[\mathbf{T}_\phi]_{mn} = -\iint_{\boldsymbol{r}\in\Gamma} \nabla\cdot\boldsymbol{f}_m(\boldsymbol{r}) \iint_{\boldsymbol{r}'\in\Gamma} G(\boldsymbol{r}-\boldsymbol{r}')\nabla'\cdot\boldsymbol{f}_n(\boldsymbol{r}')dS'dS \tag{6.3}$$

$$[\mathbf{K}]_{mn} = \iint_{\boldsymbol{r}\in\Gamma} \boldsymbol{f}_m(\boldsymbol{r}) \cdot \iint_{\boldsymbol{r}'\in\Gamma} \nabla G(\boldsymbol{r}-\boldsymbol{r}')\times\boldsymbol{f}_n(\boldsymbol{r}')dS'dS. \tag{6.4}$$

Whenever the supports of $\boldsymbol{f}_m$ and $\boldsymbol{f}_n$ are not-overlapping and far enough from each other, these integrals can be evaluated numerically by applying two-dimensional

Gaussian integration rules on triangles twice, respectively of order N and N',

$$[\mathbf{T}_A]_{mn} \simeq \sum_{i=1}^{N} \boldsymbol{f}_m(\boldsymbol{r}_i) \cdot \sum_{j=1}^{N'} G(\boldsymbol{r}_i - \boldsymbol{r}'_j) \boldsymbol{f}_n(\boldsymbol{r}'_j) w'_j w_i \tag{6.5}$$

$$[\mathbf{T}_\phi]_{mn} \simeq -\sum_{i=1}^{N} \nabla \cdot \boldsymbol{f}_m(\boldsymbol{r}_i) \sum_{j=1}^{N'} G(\boldsymbol{r}_i - \boldsymbol{r}'_j) \nabla' \cdot \boldsymbol{f}_n(\boldsymbol{r}'_j) w'_j w_i \tag{6.6}$$

$$[\mathbf{K}]_{mn} =\simeq \sum_{i=1}^{N} \boldsymbol{f}_m(\boldsymbol{r}_i) \cdot \sum_{j=1}^{N'} \nabla G(\boldsymbol{r}_i - \boldsymbol{r}'_j) \times \boldsymbol{f}_n(\boldsymbol{r}'_j) w'_j w_i, \tag{6.7}$$

where $\boldsymbol{r}_i$, $\boldsymbol{r}'_j$ are the sampling points on the supports of $\boldsymbol{f}_m$ and $\boldsymbol{f}_n$; w_i and w'_j are the corresponding Gaussian weights. A common quadrature rule is the Gauss-Legendre one, which integrates exactly polynomial kernels of orders up to $(2N-1)$, being N the rule's order. It can provide good results also for non polynomial kernels, but it produces inaccurate or completely wrong results when used to integrate singular functions.

This is the case of the above integrals when the supports of $\boldsymbol{f}_m$ and $\boldsymbol{f}_n$ are coinciding or just near. In such conditions, $\boldsymbol{r}_i \to \boldsymbol{r}'_j$ and the Green's functions, as well as its gradient, shows a singularity: special techniques should be exploited to perform the required integrations.

6.2.1 Singularity subtraction

The singularity subtraction technique [43, 44] is one of the oldest and most commonly used scheme to deal with singular kernels. The idea is to rewrite the singular integrand as the sum of its singular and non-singular parts, or equivalently to subtract and add to the integrand its singular part. On the one hand, the result of the subtraction between the total kernel and its singular part, called the regular part, is not singular anymore and can be integrated by means of quadrature rules; on the other hand, the singular remaining part can be evaluated analytically. For example, the Green's function $G(\boldsymbol{r} - \boldsymbol{r'})$ can be written as

$$G(\boldsymbol{r} - \boldsymbol{r'}) = \frac{e^{-jk|\boldsymbol{r}-\boldsymbol{r'}|} - 1}{4\pi|\boldsymbol{r} - \boldsymbol{r'}|} + \frac{1}{4\pi|\boldsymbol{r} - \boldsymbol{r'}|}, \tag{6.8}$$

where the first term constitutes the regular, while the second the singular part.

In figure 6.5, the Green's function behaviour is compared with the one of its regular part, for lossless and lossy media. The scalings of the real and imaginary parts for $R \to 0$ can be easily checked against the Taylor expansion

$$G(R) = \frac{1}{4\pi}\left[\frac{1}{R} - jk - k^2 R + \mathcal{O}(R^2)\right], \tag{6.9}$$

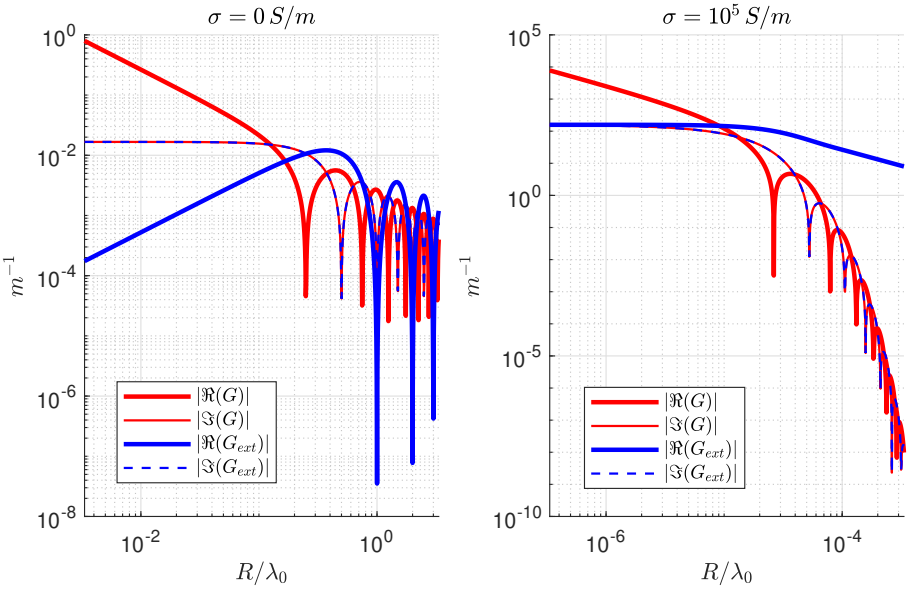

Figure 6.5: Comparison between the Green's function and its regular part in lossless and lossy media.

from which it is visible that, in the lossless case, $\Re(G) = \mathcal{O}(R^{-1})$, $\Im(G) = \mathcal{O}(1)$; extraction of the singular part affects only the real part of the Green's function and provokes a scaling $\Re(G_{ext}) = \mathcal{O}(R)$. The complex nature of the wavenumber in the lossy case leads instead to different scalings of the extracted Green's function. In particular $\Re(G_{ext}) = \mathcal{O}(1)$, while the imaginary part behaviour is unchanged from the subtraction operation.

6.2.2 Singularity cancellation

Singularity subtraction schemes have the drawback that many different special cases, for all possible kinds of kernels, have to be considered and coded for the analytic integration of the singular parts. In order to overcome this problem, many singularity cancellation schemes have been proposed during the years, the most promising of them can be found in [45–48]. Moreover, an higher level of accuracy can be usually achieved with respect to standard singularity subtraction approach.

They are all based on the application of a change of variables to the integrand function, such that the corresponding Jacobian appears inside the integral. Ideally, the performed change of variables is such that the Jacobian exactly cancels the singularity in the kernel and that the original triangular integration domain is mapped into a rectangular one.

In [49] and [50], two integration schemes based on singularity cancellation

are presented, specifically thought to alleviate the overdamped Green's function integration problem presented so far. They also exhibit the big advantage of reducing the two-dimensional integration to a one-dimensional only.

6.3 Solution strategies

6.3.1 Integration scheme A

In the following, the integration technique presented in [49] will be denoted as scheme A.

As in many other singularity cancellation schemes, the triangular integration domain T is decomposed into three sub-triangles with vertices in the vertices of the primal triangle and in the projection of the testing point on the plane of T, called $\boldsymbol{r}_o$. Notation of geometrical parameters used is represented in fig. 6.6.

In the case of current distribution being represented as linear combination of RWG functions $\boldsymbol{f}$, inner integrals to be evaluated are

$$I_{T_A} = \iint_T G(\boldsymbol{r}, \boldsymbol{r}')\boldsymbol{f}(\boldsymbol{r}')d\boldsymbol{r}' = \frac{1}{2A \cdot 4\pi}(I_b + \boldsymbol{\rho}_c I_a) \tag{6.10}$$

$$I_{T_\phi} = \iint_T G(\boldsymbol{r}, \boldsymbol{r}')\nabla' \cdot \boldsymbol{f}(\boldsymbol{r}')d\boldsymbol{r}' = \frac{1}{A \cdot 4\pi} I_b \tag{6.11}$$

$$I_K = \iint_T \nabla G(\boldsymbol{r}, \boldsymbol{r}') \times \boldsymbol{f}(\boldsymbol{r}')d\boldsymbol{r}' = \frac{1}{2A \cdot 4\pi}\left[\boldsymbol{R}_i \times (I_d + \boldsymbol{\rho}_c I_c)\right], \tag{6.12}$$

where $\boldsymbol{R}_i$ is the vector from the vertex of T opposite to its defining edge to the testing point $\boldsymbol{r}$, $\boldsymbol{\rho}_c$ is the vector from the same vertex to $\boldsymbol{r}_o$. Integrals I_a, I_b, I_c, I_d are defined as

$$I_a = \iint_{\boldsymbol{r}' \in T} \frac{e^{-jkR}}{R} d\boldsymbol{r}' \tag{6.13}$$

$$I_b = \iint_{\boldsymbol{r}' \in T} \boldsymbol{\rho}(\boldsymbol{r}') \frac{e^{-jkR}}{R} d\boldsymbol{r}' \tag{6.14}$$

$$I_c = \iint_{\boldsymbol{r}' \in T} \frac{e^{-jkR}(1 + jkR)}{R^3} d\boldsymbol{r}' \tag{6.15}$$

$$I_d = \iint_{\boldsymbol{r}' \in T} \boldsymbol{\rho}(\boldsymbol{r}') \frac{e^{-jkR}(1 + jkR)}{R^3} d\boldsymbol{r}', \tag{6.16}$$

with $\boldsymbol{\rho} = \boldsymbol{r}' - \boldsymbol{r}_o$. The scalar integrals I_a, I_c are evaluated as the sum of the integrals over the three sub-domains created. They can be rewritten through a change of variables in the spherical coordinates (θ, ρ). Then, by noticing that $RdR = \rho d\rho$, the inner integrand acquires an analytically integrable expression, so that just

the exterior $\theta-$ integration is left. It is finally transformed, with another change of variables, in an integration over the segment, boundary of T. Conversely, a vector calculus manipulation is used to transform the vectorial integrals I_b, I_d in integrals over the one-dimensional boundaries. All the relevant algebraic passages are reported in the paper. Finally, the integrals are evaluated as

$$I_a = \frac{1}{jk}\sum_{i=1}^{3}\int_{x_i^-}^{x_i^+} dx\alpha(x)\left[e^{-jkR(x)} - e^{-jkd}\right] \tag{6.17}$$

$$I_b = \frac{1}{jk}\sum_{i=1}^{3}\hat{\boldsymbol{u}}_i\int_{x_i^-}^{x_i^+} dx e^{-jkR(x)} \tag{6.18}$$

$$I_c = F\sum_{i=1}^{3}\int_{x_i^-}^{x_i^+} dx\alpha(x)\left[\frac{e^{-jkR(x)}}{R(x)} - \frac{e^{-jkd}}{d}\right] \tag{6.19}$$

$$I_d = F\sum_{i=1}^{3}\hat{\boldsymbol{u}}_i\int_{x_i^-}^{x_i^+} dx\frac{e^{-jkR(x)}}{R(x)}, \tag{6.20}$$

where $\alpha(x) = h_i/(h_i^2 + x^2)$, $R(x) = \sqrt{h_i^2 + d^2 + x^2}$, $d = |\boldsymbol{r} - \boldsymbol{r}_o|$. When $d = 0$, evaluation of I_c and I_d is not needed, since $\boldsymbol{R}_i$ results parallel to $(I_d + \boldsymbol{\rho}_c I_c)$ and I_K contribution vanishes. So, F parameter is used as a flag: it is equal to zero if $d = 0$, to one otherwise.

The biggest advantage of this formulation is that it just requires one-dimensional integration over segments. Then, some other considerations can be done. In I_a and I_c evaluation, the subtraction of two exponentials, in the case $R(x) \simeq d$, leads to a smoothing of the damping. Then, the I_a and I_c kernels' decay is determined primarily by the α factor, which is non-singular for $h_i \neq 0$. When instead h_i approaches zero, convergence slows down.

However, this integration technique is not expected to solve completely the problem under test: the highly damped and oscillating Green's function maintains these properties also on the edges of T, so its integration in case $\delta \ll h$ cannot be handled accurately in this context, as shown by the numerical results reported in the following.

6.3.2 Integration scheme B

Integration scheme B, presented in [50], exploits a different idea to evaluate I_a, I_b, I_c, I_d. Given the spherical symmetry of the Green's function, which represents indeed a spherical wave, the better choice of change of variables is from Cartesian to polar coordinates, in such a way that the integrand function is constant along θ, varying just along ρ. This allows a separability of the inner function in the product of a $\theta-$dependent part, analytically integrable, and a $\rho-$dependent part,

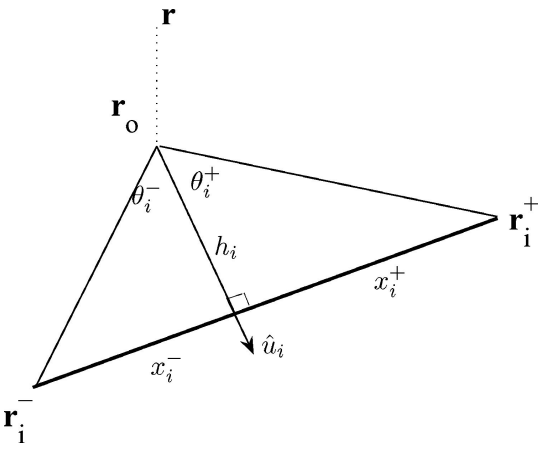

Figure 6.6: Notation referred to scheme A, taken from [49].

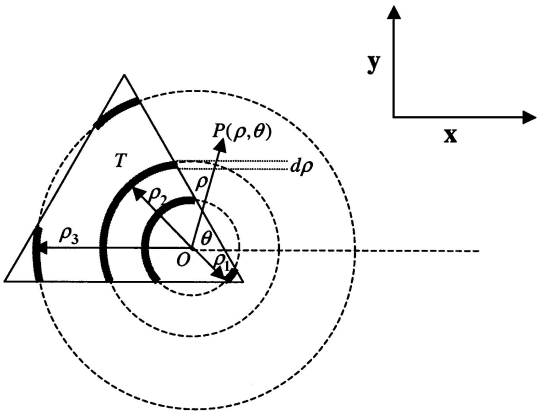

Figure 6.7: Notation referred to scheme B, taken from [50].

to be integrated numerically, leading to the reduction from two- to one-dimensional integration. The Jacobian of the transformation, to be introduced in the integral, cancels the singular part of the kernels for $R \to 0$, allowing an almost complete quench of the exponential damping.

As pointed out in [49], a complexity of this method resides in the evaluation of the θ intervals such that, for a given ρ, the point $(\rho, \theta) \in T$. This requires, for each values of ρ, the solution of three second order equations, arising from the search of intersections between the circumference centered in $\boldsymbol{r}_o$ with radius ρ and the three lines lying on the edges of the triangle T. Finally, the integrals to be evaluated are

$$I_a = \int_{\rho_{min}}^{\rho_{max}} \phi_{M,scal}(\rho)\xi_0(\rho)d\rho \tag{6.21}$$

$$I_b = \hat{\boldsymbol{x}} \int_{\rho_{min}}^{\rho_{max}} \phi_{M,vect}(\rho)\xi_c(\rho)d\rho + \hat{\boldsymbol{y}} \int_{\rho_{min}}^{\rho_{max}} \phi_{M,vect}(\rho)\xi_s(\rho)d\rho \tag{6.22}$$

$$I_c = \int_{\rho_{min}}^{\rho_{max}} \phi_{N,scal}(\rho)\xi_0(\rho)d\rho \tag{6.23}$$

$$I_d = \hat{\boldsymbol{x}} \int_{\rho_{min}}^{\rho_{max}} \phi_{N,scal}(\rho)\xi_c(\rho)d\rho + \hat{\boldsymbol{y}} \int_{\rho_{min}}^{\rho_{max}} \phi_{N,scal}(\rho)\xi_s(\rho)d\rho, \tag{6.24}$$

where ρ_{min}, ρ_{max} are the minimum and maximum values of ρ such that the point (ρ, θ) is in T for some value of θ; $\hat{\boldsymbol{x}}$ and $\hat{\boldsymbol{y}}$ coordinates are local to the triangle T.

The kernels' components are defined as

$$\phi_{M,scal}(\rho) = \frac{\rho e^{-jk\sqrt{\rho^2+d^2}}}{\sqrt{\rho^2+d^2}} \tag{6.25}$$

$$\phi_{M,vect}(\rho) = \frac{\rho^2 e^{-jk\sqrt{\rho^2+d^2}}}{\sqrt{\rho^2+d^2}} \tag{6.26}$$

$$\phi_{N,scal}(\rho) = \frac{\rho(1+jk\sqrt{\rho^2+d^2})e^{-jk\sqrt{\rho^2+d^2}}}{(\sqrt{\rho^2+d^2})^3} \tag{6.27}$$

$$\phi_{N,vect}(\rho) = \frac{\rho^2(1+jk\sqrt{\rho^2+d^2})e^{-jk\sqrt{\rho^2+d^2}}}{(\sqrt{\rho^2+d^2})^3} \tag{6.28}$$

$$\xi_0(\rho) = \sum_{i=1}^{K(\rho)} (\theta^i_{max}(\rho) - \theta^i_{min}(\rho)) \tag{6.29}$$

$$\xi_c(\rho) = \sum_{i=1}^{K(\rho)} (-\cos\theta^i_{max}(\rho) + \cos\theta^i_{min}(\rho)) \tag{6.30}$$

$$\xi_s(\rho) = \sum_{i=1}^{K(\rho)} (\sin\theta^i_{max}(\rho) - \sin\theta^i_{min}(\rho)), \tag{6.31}$$

where $K(\rho)$ is the number of intervals in θ such that, given a ρ, the point (ρ, θ) lies in T; $(\theta^i_{min}, \theta^i_{max})$ are the limits of these intervals.

6.3.3 Numerical results

Accuracy, limitations and validity ranges of the two integration schemes presented above will be explored in this section. Numerical results obtained are compared against the outcomes of `NIntegrate` function, included in *Wolfram Mathematica* environment. The integration domain considered, T, is the simplex triangle of vertices $\{\boldsymbol{O}, \alpha\hat{\boldsymbol{x}}, \alpha\hat{\boldsymbol{y}}\}$. Degrees of freedom of the simulation are (I) the position of the testing point $\boldsymbol{r}$ and (II) the ratio between skin depth and characteristic size of the triangle, $S = \delta/\alpha$; every ratio $S < 1/\pi \simeq 0.3$ does not satisfy Shannon sampling theorem. For every integral evaluated, its converging behaviour is analyzed for increasing number of integration points. In order to allow a fair comparison between the two techniques considered, the same number of integration points over the triangle is taken at each integration, meaning n points per segment for scheme A, $3n$ points distributed in $[\rho_{min}, \rho_{max}]$ for scheme B. Gauss-Legendre rules have been used to evaluate one-dimensional integrals in both cases.

In figure 6.8 a first comparison between the two integration schemes at $\boldsymbol{r} = (1/3,\, 1/3,\, 1)\,\alpha$, $S = 0.3$ is reported. As expected, from considerations in section 6.3.1, I_a and I_c converge faster than I_b and I_d when exploiting integration

technique A. In this conditions, scheme A provides better results than B. Increasing $\omega\sigma$ product instead (figure 6.9), convergence of technique A slows down significantly, while scheme B provides much more accurate results and fast convergence.

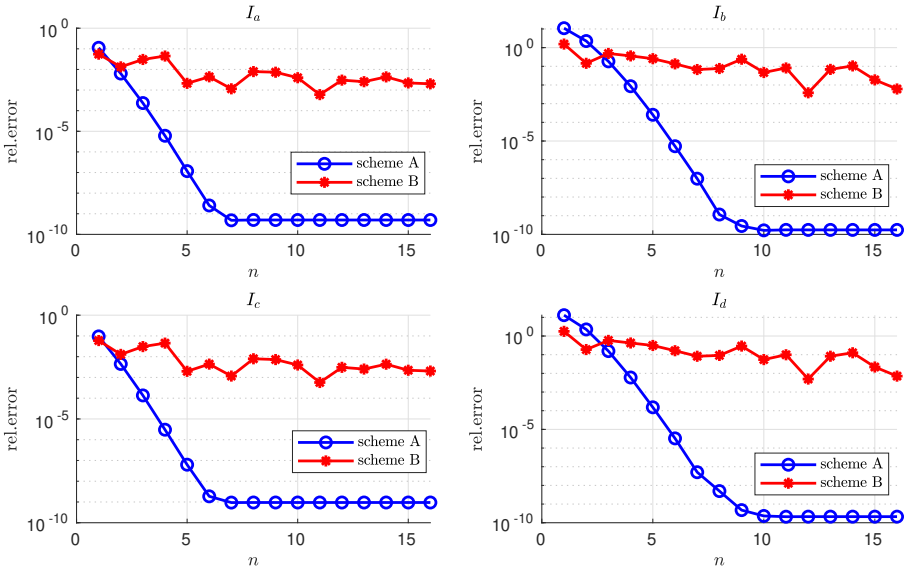

Figure 6.8: Comparison between scheme A and B at $\boldsymbol{r} = (1/3,\ 1/3,\ 1)\,\alpha$, $S = 0.3$.

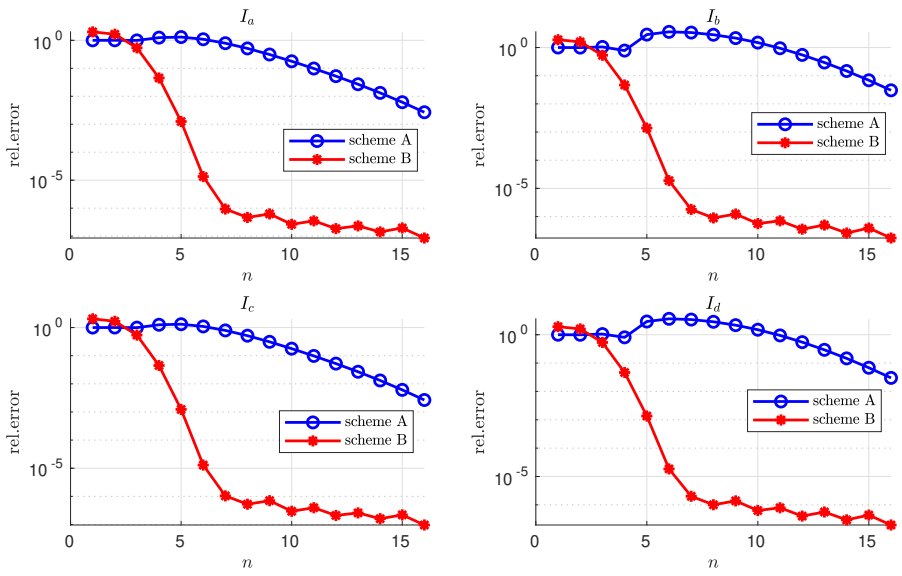

Figure 6.9: Comparison between scheme A and B at $\boldsymbol{r} = (1/3,\ 1/3,\ 1)\,\alpha$, $S = 0.01$.

In figures 6.10 and 6.11, relative errors against the ratio S are represented at different distances d, for testing points such that $\boldsymbol{r}_o$ lies inside and outside T respectively. Just I_a and I_b related results are shown, since I_c and I_d behaviours are similar to I_a, I_b ones. In both cases, it is clear that the errors produced from scheme A and B show opposite behaviours with S: when increasing the ratio $\omega\sigma$ (decreasing S), the error from technique A increases, while the one from technique B decreases.

From these results, it can be deduced that the integration scheme presented in [50] represents a valid strategy to fix the highly-conductivity Green's function integration issue, making it possible to formulate the PMCHWT problem over the same kinds of meshes that would be used to solve the exterior integral equations. It is also clear that a control on S should be implemented to decide wether to integrate by means of the standard singularity subtraction method, or by exploiting singularity cancellation scheme B, whose performance increases at lower values of δ/h.

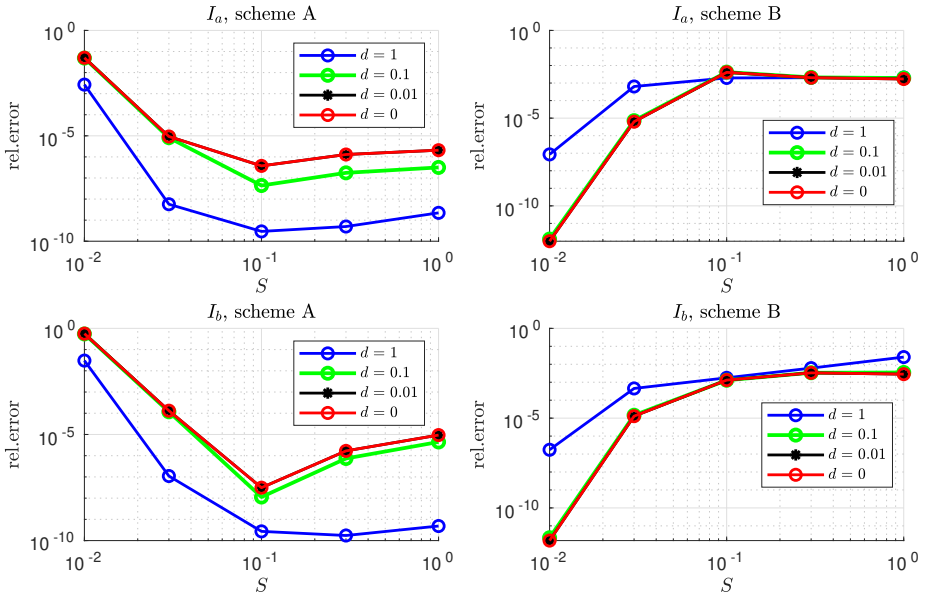

Figure 6.10: Comparison between scheme A and B at $\boldsymbol{r} = (1/3,\, 1/3,\, d)\,\alpha$, $n = 16$.

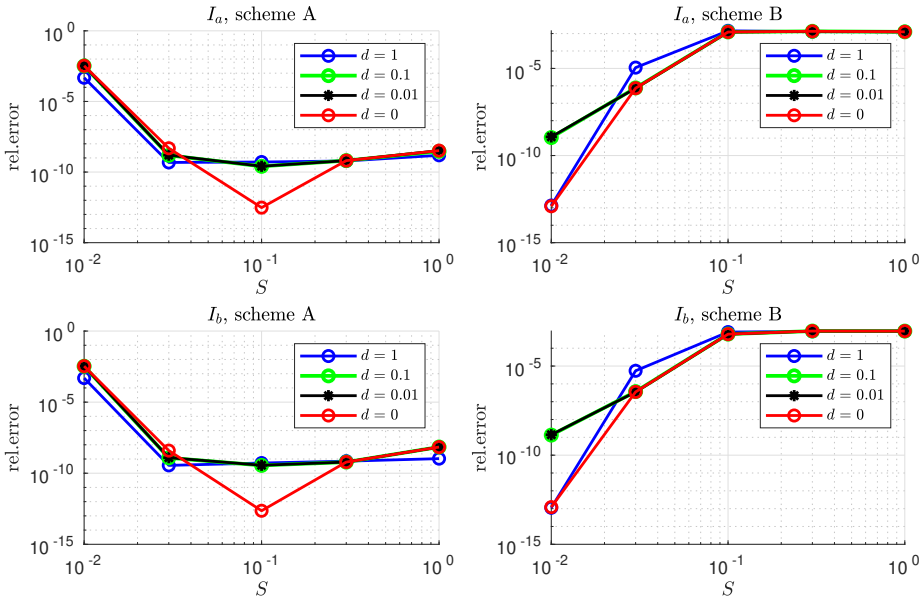

Figure 6.11: Comparison between scheme A and B at $\boldsymbol{r} = (1,\, 1,\, d)\,\alpha$, $n = 16$.

Chapter 7

Conclusions and future work

In this work, the low-frequency stable PMCHWT formulation presented in [2] has been widely validated against both analytical scattering models and expected field distributions on canonical circuital structures, well known from circuit theory. Then, promising results presented in chapter 6 set the possibility of further broadening the range of applicability of the solver, toward higher values of frequency and conductivity.

Future work will focus on additional developments of the formulation, in the perspective of making it usable for large and reliable simulations of complex realistic structures. To this purpose, potential research topics include:

- Acceleration of simulations by means of fast algebraic solvers, such as ACA and MLACA, fully compatible with the quasi-Helmholtz projectors based PMCHWT formulation under test.
- Implementation of an adaptive frequency-preconditioning strategy, in order to allow seamless transition between different frequency regimes, other than the eddy current one.
- Extension of the present PMCHWT formulation to a multi-layer version, capable of handling change of parameters between different layers. Successful realization of this and previous points would allow simulations of complex layered structures, such as printed circuit boards (PCBs).

Appendix A

Two-dimensional integration rules

In chapter 5, two-dimensional numerical integration is required in order to retrieve voltage and current of circuital structures. In particular, the domain of integration can be a disk or the difference between two concentric disks with different radii. In order to obtain Gauss-Legendre integration rules over these kinds of domains, it is necessary to perform a change of variable to transform them in the standard square, as explained in [41]. In this paper, the Jacobian matrix relative to the change of variable performed is calculated just for the unit disk domain, but it is trivial to extend the evaluation for the general case of $\rho \in [\rho_1, \rho_2]$, with $\rho_1 \neq 0$.

Assume that the integration domain is identified in spherical coordinate system by

$$\begin{cases} 0 \leq \phi \leq \pi/2 \\ \rho_1 \leq \rho \leq \rho_2 \\ \theta = 0 \end{cases} . \tag{A.1}$$

The proposed change of variable which transforms the domain in the standard square is

$$\rho = \frac{b-a}{2}\xi + \frac{b+a}{2} \tag{A.2}$$

$$\phi = \frac{\beta-\alpha}{2}\eta + \frac{\beta+\alpha}{2} \tag{A.3}$$

with $a = \rho_1$, $b = \rho_2$, $\alpha = 0$, $\beta = \pi/2$. The relation between the Cartesian and the

new coordinates, ξ and η, reads

$$x = \rho\cos\phi = \left(\frac{b-a}{2}\xi + \frac{b+a}{2}\right)\cos(\pi/4(\eta+1)) \tag{A.4}$$

$$y = \rho\sin\phi = \left(\frac{b-a}{2}\xi + \frac{b+a}{2}\right)\sin(\pi/4(\eta+1)). \tag{A.5}$$

From these simple relations, the determinant of the Jacobian matrix of the transformation is calculated as

$$\det(\boldsymbol{J}(\xi,\eta)) = \begin{vmatrix} \frac{dx}{d\xi} & \frac{dy}{d\xi} \\ \frac{dx}{d\eta} & \frac{dy}{d\eta} \end{vmatrix} = \frac{1}{16}(a-b)\,\pi\,[a(\xi-1) - b(\xi+1)], \tag{A.6}$$

consistent with the special case of $a = 0$, $b = 1$ reported in the paper. Finally, the integral under test $I = \iint_S f(x,y)\,dx\,dy$ is evaluated numerically as

$$I = \sum_{i=1}^{n}\sum_{j=1}^{n} \det(\boldsymbol{J}(\xi_i,\eta_j))w_i\,w_j\,f\left[x\left(\xi_i,\eta_j\right), y\left(\xi_i,\eta_j\right)\right], \tag{A.7}$$

where ξ_i, η_j are Gaussian points between -1 and 1, w_i, w_j are the corresponding Gaussian weights. Equality reported in A.7 is valid if the integrand f is a polynomial function $\xi^k\eta^l$ of degree $k+l$ up to $(n\cdot n-1)$ [51], [52].

To test the integration rule derived, volume of a cone can be calculated for example and then compared with the analytic result: the relative error obtained is in the order of machine precision for integration rules of order $n \geq 2$.

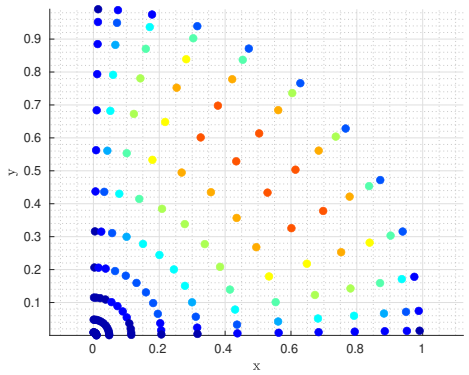

Figure A.1: Gauss-Legendre quadrature rule of order $n = 12$ in a quadrant of disk of radius 1.

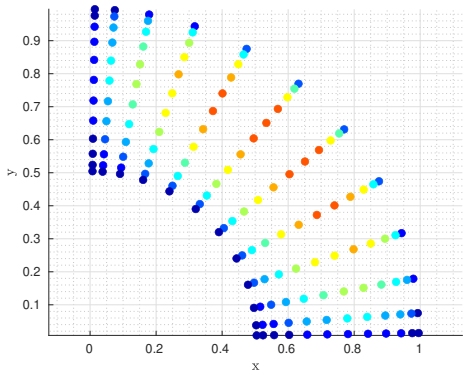

Figure A.2: Gauss-Legendre quadrature rule of order $n = 12$ in a quadrant of difference of disks of radii 1 and 0.5.

Bibliography

[1] Marc Bonnet and Edouard Demaldent. «The eddy current model as a low-frequency, high-conductivity asymptotic form of the Maxwell transmission problem». In: *Computers & Mathematics with Applications* 77.8 (2019), pp. 2145–2161 (cit. on pp. iii, 36).

[2] Tiffany L Chhim, Adrien Merlini, Lyes Rahmouni, John Erick Ortiz Guzman, and Francesco P Andriulli. «Eddy Current Modeling in Multiply Connected Regions via a Full-Wave Solver Based on the Quasi-Helmholtz Projectors». In: *IEEE Open Journal of Antennas and Propagation* 1 (2020), pp. 534–548 (cit. on pp. iii, 35, 38, 41, 42, 91).

[3] Constantine A Balanis. *Advanced engineering electromagnetics*. John Wiley & Sons, 2012 (cit. on p. 2).

[4] Leopold B Felsen and Nathan Marcuvitz. *Radiation and scattering of waves*. Vol. 31. John Wiley & Sons, 1994 (cit. on p. 6).

[5] Richard Phillips Feynman, Robert B Leighton, and Matthew Linzee Sands. *The Feynman Lectures on Physics: electromagnetism and matter*. Vol. 2. Addison-Wesley Publishing Company, 1964 (cit. on p. 8).

[6] Raymond A Serway and John W Jewett. *Physics for scientists and engineers*. Cengage learning, 2018 (cit. on p. 8).

[7] Jearl Walker et al. «Halliday & Resnick Fundamentals of Physics (Extended 10th Edition)». In: (2013) (cit. on p. 8).

[8] Hermann A Haus and James R Melcher. *Electromagnetic fields and energy*. Vol. 107. Prentice Hall Englewood Cliffs, NJ, 1989 (cit. on p. 8).

[9] Stefan A Sauter and Christoph Schwab. «Boundary element methods». In: *Boundary Element Methods*. Springer, 2010, pp. 183–287 (cit. on pp. 14, 15, 28).

[10] David L Colton, Rainer Kress, and Rainer Kress. *Inverse acoustic and electromagnetic scattering theory*. Vol. 93. Springer, 1998 (cit. on pp. 14, 15).

[11] Jean-Claude Nédélec. *Acoustic and electromagnetic equations: integral representations for harmonic problems*. Springer Science & Business Media, 2001 (cit. on pp. 14, 28).

[12] Andrew J Poggio and Edmund K Miller. *Integral equation solutions of three-dimensional scattering problems*. MB Assoc., 1970 (cit. on p. 16).

[13] Sadasiva Rao, Donald Wilton, and Allen Glisson. «Electromagnetic scattering by surfaces of arbitrary shape». In: *IEEE Transactions on antennas and propagation* 30.3 (1982), pp. 409–418 (cit. on p. 20).

[14] Annalisa Buffa and Snorre Christiansen. «A dual finite element complex on the barycentric refinement». In: *Mathematics of Computation* 76.260 (2007), pp. 1743–1769 (cit. on p. 20).

[15] Francesco P Andriulli, Kristof Cools, Hakan Bagci, Femke Olyslager, Annalisa Buffa, Snorre Christiansen, and Eric Michielssen. «A multiplicative Calderon preconditioner for the electric field integral equation». In: *IEEE Transactions on Antennas and Propagation* 56.8 (2008), pp. 2398–2412 (cit. on pp. 21, 28).

[16] Francesco P Andriulli. «Loop-star and loop-tree decompositions: Analysis and efficient algorithms». In: *IEEE Transactions on Antennas and Propagation* 60.5 (2012), pp. 2347–2356 (cit. on pp. 21, 22, 31).

[17] Kristof Cools, Francesco P Andriulli, Femke Olyslager, and Eric Michielssen. «Nullspaces of MFIE and Calderón preconditioned EFIE operators applied to toroidal surfaces». In: *IEEE Transactions on Antennas and Propagation* 57.10 (2009), pp. 3205–3215 (cit. on p. 23).

[18] Mario Bebendorf. «Approximation of boundary element matrices». In: *Numerische Mathematik* 86.4 (2000), pp. 565–589 (cit. on p. 26).

[19] Hongwei Cheng, Zydrunas Gimbutas, Per-Gunnar Martinsson, and Vladimir Rokhlin. «On the compression of low rank matrices». In: *SIAM Journal on Scientific Computing* 26.4 (2005), pp. 1389–1404 (cit. on p. 26).

[20] Leslie Greengard and Vladimir Rokhlin. «A fast algorithm for particle simulations». In: *Journal of computational physics* 73.2 (1987), pp. 325–348 (cit. on p. 26).

[21] Wolfgang Hackbusch. «A sparse matrix arithmetic based on h -matrices. Part I and II». In: *Computing* 62.2 (1999), pp. 89–108 (cit. on p. 26).

[22] Mario Bebendorf. *Hierarchical matrices*. Springer, 2008 (cit. on p. 26).

[23] Jiming Song, Cai-Cheng Lu, and Weng Cho Chew. «Multilevel fast multipole algorithm for electromagnetic scattering by large complex objects». In: *IEEE Transactions on Antennas and Propagation* 45.10 (1997), pp. 1488–1493 (cit. on p. 26).

[24] Jonathan Richard Shewchuk et al. *An introduction to the conjugate gradient method without the agonizing pain*. 1994 (cit. on p. 26).

[25] Xavier Antoine and Marion Darbas. «An introduction to operator preconditioning for the fast iterative integral equation solution of time-harmonic scattering problems». In: *Multiscale Science and Engineering* (2021), pp. 1–35 (cit. on p. 27).

[26] Francesco P Andriulli, Kristof Cools, Ignace Bogaert, and Eric Michielssen. «On a well-conditioned electric field integral operator for multiply connected geometries». In: *IEEE transactions on antennas and propagation* 61.4 (2012), pp. 2077–2087 (cit. on p. 28).

[27] DR Wilton. «Topological consideration in surface patch and volume cell modeling of electromagnetic scatterers». In: *Proc. URSI Int. Symp. Electromagn. Theory*. 1983, pp. 65–68 (cit. on p. 29).

[28] Carl D Meyer. *Matrix analysis and applied linear algebra*. Vol. 71. Siam, 2000 (cit. on p. 32).

[29] EE Kriezis, Theodoros D Tsiboukis, Stavros M Panas, and John A Tegopoulos. «Eddy currents: Theory and applications». In: *Proceedings of the IEEE* 80.10 (1992), pp. 1559–1589 (cit. on p. 35).

[30] Javier Garcìa-Martìn, Jaime Gòmez-Gil, and Ernesto Vàzquez-Sànchez. «Non-destructive techniques based on eddy current testing». In: *Sensors* 11.3 (2011), pp. 2525–2565 (cit. on p. 35).

[31] Wolfgang M Rucker, Robert Hoschek, and Kurt R Richter. «Various BEM formulations for calculating eddy currents in terms of field variables». In: *IEEE transactions on magnetics* 31.3 (1995), pp. 1336–1341 (cit. on p. 36).

[32] Gordon E Moore et al. *Cramming more components onto integrated circuits*. 1965 (cit. on p. 36).

[33] Siyuan Y Chen, Weng Cho Chew, Jiming M Song, and Jun-Sheng Zhao. «Analysis of low frequency scattering from penetrable scatterers». In: *IEEE Transactions on Geoscience and Remote Sensing* 39.4 (2001), pp. 726–735 (cit. on p. 38).

[34] Ignace Bogaert, Kristof Cools, FP Andriulli, and Daniël De Zutter. «Low frequency scaling of the mixed MFIE for scatterers with a non-simply connected surface». In: *2011 International Conference on Electromagnetics in Advanced Applications*. IEEE. 2011, pp. 951–954 (cit. on p. 38).

[35] Yves Beghein, Rajendra Mitharwal, Kristof Cools, and Francesco P Andriulli. «On a low-frequency and refinement stable PMCHWT integral equation leveraging the quasi-Helmholtz projectors». In: *IEEE Transactions on Antennas and Propagation* 65.10 (2017), pp. 5365–5375 (cit. on p. 44).

[36] Julius Adams Stratton. *Electromagnetic theory*. Vol. 33. John Wiley & Sons, 2007 (cit. on p. 50).

[37] Constantine A Balanis. *Antenna theory: analysis and design*. John wiley & sons, 2015 (cit. on p. 51).

[38] John David Jackson. *Classical electrodynamics*. 1999 (cit. on p. 53).

[39] Yat Hei Lo, Li Jun Jiang, and Weng Cho Chew. «Finite-width feed and load models». In: *IEEE transactions on antennas and propagation* 61.1 (2012), pp. 281–289 (cit. on p. 60).

[40] Rob Maaskant and Michel Arts. «Reconsidering the voltage-gap source model used in moment methods». In: *IEEE Antennas and Propagation Magazine* 52.2 (2010), pp. 120–125 (cit. on p. 61).

[41] KT Shivaram. «Gauss Legendre quadrature over a unit circle». In: *International Journal of Engineering Research & Technology* 2.9 (2013) (cit. on pp. 65, 93).

[42] Clayton R Paul. *Inductance: loop and partial*. John Wiley & Sons, 2011 (cit. on p. 67).

[43] DRSM Wilton, S Rao, AW Glisson, D Schaubert, O Al-Bundak, and C Butler. «Potential integrals for uniform and linear source distributions on polygonal and polyhedral domains». In: *IEEE Transactions on Antennas and Propagation* 32.3 (1984), pp. 276–281 (cit. on p. 81).

[44] Roberto D Graglia. «On the numerical integration of the linear shape functions times the 3-D Green's function or its gradient on a plane triangle». In: *IEEE transactions on antennas and propagation* 41.10 (1993), pp. 1448–1455 (cit. on p. 81).

[45] Michael A Khayat, Donald R Wilton, and Patrick W Fink. «An improved transformation and optimized sampling scheme for the numerical evaluation of singular and near-singular potentials». In: *IEEE Antennas and Wireless Propagation Letters* 7 (2008), pp. 377–380 (cit. on p. 82).

[46] Michael A Khayat and Donald R Wilton. «Numerical evaluation of singular and near-singular potential integrals». In: *IEEE transactions on antennas and propagation* 53.10 (2005), pp. 3180–3190 (cit. on p. 82).

[47] Michael G Duffy. «Quadrature over a pyramid or cube of integrands with a singularity at a vertex». In: *SIAM journal on Numerical Analysis* 19.6 (1982), pp. 1260–1262 (cit. on p. 82).

[48] Luca Rossi and Peter J Cullen. «On the fully numerical evaluation of the linear-shape function times the 3D Green's function on a plane triangle». In: *IEEE Transactions on Microwave Theory and Techniques* 47.4 (1999), pp. 398–402 (cit. on p. 82).

[49] Zhi Guo Qian, Weng Cho Chew, and Roberto Suaya. «Generalized impedance boundary condition for conductor modeling in surface integral equation». In: *IEEE Transactions on Microwave Theory and Techniques* 55.11 (2007), pp. 2354–2364 (cit. on pp. 82, 83, 85).

[50] Swagato Chakraborty and Vikram Jandhyala. «Evaluation of Green's function integrals in conducting media». In: *IEEE transactions on antennas and propagation* 52.12 (2004), pp. 3357–3363 (cit. on pp. 82, 84, 85, 88).

[51] Gouri Dhatt, Emmanuel Lefrançois, and Gilbert Touzot. *Finite element method*. John Wiley & Sons, 2012 (cit. on p. 94).

[52] Vladimir Ivanovich Krylov and Arthur H Stroud. *Approximate calculation of integrals*. Courier Corporation, 2006 (cit. on p. 94).